

Review

Recent Advances in Hole-Transporting Layers for Organic Solar Cells

Cintha Anrango-Camacho ¹, Karla Pavón-Ipiales ¹, Bernardo A. Frontana-Urbe ^{2,3}
and Alex Palma-Cando ^{1,*}

¹ Grupo de Investigación Aplicada en Materiales y Procesos (GIAMP), School of Chemical Sciences and Engineering, Yachay Tech University, Hda. San José s/n y Proyecto Yachay, Urcuqui 100119, Ecuador; cinthya.anrango@yachaytech.edu.ec (C.A.-C.); karla.pavon@yachaytech.edu.ec (K.P.-I.)

² Centro Conjunto de Investigación en Química Sustentable UAEMex-UNAM, Carretera Toluca Atlacomulco, Km 14.5, Toluca 50200, Mexico; bafrontu@unam.mx

³ Instituto de Química, Universidad Nacional Autónoma de México, Circuito Exterior, Ciudad Universitaria, Ciudad de México 04510, Mexico

* Correspondence: apalma@yachaytech.edu.ec

Abstract: Global energy demand is increasing; thus, emerging renewable energy sources, such as organic solar cells (OSCs), are fundamental to mitigate the negative effects of fuel consumption. Within OSC's advancements, the development of efficient and stable interface materials is essential to achieve high performance, long-term stability, low costs, and broader applicability. Inorganic and nanocarbon-based materials show a suitable work function, tunable optical/electronic properties, stability to the presence of moisture, and facile solution processing, while organic conducting polymers and small molecules have some advantages such as fast and low-cost production, solution process, low energy payback time, light weight, and less adverse environmental impact, making them attractive as hole transporting layers (HTLs) for OSCs. This review looked at the recent progress in metal oxides, metal sulfides, nanocarbon materials, conducting polymers, and small organic molecules as HTLs in OSCs over the past five years. The endeavors in research and technology have optimized the preparation and deposition methods of HTLs. Strategies of doping, composite/hybrid formation, and modifications have also tuned the optical/electrical properties of these materials as HTLs to obtain efficient and stable OSCs. We highlighted the impact of structure, composition, and processing conditions of inorganic and organic materials as HTLs in conventional and inverted OSCs.

Keywords: hole transporting layer; organic solar cells; photoconversion efficiency; stability; metal oxides; metal sulfides; nanocarbon materials; conducting polymers; conjugated polyelectrolyte; small organic molecules



Citation: Anrango-Camacho, C.; Pavón-Ipiales, K.; Frontana-Urbe, B.A.; Palma-Cando, A. Recent Advances in Hole-Transporting Layers for Organic Solar Cells. *Nanomaterials* **2022**, *12*, 443. <https://doi.org/10.3390/nano12030443>

Academic Editor: Vlad Andrei Antohe

Received: 13 December 2021

Accepted: 24 January 2022

Published: 28 January 2022

Publisher's Note: MDPI stays neutral with regard to jurisdictional claims in published maps and institutional affiliations.



Copyright: © 2022 by the authors. Licensee MDPI, Basel, Switzerland. This article is an open access article distributed under the terms and conditions of the Creative Commons Attribution (CC BY) license (<https://creativecommons.org/licenses/by/4.0/>).

1. Introduction

Solar energy has enough power capacity to satisfy the whole world's demand [1,2]. According to Luqman et al. [3], the amount of solar energy irradiated at the Earth's atmosphere ranges from 200 to 250 Wm⁻² per day, of which ca. 70% is available for conversion into power generation [4,5]. Research on solar energy technology, which aims to convert sunlight directly into electrical energy, is vital to switch into low-carbon energy systems [6,7]. The intense developments concerning solar energy have boosted the investigations to optimize the efficiency and stability of emerging photovoltaic technology, such as dye-sensitized solar cells, organic solar cells (OSCs), perovskite solar cells, quantum dot solar cells, and so on, of which OSCs are one of the most promising technologies [8–14]. Since Kearns and Calvin's pioneering work on OSCs in 1958, one significant breakthrough in solar energy technology has been the efficient electron transfer between a conjugated polymer and fullerene derivative [15,16]. It encouraged the interest in the light-harvesting of OSCs from the structure device into the materials used for their construction [16–19]. OSCs are based

on organic semiconductors as active layers with unique advantages to achieve low-cost renewable energy harvesting, owing to their material and manufacturing advances [20,21]. OSCs have some advantages: low-cost fabrication, solution processes, light weight, flexibility, a great opportunity for large-scale roll-to-roll production, and a low environmental disposable impact. Furthermore, OSCs showed shortened energy payback time, that is, the time needed to recover the device fabrication energy [22]. OSCs' record efficiency is over 18.2% in single cells [23,24] and over 18.6% in tandem cells [25]. In the last ten years, extensive research and development have been conducted in OSCs to improve lifetimes (7–10 years) and the power conversion efficiency (PCE) over 10% in roll-to-roll industrial manufacturing [23,26–28]. Some companies have developed OSCs commercially, such as Heliatek, infinityPV, and OPVIUS GmbH, which manufacture flexible OSC modules [29] representing 5% of the market [30]. OSCs have been used in small-scale applications as building integrated photovoltaics, e.g., incorporated on roofs and walls of storage buildings and solar parks [31].

The core of the OSCs is a blend of electron-donor materials (e.g., conjugated polymers) and fullerene-based or non-fullerene-based electron-acceptor materials [32]. This central layer is called the photoactive layer and absorbs solar radiation. A typical OSC has a bulk heterojunction (BHJ) structure that is a mixed-blend of donor and acceptor materials, which constitute the photoactive layer [33]. When the solar cell is irradiated, the photoactive layer absorbs photons to generate excitons (bound electron-hole pairs), which dissociate into free charge carriers in the donor-acceptor interface, producing separated holes and electrons. These free charges are then extracted and transported to the corresponding electrodes [34,35]. Interfacial layers are generally utilized to tailor the work function (WF) of electrodes for the maximization of charge carrier (e.g., electrons and holes) collection. They modify the interface to alter the photoactive layer morphology and minimize charge carrier recombination (improving the charge selectivity) at the interface between the active layer and transport layer [36]. Moreover, the interfacial layers help to form an ohmic contact between electrodes and active layers as well as tune the energy level alignment to facilitate the charge extraction [37,38]. Hole-transporting layers (HTLs), also called anode interfacial layers (AILs), facilitate hole extraction and transportation while blocking electron flux. Hole-transport materials are deposited between the photoactive layer and the anode, improving the device performance. HTLs, used in conventional polymer solar cells (PSCs), were first reported in the late 1990s after a similarly reported experimentation in organic light-emitting diodes (OLEDs) [39,40]. Some important characteristics are required for hole-transport materials such as a high conductivity, high transparency (since the sunlight is absorbed by the photoactive layer through the HTL on anode), solution processability and favorable stability, high WF (since the energy level of materials should be appropriate for charge collection), and predominantly good hole mobility [39].

Over the past five years, the research community has been working on achieving high efficiency and stability and low cost of production on emerging clean energy sources, such as OSCs, with a priority on interfacial layer engineering. Tian et al. analyzed the diverse molecular structures employed as HTL and electron transporting layers (ETLs) to minimize energy losses in non-fullerene OSCs [41]. Palilis et al. discussed the relationship between the optoelectronic and physical properties of inorganic materials and their functionality at the interface [42]. Gusain et al. showed the physical mechanisms involved with the interfacial issues and the routes adopted to address them [43]. Amollo et al. explored the physical and optical properties of polymers and metal oxides together with their hybrids and graphene to guide the choice of suitable interfacial materials [44]. Wu et al. showed the impact of nanotechnology and nanomaterials in manufacturing multifunctional interfacial layers to enhance OSCs' performance [45]. Huang et al. reviewed the feasibility of tuning the optical and electrical properties of solution-processed ternary oxides, as potential carrier transports layers, from the large range of crystal structures and adjustable atomic ratio [46]. Herein, we presented an extensive state-of-the-art review about the advances in HTLs that show great potential for enhancing the efficiency (e.g., PCE) and stability of OSCs.

The progress made on improving HTL properties of inorganic (metal oxides and sulfides), nanocarbon materials, conjugated polymers, and small organic molecules as HTLs in OSCs was discussed, focusing on solution-processing conditions, deposition methods, doping, composite/hybrid formation, and chemical modifications. Considering the numerous and highly dispersed literature, we tried to include relevant information reported in scientific journals. This review included a short section on the structure and characterization of OSCs and some remarks on HTLs followed by reports of the last five years in the use of hole-transporting materials as HTLs in OSCs. Summary tables of the photovoltaic device architecture and their performance are presented at the end of Sections 4.3 and 4.5.

2. Structure and Characterization of Organic Solar Cells

A conventional OSC consists of an active layer sandwiched between two electrodes with their respective extracting layers to ensure mobility, collection, and transport of the charge carriers [47]. At the bottom, the anode electrode is a transparent conductive oxide, such as indium tin oxide (ITO), and at the top, the cathode is a low WF metal, such as Ca and Al (see Figure 1) [48]. The OSCs based on two organic semiconductors in the active layer can have two architectures: the bilayer and the BHJ devices. Tang et al. presented the sequential stacking of donor and acceptor semiconductors to form the bilayer planar heterojunction in 1986 [17]. However, it has limitations, such as the small surface area between the donor/acceptor interface and the poor excitons' dissociation. Then, the introduction of BHJ devices in 1990 solved bilayer devices' issues [19]. They involve mixing donor and acceptor materials in the bulk body of an OSC to reduce phase separation. Donor and acceptor domains are twice the size of the exciton diffusion length (~10 nm). To expand the active layer's absorption range, tandem OSCs have been proposed to stack two single-junctions with different absorption ranges [49,50]. According to the charge flow direction, OSCs can be divided into conventional and inverted devices (see Figure 1) [51]. Under light irradiation, photons are absorbed by the donor material in the active layer to form excited states, called excitons, which are bound electron-hole pairs. Excitons diffuse towards the donor/acceptor material interface and separate into free charge carriers. Holes and electrons move apart in the highest occupied molecular orbital (HOMO) and the lowest unoccupied molecular orbital (LUMO) levels, respectively (see Figure 1). Then, the separated charge carriers are transported and collected at the electrodes supplying a photocurrent [52].

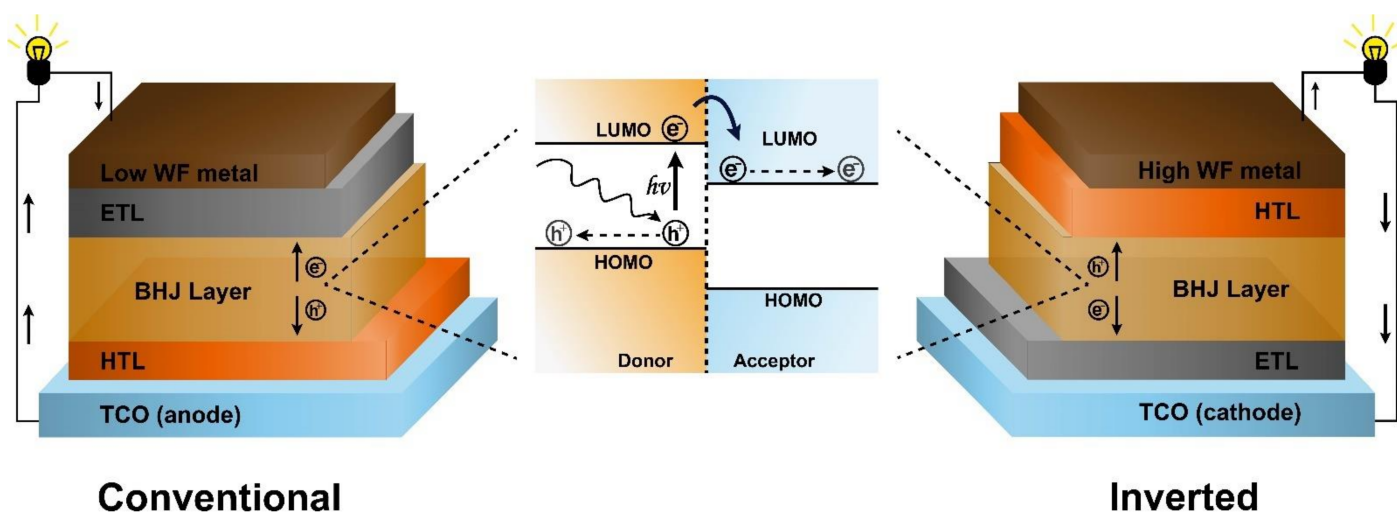


Figure 1. Schematic structure of conventional and inverted OSCs, and a simplified view of the operating principle in the active layer.

The current-voltage (J-V) curve of an OSC is characterized under 1000 W/m^2 light of AM 1.5 solar spectrum [53]. Figure 2a shows a J-V curve of an OSC under darkness

(dashed line) and illumination (solid line) conditions. Photocurrent is not flowing through the electrodes under dark conditions, just the current by the forward bias of contacts as a diode. Under irradiation, photocurrent is generated. PCE is determined by the product of three parameters: short-circuit current density (J_{sc}), open-circuit voltage (V_{oc}), and fill factor (FF) over the incident light power density (P_{in}) as follows [54]:

$$PCE = \frac{V_{oc} \times J_{sc} \times FF}{P_{in}} \quad (1)$$

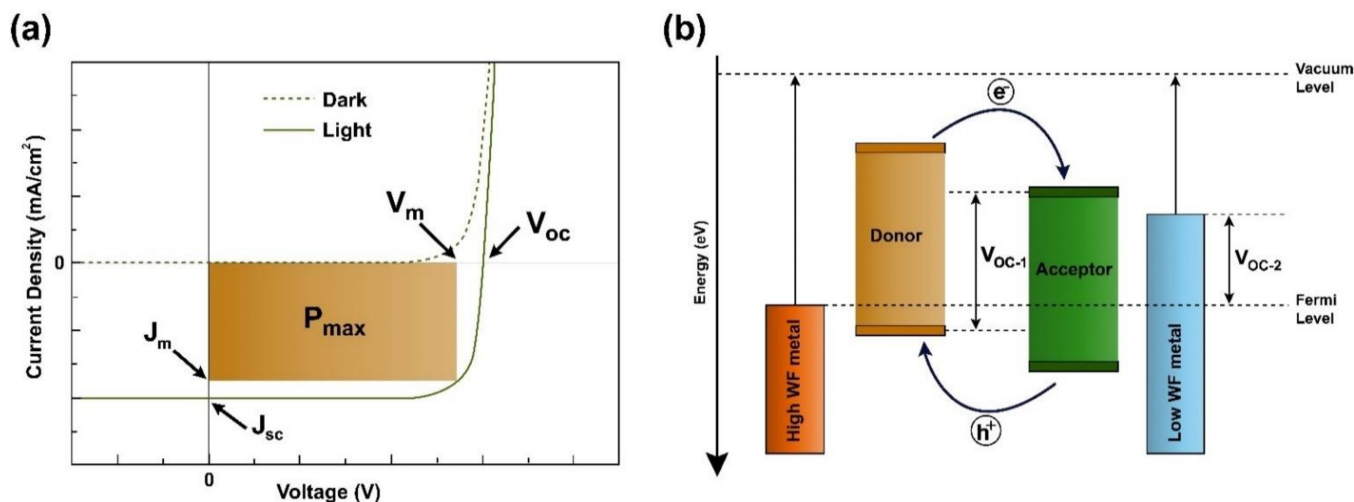


Figure 2. (a) Typical J-V curve and (b) schematic representation of the V_{oc} in a conventional OSC.

The ratio of collected photogenerated charges and the number of incident photons is related to the external quantum efficiency (EQE) of the OSC. V_{oc} is the main driving force for charge separation once the exciton reaches the donor/acceptor interface [55,56]. V_{oc} is the difference of WFs between the quasi-Fermi levels of holes ($E_{F,h}$) in the HOMO level of the donor and the quasi-Fermi levels of electrons ($E_{F,e}$) in the LUMO level of the acceptor in a BHJ under the formation of ohmic contacts with the cathode and anode (depicted as V_{oc-1} in Figure 2b). If a Schottky contact appears in both BHJ/electrode interfaces, the V_{oc} would decrease and would depend on the difference between the WFs of the two metal contacts (depicted as V_{oc-2} in Figure 2b) [57,58]. FF is the ratio between the maximum power output (P_{max}) and the maximum attainable power output ($J_{sc} V_{oc}$). P_{max} describes the maximum power drawn from the device and is the product of the maximum current (J_m) and voltage (V_m) (see Figure 2a) [59], as follows:

$$FF = \frac{P_{max}}{J_{sc} V_{oc}} = \frac{J_m V_m}{J_{sc} V_{oc}} \quad (2)$$

The main factors that influence the FF are the series resistance (R_s) and the shunt resistance (R_{sh}). Their interaction determines the current flow. R_s is attributed to the conductivity of electrodes, BHJ and extracting interface layers, as well as the contact resistance between them [60]. A small R_s increases the mobility of the charge carriers and the performance of OSCs. R_{sh} reflects the current losses from the pinholes and traps in the film. Established relationships describing J-V behavior in OSCs and directly accounting for resistance effects on cell performance are the following [61–64]:

$$J = J_d + J_{sh} - J_{ph} = J_0 \left\{ \exp \left[\frac{e(V - JR_s)}{nk_B T} - 1 \right] \right\} + \frac{V - JR_s}{R_{sh}} - J_{ph} \quad (3)$$

where, J_d is the diode current density, J_{sh} is the leakage current density, J_{ph} is the photogenerated current density, J_0 is the reverse saturation current, e is the elementary charge, n is the

diode ideality factor, k_B is Boltzmann's constant, and T is temperature. J_{sh} is an undesirable current injected from the electrodes in the opposite direction to J_{sc} . A suitable interface morphology decreases J_{sh} and increases R_{sh} independently of the light intensities [65]. Thus, the contact quality at the active layer/electrode interface is critical to optimize FF, V_{oc} , and J_{sc} . Interface transporting layers enhance all these parameters because they tune the energy level alignment at the active layer and electrodes, the surface morphology, and the contact to boost the efficiency and stability of the OSCs [66].

3. Hole-Transporting Layers

Interfacial layers are critical components of OSCs to enhance the collection efficiency of holes and electrons toward the anode and cathode electrodes. In photovoltaic devices, including OSCs, there are barriers to charge extraction by the non-ideal contact between the active layer and the electrodes [39]. This limited interfacial energy alignment inhibits the spontaneous charge transport, resulting in charge accumulation at the interface, thus decreasing V_{oc} , FF, and PCE [67]. Interfacial layers with suitable WFs contribute to match the energy levels of donor and acceptor materials with the electrodes, favoring the charge transport and stability [38]. The interfacial layers must be charged selectively to avoid charge recombination at the electrodes in addition to the tuning of the energy levels. HTLs and ETLs increase the hole and electron mobility in the opposite direction to collect only one type of charge on each electrode [68]. In the 1990s, HTLs were introduced to the organic electronics field by Tokito et al., who showed that hole-injection increased from inserting vanadium, molybdenum, and ruthenium oxides layers into OLEDs [69]. HTL's central role is the efficient hole extraction and transport from the HTL/active interface to the anode/HTL interface, increasing power generation [70]. To achieve high-performance OSCs, the materials used for HTLs need to show (i) high WF that matches with the HOMO energy level of the donor material and the anode energy level, (ii) transparency to increase the light absorption by the active layer, (iii) high hole mobility to lower the charge accumulation and recombination, (iv) a large band gap to block electron carriers, and (v) chemical resistance to external factors [38,71,72]. The first materials used as HTLs in OSCs were inorganic p-type transition metal oxides (MoO_3 , WO_3 , NiO , Fe_3O_4) or metal sulfides (MoS_2), which showed high stability and performance [73–77]. Most of them required high vacuum for deposition, which, compared with organic materials, might be costly for industrial and large-scale processing [78]. Poly(3,4-ethylenedioxythiophene)-poly(styrene sulfonate) (PEDOT:PSS) is still the standard conducting polymer used as HTL in OSCs because of the low costs, minimal toxicity, facile solution processing, and high WF. However, it is not stable at standard conditions owing to its hygroscopic and acidic nature [79]. Currently, there is an excellent development of cost-effective low-temperature deposition strategies for industrial scaling to avoid the traditional vacuum method used in the manufacture of HTLs. Casting process deposits the material dissolved in liquid form in a solvent on the underlying substrate, followed by drying. Spray casting solves the lack of control in film morphology and uniformity [80]. Spin coating is the most common deposition method of PEDOT:PSS due to its high reproducibility in film thickness and morphology. It applies the spinning at a certain rotation speed of the substrate to dry the deposited liquid material. However, neither large area applicability nor film patterning are achievable by this technique [81]. Electrochemical deposition or electrodeposition allows depositing polymers and inorganic materials through an electric field [82]. The control on deposition has broader applicability for the formation of composites [83]. The roll-to-roll technique is usually utilized in flexible OSCs because the flexible substrate is unwound to pass through printing or coating machines, followed by being rewound on a roll. It opens the applicability for large-area production because substrates are not handled individually but instead in rolls [84,85]. Compared with the vacuum method, these deposition techniques offer the advantage of a continuous and large-area process at mild conditions, avoiding wasting raw materials.

4. Hole-Transporting Materials as HTLs in OSCs

4.1. Metal Oxides

4.1.1. Molybdenum Oxide

MoO_x is an *n*-type material with a valence band edge around 2.5–3 eV below the Fermi level and a conduction band closer to the Fermi level [70]. MoO₃ has a high WF (6.9 eV) and conductivity of $1.2 \times 10^{-7} \text{ Sm}^{-1}$ due to the different states of O and the multivalence of Mo in its three crystal phases (α -MoO₃, β -MoO₃, h-MoO₃) [86–88]. MoO₃ is a promising HTL due to its electronic structure, transparency, conductivity, and stability, enhancing the hole extraction and thus the efficiency of OSCs, compared with PEDOT:PSS [89]. Lee et al. reported that MoO_x HTL-based OSCs are more stable at a high operating temperature near 300–420 K than PEDOT:PSS [90]. Therefore, there is much research in strategies to optimize the solution-processing methods and the film properties of MoO₃ [91–93]. Bortoti et al. obtained the orthorhombic phase of MoO₃ (α -MoO₃) by refluxing MoS₂ in HNO₃ and H₂SO₄ as the oxidant media, followed by heating at 120 °C for 10 min to evaporate the solvent [94]. The energy level of α -MoO₃ well-matched with that of the P3HT. A PCE of 1.55% was obtained in a FTO/ZnO/P3HT:PC₆₀BM/MoO₃/Ag cell structure. Ji et al. used ammonium heptamolybdate (AHM) as the precursor solution to prepare a solution-processed MoO₃ array on P3HT:PC₆₁BM by the ultrasonic spray-coating method at 80 °C [95]. The solution-processed MoO₃ micro arrays improved the charge transport between the active layer and the anode. Thus, the V_{oc} and FF increased to 0.59 V and 59.2%, and a higher PCE of 3.40% was achieved. MoO₃ is adequate to attain a high built-in potential and V_{oc} because it can suppress interfacial reactions at the HTL/BHJ interface. MoO₃ nanoparticles (NPs) can be added at the interface between the active layer and the PEDOT:PSS to take advantage of the localized surface-resonance plasmon (LSRP) effect of NPs and the electronic structure of MoO₃ [96]. MoO₃ NPs increased the path length of the absorbed light and blocked the electrons flow to the anode, resulting in a higher J_{sc} and FF, and thus a PCE of 4.11% was reached over a long period of 30 days [97]. The high transparency of MoO_x allows an enhanced back-reflected light into the active layer to enhance the photocurrent, as shown in the EQE curves (see Figure 3a) [98]. At low temperatures of 80–200 °C, Jagadamma et al. prepared an alcohol-based MoO_x nanocrystalline suspension processed directly over temperature-sensitive active layers (see Figure 3b) [99]. The water-free solvent and the fine MoO_x nanocrystal diameter (<5 nm) resulted in a compact and smooth film with a thickness around ~5–10 nm. All inverted OSCs reached a PCE above 9%, retaining 90% of their efficiency after five months of aging. MoO₃ nanocrystals (NCs) with a size greater than 5 nm can form a composite of MoO_x with Ag nanowires (NWs) to lower the nanowire junction resistance by close packing Ag NWs. The Ag NWs/MoO_x composite also served as a barrier for Ag diffusion into the active layer's bulk. Wang et al. added AgAl NPs into MoO_x HTL to prevent the Ag diffusion by forming AlO_x [100]. The PTB7-Th:PC₇₁BM cell retained 60% of the initial PCE (9.28%) over 120 days. Cong et al. used ammonium molybdate and citric acid in 2-methoxyethanol as the precursor to prepare MoO_x, followed by 10 vol.% of H₂O₂ to form a stable conductive film [101]. The presence of H₂O₂ induced oxygen vacancies to help in the polyvalence and conductivity of the MoO_x film. Jung et al. prepared a solution-processed MoO_x from the dissolution of MoO_x powder in ammonium hydroxide (NH₄OH) and isopropanol solvent [102]. The Mo⁵⁺-OH bonds induced by hydroxyl radicals facilitated the charge transport with higher hole mobilities, of $2.3 \times 10^{-6} \text{ cm}^2\text{V}^{-1}\text{s}^{-1}$, than PEDOT:PSS, of $2.1 \times 10^{-6} \text{ cm}^2\text{V}^{-1}\text{s}^{-1}$. The gap states induced in the bandgap by the oxygen defects tuned the Fermi level of MoO_x with the HOMO of PBDB-T as the donor material, showing overall improvement in FF and J_{sc} with a PCE of 10.86%. The excess of oxygen vacancies during the film formation results in recombination sites which compromise the performance and stability of the OSC [37]. Kobori et al. improved the J_{sc} and FF when the as-deposited solution-processed MoO_x film was annealed at 160 °C for 2 min [103]. The enhancement in the efficiency from 1.40% to 6.57% is because of surface passivation of MoO_x HTL by annealing treatment, resulting in a reduction of oxygen vacancies in the MoO_x film (see Figure 3c). It helps the fabrication

of OSCs with temperature-sensitive low-bandgap polymers, such as PTB7-Th:PC₇₁BM and PCPDTBT:PC₇₁BM. Li et al. reported that low-temperature annealing treatment could also enhance the preparation of solution-processed MoO_x films from peroxomolybdic acid organosol precursor solution at 150 °C, while also achieving passivation of the surface [104].

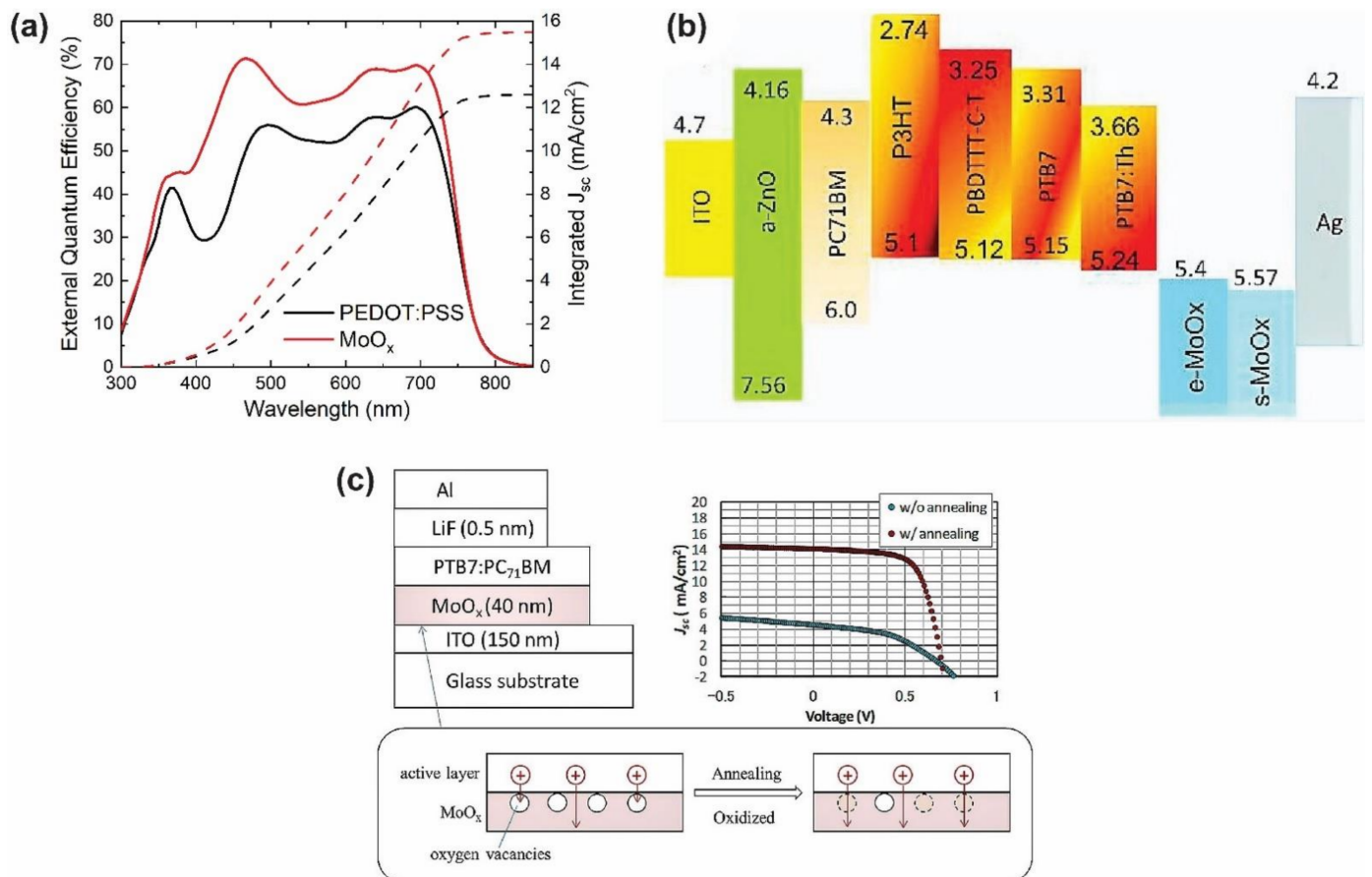


Figure 3. (a) External quantum efficiency of inverted OSCs with MoO₃ and PEDOT:PSS HTLs. Adapted with permission from [98]. (b) Energy level diagram of inverted OSCs with different donor polymers. Adapted with permission from [99]. Copyright 2016, Elsevier. (c) Reduction of oxygen vacancies by annealing treatment. Adapted with permission from [103]. Copyright 2016, Elsevier.

Ultraviolet (UV) annealing can retain a higher PCE over a longer period if compared with OSCs' efficiency under no annealing or under thermal annealing (100 °C) [105]. UV annealing removed the adhered organic contaminants on the MoO₃ film surface by two short wave UV lights at 185 nm and 285 nm. This radiation decomposed O₃ into O₂ and active O, which oxidized and removed any organic contaminant by transformation into volatile gases. Cai et al. achieved a PCE of 9.27% in the PBDB-T:ITIC BHJ cell using an ultraviolet-deposited MoO₃ film [106]. Tan et al. developed a solution-processed, annealing-free aqueous MoO_x for non-fullerene OSCs [107]. By adding a small amount of water to MoO₂(acac)₂, the ligand of MoO₂(acac)₂ was removed from the MoO_x film, avoiding thermal treatments, and enhancing the PCE of PBDB-T-2F:Y6 cell up to 17.0%. In addition to the impurities in the precursor solution, external factors, such as air, create oxygen defects in the MoO_x film lattice, which change the electric properties (e.g., WF, energy levels) and the performance of the OSC [108,109]. Soultati et al. reported the microwave (MW) air annealing approach for recovering the WF in stoichiometric MoO_x and the efficiency of the FTO/MW-MoO_x/P3HT:PC₇₁BM/Al cell up to 5.0% [110]. The WF recovery resulted in the formation of a large interfacial dipole at the FTO/MW-MoO_x/P3HT:PC₇₁BM interfaces, favoring hole extraction via gap states.

In addition to post-treatments, the film properties of the MoO₃ HTL in OSCs also improve through strategies involving doping, composite/hybrid formation, multilayers, and deposition techniques. Chang et al. reported vanadium-doped MoO_x films at different ammonium metavanadate concentrations. The smallest band offset (1.13 eV) between the valence band edge of V_{0.05}MoO_x and P3HT HOMO level favored the hole transport due to having the lowest resistance among all V-MoO_x films [111]. Marchal et al. reported a decrease of 3 nm in the surface roughness of MoO_x HTL by adding 0.5 mol% of Zr and Sn via a combustion chemical deposition method at low temperatures [112]. The Zr and Sn atoms also covered the surface defects of MoO_x, forming a uniform and well-covered HTL film on the ITO electrode (see Figure 4a). Bai et al. employed a small amount of *p*-type NiO_x into *n*-type MoO₃ in one step [113]. Since MoO₃:NiO_x was highly transparent and had a conduction band of 3.25 eV and a WF of 5.10 eV (see Figure 4b), the MoO₃:NiO_x film was able to block electrons while enhancing the contact to charge transport toward the anode, achieving a PCE of 10.81% in PBDB-T:IT-M BHJ OSCs. Li et al. showed the feasibility of the work function tuning of MoO_x to use as both HTL and ETL through the Cs intercalation approach [114]. MoO_x and the intercalated mole ratio MoO_x:Cs (1:0.5) tested in P3HT-based conventional and inverted OSCs as HTL and ETL achieved PCEs of 3.50% and 3.20%. Besides, high PCEs of 7.35% and 6% were obtained in the PBDDTTT-S-T-based conventional and inverted OSCs. The Cs-intercalation within the MoO_x acts as an *n*-type semiconductor [115] to tune the work function from 5.30 to 4.16, which favors the energy alignment at the interface and the reduction in the charge carrier losses. Yoon et al. synthesized a dual-HTL by mixing solution-processed copper iodide (CuI) and thermally evaporated MoO₃ [116]. The interaction between MoO₃ and the CuI increased the forbidden gap states in the MoO₃ layer for the hole transport by forming small oxygen vacancies and Mo⁵⁺ defect states. Zhiqui et al. reported a composite of copper bromide (CuBr₂) and molybdenum trioxide (MoO₃) as the HTL for OSCs [117]. CuBr optimized interfacial contact to increase charge carriers, and MoO₃ blocked electron transport, resulting in improved FF (65.20%), J_{sc} (19.65 mAcm⁻²), and an increase in the PCE from 7.30 to 9.56%. Li et al. prepared CTAB-modified MoO₃ nanocomposites by adding a small amount of cetyltrimethylammonium bromide (CTAB) solution into ammonium molybdate and annealing it at 200 °C in a glovebox [118]. CTAB passivated the surface traps of MoO₃ films to avoid the recombination sites, resulting in a film with PCEs of 5.80 ± 0.13% in P3HT:ICBA and 8.34 ± 0.13% in PTB7:PC₇₁BM OSCs. The formation of polynuclear metal-oxo clusters (PMC) of tungsten/molybdenum as HTLs showed PCEs of 14.3% and higher stability than PEDOT:PSS [119]. The variation in the W/Mo ratio allowed the increase of the hole transport from the polymer donor (PBDBT-2F) toward the anode due to the formation of an inorganic-organic charge transfer complex with a barrier-free interface. This unique characteristic of PCM clusters in OSCs might promote new insights for its utility in high-performance optoelectronic devices. Kwon et al. also boosted the efficiency by developing an alloy of molybdenum-tungsten disulfides films as HTL to replace PEDOT:PSS efficiently [120]. As was mentioned before, Ag NPs can be incorporated into MoO₃ to enhance the electrical and optical properties of the HTL. Indeed, it can form a MoO₃/AgNPs/MoO₃ structure as HTL to improve the J_{sc} and reduce the recombination by the backscattering and surface plasmon effects of AgNPs [121]. Zhang et al. prepared a solution-processed MoO₃/AgNPs/MoO₃ (MAM) HTL in PTB7:PC70BM cells [122]. The MAM multilayer enabled an enhanced charge collection by suppressing charge recombination. The efficiency of the OSC was superior (7.68%) to that of the s-MoO₃ (6.72%). The manufacture of OSCs has also been limited by the material's finite availability, such as the transparent anode electrode, ITO [123,124]. An ITO-free flexible OSC obtained by Chen et al. used multiple layers of molybdenum oxide MoO₃/LiF/MoO₃/Ag/MoO₃ as transparent electrodes, facilitating the transmittance and charge transport [125]. Lee et al. reported a reduced atomic percentage of In and Sn at the surface of ITO electrodes by graded sputtering of MoO₃ HTLs (see Figure 4c) [126]. The MoO₃-graded ITO (MGI) electrode formed three regions: (i) the bottom ITO region, providing high transparency

(83.8%), (ii) the Mo-In-Sn-O graded interlayer, and (iii) the MoO₃ region, which served as the HTL. For thin HTLs, the deposition method might cause defects or form compacted layers depending on the working conditions. Uniform s-MoO_x HTLs prepared by direct current (DC) magnetron sputtering showed enhanced charge transport with a FF of 50%, as the s-MoO_x film's surface was smoother and controlled by DC in comparison with the conventional evaporated approach [127]. Chaturvedi et al. applied a DC voltage of 1 kV during the spray deposition of MoO₃ HTL, obtaining a PCE of 2.71% [128]. The applied electric field controlled both the optical and electrical properties of the thin MoO₃ film. Dong et al. used a laser-assisted method to obtain a hydrogenated molybdenum oxide H_yMoO_{3-x} film for flexible OSCs (see Figure 4d) [129]. By controlling the energy of the KrF laser (λ = 248 nm) during the irradiation of photons on the AHM precursor solution, the WF (5.6 eV) and the hole transport of H_yMoO_{3-x} film increased, allowing higher PTB7:PC₇₀BM cell performance. The laser processing time lasts only 30 ns, so it is suitable in time and economically compared with the thermal evaporation method.

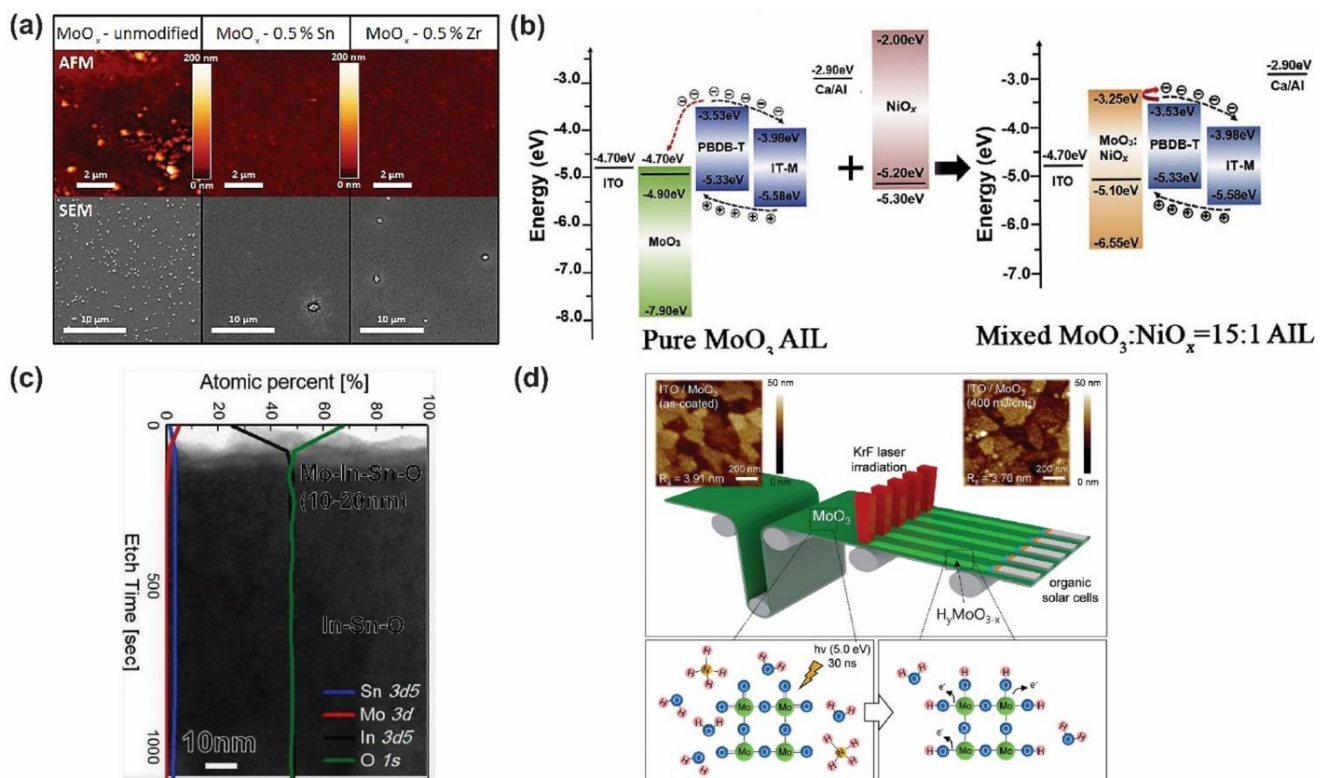


Figure 4. (a) AFM and SEM images of unmodified and modified MoO_x HTL. Adapted with permission from [112]. (b) Energy levels of pristine and doped MoO₃ with a NiO_x layer. Adapted with permission from [113]. Copyright 2019, Elsevier. (c) XPS depth profile of MGI electrode. Adapted with permission from [126]. Copyright 2016, Elsevier. (d) Scheme of laser-assisted synthesis of H_yMoO_{3-x}. Adapted with permission from [129]. Copyright 2016, Royal Society of Chemistry.

4.1.2. Tungsten Oxide

Tungsten oxide is an *n*-type material with a WF ranging from 4.7 to 6.4 eV depending on the film preparation [130–133]. Tungsten oxide is a hole extracting layer that can work efficiently in conventional and inverted OSCs using vacuum and solution-processing methods [74,134]. WO_x is an amorphous structure that (i) forms smooth surface morphologies, (ii) increases the charge mobility in the active layer, and (iii) enhances the charge collection because V_{oc} depends linearly on the anodic WF when there is not ohmic contact at the anode/donor interface [135]. Thus, the enhancement in solution-processing WO_x-based OSCs is particularly focused on increased light absorption. Lee et al. designed an Au@SiO₂-WO₃ nanocomposite (NC) which works as a photon antenna for high

light absorption [136]. The localized surface-plasmon resonance (LSPR) effect of AgNPs enhances the intensity of photon absorption in the P3HT:PC₆₁BM BHJ cell, resulting in increased J_{sc} . The favorable plasmonic effect is comparable to some reported literature for plasmonic nanomaterials-based optoelectronic devices [137–139]. Moreover, high hole mobility of WO_x NPs boosted the device PCE by up to 1.6%. The surface morphology of the Au@SiO₂-WO₃ NC film was kept uniform due to the SiO₂ shell avoiding the aggregation effect of the Au NPs. Instead of SiO₂, the aggregation effect can be avoided by controlling the concentration of Au NPs. Using 10 wt% of Au NPs, the Au-WO₃ NC HTL decreased the surface morphology's roughness, achieving a PCE of 60.37% [140]. Shen et al. enhanced the light absorption and the PCE of OSCs based on the LSRP effect of structure-differentiated silver nano-dopants in solution-processed WO_x HTL [141]. Three silver nano-dopants, (i) naked Ag NPs (nAgp), (ii) SiO₂-covered Ag NPs (SiAgp), and (iii) naked Ag nanoplates (nAgPI), were synthesized. The triangular nAgPI reached the highest PCE of 4.6% while spherical nAgp reached the lowest. The spherical nAgp surface decreased the PCE because its surface can directly contact the donor/acceptor material of the active layer, resulting in excitons quenching and thus weakening LSRP effects (see Figure 5). The shape of NPs affects the overall performance of OSCs by tuning plasmon-electrical [142], plasmon-optical [143,144], and charge-storage effects [145]. Ren et al. reported the high efficiency of OSCs by incorporating gold nanostars (Au NSs) between HTL and the active layer [146]. The plasmonic asymmetric modes of Au NSs enhanced the optical absorption of the active layer and the balance of photogenerated charges by shortening transport path length in the HTL. The localized plasmonic effect of NPs manipulates transport paths of photogenerated carriers in bulk heterojunction OSCs and thus reduces the charge recombination sites and the space-charge-limit effect [147,148]. Li et al. reported comparable results by applying Ag nanoprisms to achieve higher PCE through the improvement in the broadband absorption [149]. Remya et al. performed a study between dehydrated and di-hydrated WO₃ films as HTL in the inverted P3HT:PC₆₁BM and PTB7:PC₇₁BM cells [150]. The hydrated phase of WO₃ enabled a suitable energy level alignment with the active layer by tuning the water coordination, resulting in a higher PCE of 5.1% and 7.8%, respectively.

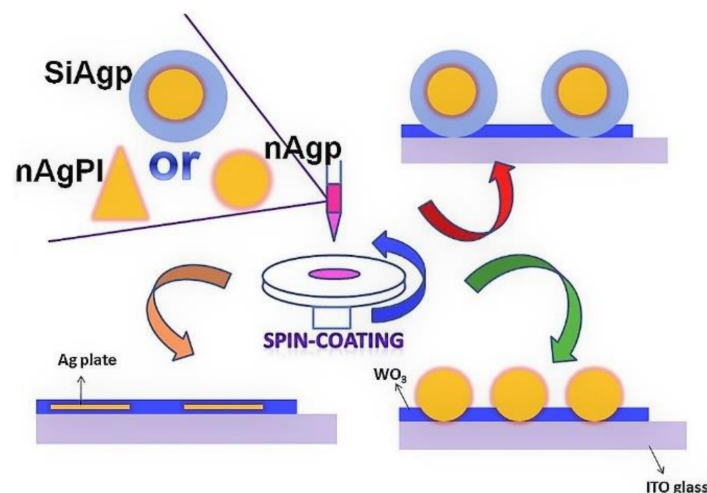


Figure 5. Schematic representation of different silver nanoparticles structures/WO₃ layers by spin coating. Adapted with permission from [141]. Copyright 2016, Elsevier.

4.1.3. Vanadium Oxide

V₂O₅ is a hole-transporting/electron-blocking layer that acts as a protecting layer [151] avoiding surface reactions by the moisture from the working conditions, resulting in improved efficiency and stability [152]. The electronic structure of V₂O₅ corresponds to an *n*-type material with deep electronic states and WF ranging from 4.7 eV to 7.0 eV, depending on the processing method [73,153]. Li et al. reported the Cs-intercalation method to tune the work function of V₂O_x and used Cs-intercalated V₂O_x and V₂O_x as

both ETLs and HTLs in organic optoelectronic devices [114]. The work function tuning and the reduction in the interfacial barrier of Cs-intercalated V_2O_x allowed for obtaining PCEs in P3HT and PBDTDTT-S-T-based conventional and inverted OSCs up to 3.59% and 7.44%. Xu et al. reported a low-temperature solution-processed V_2O_5 by dissolving V_2O_5 powder into water at room temperature [154]. V_2O_5 -based HTLs showed a PCE of 8.05% in ITO/ V_2O_5 /PTB7:PC₇₀BM/LiF/Al OSCs compared with PEDOT:PSS-based HTLs with a PCE of 7.46%. V_2O_5 served as an optical spacer that increased light absorption, leading to a higher photocurrent. V_2O_5 powder can also be treated directly from the melting-quenching sol-gel method to obtain an easy tunable $V_2O_5 \cdot nH_2O$ HTL [155]. The energy positioning of the $V_2O_5 \cdot nH_2O$ HTL (with $n = 1$) was closer to PEDOT:PSS [67], allowing an ohmic contact with the novel conjugated polymer donor (PBDS_e-DT2PyT) and the acceptor of P₇₁CBM; thus, a large V_{oc} and a PCE of 5.87% were obtained. The layered and hydrated phase of V_2O_5 is an affordable and tunable charge transport material. Although $V_2O_5 \cdot H_2O$ -based HTLs exhibit better performance than PEDOT:PSS-based HTLs, the melting-quenching sol-gel method might be an expensive method owing to the high melting temperature of V_2O_5 (~800 °C). Cong et al. applied a green method to prepare vanadium oxide hydrate layers ($VO_x \cdot nH_2O$) to enhance the PCE in organic PTB7-Th:PC₇₁BM- and P3HT:PC₆₁BM-based polymer solar cells up to 8.11% and 3.24% [156]. The combined H_2O_2 and ultraviolet ozone (UVO) in-situ treatments allowed for a smooth surface and improved wettability with the presence of dangling bonds on the HTL surface to enhance interfacial contact. The presence of V^{4+} in the composition analysis of $VO_x \cdot nH_2O$ accounted for a small amount of oxygen vacancies, causing *n*-type doping, which is essential to hole transport by extracting electrons through its conduction band [157]. Vishnumurthy et al. reported that V_2O_5 HTL optimized the efficiency of thienothiophene-diketopyrrolopyrrole-based OSCs by up to 1.02% [158]. Remya et al. prepared an efficient hole-transport/electron-blocking hydrated vanadium oxide (HVO) from V_2O_5 powder with hydrogen peroxide [159]. In the P3HT:PC₆₁BM and PBDTT-FTTE:PC₇₁BM BHJ cells, HVO HTL performance was superior to PEDOT:PSS, obtaining 56% enhancement (7.12–11.14%) in the PCE for the PBDTT-FTTE:PC₇₁BM-based inverted OSC with a lower degradation of 1.4% over 20 weeks. In addition to the V_2O_5 powder, V_2O_5 HTLs can be prepared by other precursors. Xu et al. reported an ammonium metavanadate ammonium water solution for processing VO_x HTLs in PTB7:PC₇₁BM BHJ cells with a PCE of 7.7% [160]. This HTL showed a WF of 5.3 eV and high conductivity by air-annealing treatment at 210 °C for 5 min. The thermal treatment smoothed the surface film to reduce the leakage current, obtaining a higher J_{sc} . Although the stability was better than PEDOT:PSS with a remaining 83% efficiency after four days, it was still low compared with other inorganic HTLs. Shafeeq et al. reported the formation of uniform and crystalline V_2O_5 nanorods by thermal decomposition of ammonium metavanadate NH_4VO_3 to enhance surface morphology and efficiency of OSCs [161]. Alsulami et al. obtained a stable V_2O_x HTL by using vanadium (V) oxytriisopropoxide as the precursor, which converted into V_2O_x by hydrolysis in air [162]. The PCE of the V_2O_x HTL was insensitive to thermal annealing at 100 °C and 200 °C because its optical and electronic properties were comparable to the vacuum-deposited V_2O_5 . Besides, the highly tunable V_2O_5 thin films prepared by the solution-processing method boost inverted OSCs because of their higher stability under air conditions [163]. To optimize the interface properties and OSC performance, VO_x NP can efficiently be mixed with PEDOT:PSS solution, resulting in a stable VO_x :PEDOT:PSS HTL by the uniform molecular distribution of VO_x with PEDOT:PSS as reported by Teng et al. [164]. They achieved a PCE, of 10.2%, compared with PEDOT:PSS, of 5.27%, when VO_x :PEDOT:PSS was used as HTL in the TPD-3F:IT-4F cells. Xia et al. reported a nanoparticulate compact V_2O_5 film as HTL using a facile metal-organic decomposition method to replace the traditional HTLs [165]. By adding polyethylene glycol (PEG) as an additive in the precursor, a uniform and compact film of V_2O_5 served as HTL in the PTB7:PC₇₀BM, improving the interface contact, J_{sc} , and the FF. Compared with the spin coating, the spray coating of V_2O_5 HTL has allowed the large-scale production of flexible OSCs in a roll coater [166]. Using a precursor solution of vanadium

oxytriisopropoxide (VTIP) diluted in ethanol (1:100), V_2O_5 HTLs exhibited improved electrical properties. The mechanical stress on V_2O_5 HTL was mitigated by introducing a PEDOT:PSS binding-interfacial layer between V_2O_5 HTL and the Ag electrode in the inverted P3HT:PC₆₀BM and PBDTTTz-4:PC₆₀BM BHJ cells. Arbab and Mola also explored electrochemical deposition that resulted in 80% enhancement in PCE (2.43%) compared with PEDOT:PSS-based OSCs [167]. Kavuri et al. reported electrospray deposition (ESD) for V_2O_5 HTL in PTB7:PC₇₁BM-based OSCs with a PCE of 7.61% [168]. Compared to the spin-coating, the ESD allowed more control in the deposition conditions and reduced the manufacturing costs of V_2O_5 -based OSCs. Surface morphology, charge mobility, and interfacial contact were adjusted as a function of the solvent evaporation rate. V_2O_5 HTL has also been effective in ITO-free polymer solar cells with an optimized precursor solution (VTIP) of 0.005% [169]. The deposition of V_2O_5 HTL on PEDOT:PSS, as the anode, led to increase R_{sh} and conductivity with the active layer of P3HT:PC₆₁BM by the hydrophobic surface of V_2O_5 , resulting in an uniform and compact HTL with a PCE of 3.33%. V_2O_5 is also a potential material that increases the anode's WF of indium zinc oxide (IZO), exhibiting a higher PCE of 2.8% than that flexible OSCs with only IZO [170].

4.1.4. Nickel Oxide

Non-stoichiometric NiO_x is a wide bandgap *p*-type semiconductor [171]. NiO_x is an efficient electron-blocking layer to the anode due to its conduction band minimum, 1.8 eV, which is above the LUMO of the organic donor P3HT (3.0 eV) [75]. Due to the conduction band of NiO_x being closer to the vacuum level, it is able to suppress electron recombination at the anode [172]. The ohmic contact between NiO and P3HT allows holes to freely transport from the active layer to the anode through the Ni^{2+} vacancy-based hole-conducting anode band [173]. Parthiban et al. demonstrated an enhancement in OSC performance with a NiO HTL deposited via spin coating [174]. Using the precursor solution of nickel acetate and a simple post-annealing process (>300 °C) to reduce roughness, NiO HTL achieved a FF of 63.0% and a corresponding PCE of 4.45% in RP(BDT-PDBT):PC₇₀BM solar cells. Although NiO-based HTLs exhibit better performance and stability than PEDOT:PSS, the high annealing temperature required to convert the nickel precursors into the NiO thin films make it expensive and not compatible with flexible substrates. Chavhan et al. reported a room-temperature approach to manufacture NiO_x films from a nickel formate precursor solution via UV-ozone treatment [175]. In terms of efficiency, the UV-ozone treatment results were ideal for increasing the WF by creating hydroxides at the surface, avoiding high processing temperatures. A high PCE of 6.1% in NiO_x HTL treated with UV-ozone was related to increased presence of NiO(OH) at the surface. Besides the precursor method, Jiang et al. used chemical precipitation to obtain non-stoichiometric NiO_x NPs at room temperature without any post-treatment [176]. The atomic ratio between Ni and O (1:1.14) reduced the R_s of the opto-electronic device as the *p*-type conductivity was enhanced by the presence of two oxidation states (Ni^{2+} and Ni^{3+}) that favor Ni^{2+} vacancies. Thus, the FF and the J_{sc} increased up to 67.20% and 9.67 $mAcm^{-2}$ to yield a PCE of 3.81% in P3HT-based conventional OSCs. The high performance of NiO_x NPs HTL-based OSCs was also demonstrated for low-bandgap polymers. Alternatively, *p*-type ternary metal oxides are promising candidates for enhancing electron-blocking ability due to their tunable electronic and optical properties through the hypocrystalline hydroxide-based method [177]. To date, the high surface roughness of fluorine-doped tin oxide (FTO) has limited its application in OSCs; however, the surface roughness can be decreased from 10.36 nm to 6.74 nm by fully covering it with an optimized NiO layer (see Figure 6) [178]. A polyethylene glycol (PEG) assisted sol-gel process altered the c-NiO/FTO surface because it has a stabilizing effect on NiO NPs, so it allowed the crystallization of a close-packed structure of NiO film. The further deposition of PEDOT:PSS led to the formation of a free-pinhole layer with an RMS roughness of 2.44 nm and selective hole transport, increasing the PCE from 5.68% to 7.93%. Although organic devices based on spin-coated NiO HTLs have emerged successfully in the photo-electronic field, it is vital to focus research efforts for printing technologies for

large-area roll-to-roll production. Printing technology usually results in thick NiO films, increasing the interfacing between the active and HTL layers and shortening hole carriers' migration due to its short lifetime [179]. Singh et al. obtained a thin film of NiO_x by controlling substrate-processing conditions and inkjet printing [180]. Optimal conditions of UVO pretreatment, drop spacing, and substrate temperature at 25 °C resulted in a PCE of 2.60% in the P3HT:PC₆₀BM cell with superior environmental stability. Huang et al. used copper (5.0 at.%) as a dopant to increase the electrical conductivity of NiO_x film, resulting in a reduction of R_s from 11.25 to 9.98 Ωcm² [181]. The Cu-doped NiO_x (Cu:NiO_x) also improved the interface contact with the active layer and facilitated the charge transport, resulting in a higher PCE of 7.1% in PCDTBT:PC₇₁BM-based cells. The enhancement in the optoelectronic properties, surface morphology, and stability of NiO_x HTL by doping is comparable with reported literature, as observed in the co-doping of NiO_x NPs with Li and Cu [182]. The co-doping favored the conductivity by increasing the Ni³⁺/Ni²⁺ ratio and kept the high transparency in the well-dispersed solution based on NiO_x NPs.

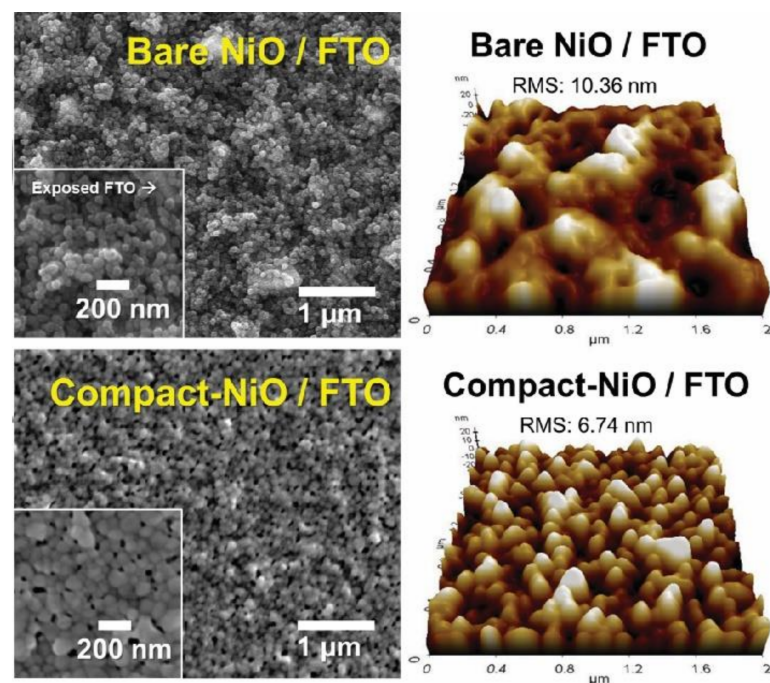


Figure 6. AFM and SEM images of bare nickel oxide on FTO (without PEG) and compact nickel oxide (c-NiO) on FTO (with PEG). Adapted with permission from [178].

4.1.5. Other Oxides

CuO_x are *p*-type semiconductors with narrow band gaps of 1.3–2.0 eV for CuO and 2.1–2.3 eV for Cu₂O [183–186]. HTLs of CuO_x spin-coated on ITO decreased the interfacial barrier using a green solvent of copper acetylacetonate (Cu(C₅H₇O₂)₂), improving cell efficiency of PTB7:PC71BM cell up to 8.68% [187]. After H₂O₂ and UVO treatment, CuO_x HTLs increased the WF to 5.45 eV, forming an excellent ohmic contact, while the V_{oc} increased to 0.74 V. Furthermore, the oxidation of CuO_x by UVO treatment enhanced the interfacial contact and the light absorption in the visible range, obtaining a high transmittance of 88%, low R_s of 2 Ωcm², and higher hole transport to the anode. The OSCs' initial performance (8.68%) dropped down to 47% over 50 h of storage in the air. The *p*-type CuCrO₂ is a semiconductor that belongs to the delafossite compounds [188]. CuCrO₂ HTLs are of great interest in optoelectronic applications due to their high transparency, large hole diffusion coefficient, high WF, and ionization energy, which are essential in the manufacture of OSCs [189–191]. Other strategies to boost the potential of CuCrO₂ HTL involve In doping, in which optical transmittance and hole conductivity are increased [192]. New alternative techniques to produce efficient and cost-effective CuCrO₂ HTLs for roll-

to-roll manufacturing are developing, such as microwave assisted-heating to produce CuCrO_2 nanocrystals with an efficient PCE of 4.9% [193], or the combustion synthesis to produce CuCrO_2 thin films by low-temperature processing at 180°C with a PCE of 4.6% (see Figure 7) [194]. Both methods are highly efficient and represent advances for lowering fabrication costs. UV-ozone post-treatment or annealing increases the metallic copper oxidation to Cu^{2+} to promote the electronic conduction by the hopping mechanism between Cu^{1+} and Cu^{2+} species. The higher oxidation state of Cu^{2+} enhanced the electronic properties, exhibiting deeper ionization energy (IE) and Fermi energy (E_F). The Cu doping favored the surface-roughness reduction, resulting in an improved interfacial contact, and thus favored J_{sc} , FF, and PCE.

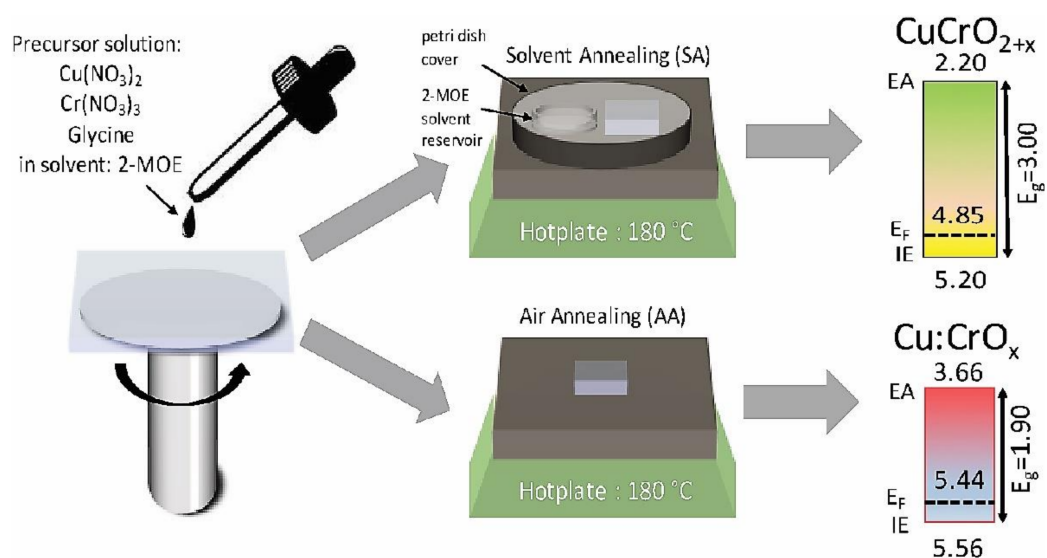


Figure 7. Schematic representation of the combustion synthesis. Adapted with permission from [194]. Copyright 2018, American Chemical Society.

Wahl et al. reported the first HTL based on ITO NPs in inverted OSCs [195]. The addition of ethylenediamine into ITO NPs stabilized it to deposit uniform HTLs on the underlying absorber layer. The deposition of the ITO NPs HTLs by doctor blading allowed controlling the thickness between 15 and 20 nm. Post-treatments of thermal annealing and plasma were beneficial for the film's electronic properties, achieving a PCE of 3%. However, plasma application needs to be mild to avoid OSCs' detrimental performance. The doping method using high-WF metals might be a good alternative over plasma treatments to develop high-quality films in OSCs. The solubility of metal oxides in common solvents such as DMF or water is another main factor for its application in the roll-to-roll manufacturing of OSCs. Bhargav et al. reported the suitability of DMF-soluble Co_3O_4 as HTLs in PCDTBT:PC₇₁BM BHJ [196]. Co_3O_4 HTLs showed transparency around 81% and a smooth surface, allowing for a remarkably high FF of 49.1% and higher PCE (3.21%) compared with PEDOT: PSS-based OPVs.

4.2. Metal Sulfides

4.2.1. Molybdenum Disulfide

MoS_2 with a layered structure is a metal dichalcogenide (TMD) semiconductor that can display two phases under normal conditions, the traditional trigonal prismatic H- MoS_2 phase and the distorted octahedral ZT- MoS_2 phase with hole mobilities of $3.8 \times 10^2 \text{ cm}^2\text{V}^{-1}\text{s}^{-1}$ and $5.7 \times 10^4 \text{ cm}^2\text{V}^{-1}\text{s}^{-1}$, respectively [197]. Instead of using a vacuum or temperature-dependent process to prepare the traditional MoS_2 HTL, Barrera et al. prepared suspensions of MoS_2 via liquid exfoliation at room temperature [198]. The high WF of MoS_2 resulted in enhanced charge mobility; however, the low transmittance of the film affected the J_{sc} . An effective way to address films' low transmittance is by using composites or hybrid layers

with tunable transparency. Martinez-Rojas et al. reported a hybrid layer of $\text{MoS}_x:\text{MoO}_3$ on FTO substrates with high transmittance by a pulsed electrochemical method [199]. After 150 cycles of depositing MoS_x on the MoO_3 , the percentage of transmitted light decreased significantly due to the agglomeration of MoS_x (see Figure 8a). A hybrid layer with 100 cycles of deposition resulted in 10% higher PCE than the one obtained using MoO_3 or MoS_x HTL. MoS_x was an efficient electron-blocking layer, while MoO_3 increased conductivity, resulting in enhanced hole-transporting properties. The effectiveness of UVO treatment to form homogeneous films and increase the WF was tested in a layer of MoS_2 quantum dots (QDs), showing a PCE of 2.62% and 8.7% for P3HT and PTB7-Th donor systems [200]. The solar cell efficiency increased after 30 min of UVO exposure, but longer UVO treatment periods degraded the HTL, resulting in decreased PCEs (see Figure 8b). The UVO- MoS_2 QDs showed compact and uniform layers with a lower surface roughness of 1.19 nm than UVO- MoS_2 nanosheets of 2.03 nm. The OSC achieved long-term durability due to the improved interfacial contact, showing 64% of its initial PCE after 47 days (see Figure 8c). Annealing treatments can also decrease the surface roughness and favor the optoelectronic properties of the film. At 300 °C, MoS_x flattened the surface morphology, enhancing the PCE by up to 7.5%, 52% of which was retained after two months [201]. However, an annealing treatment is not as efficient as a UVO treatment for temperature-sensitive devices.

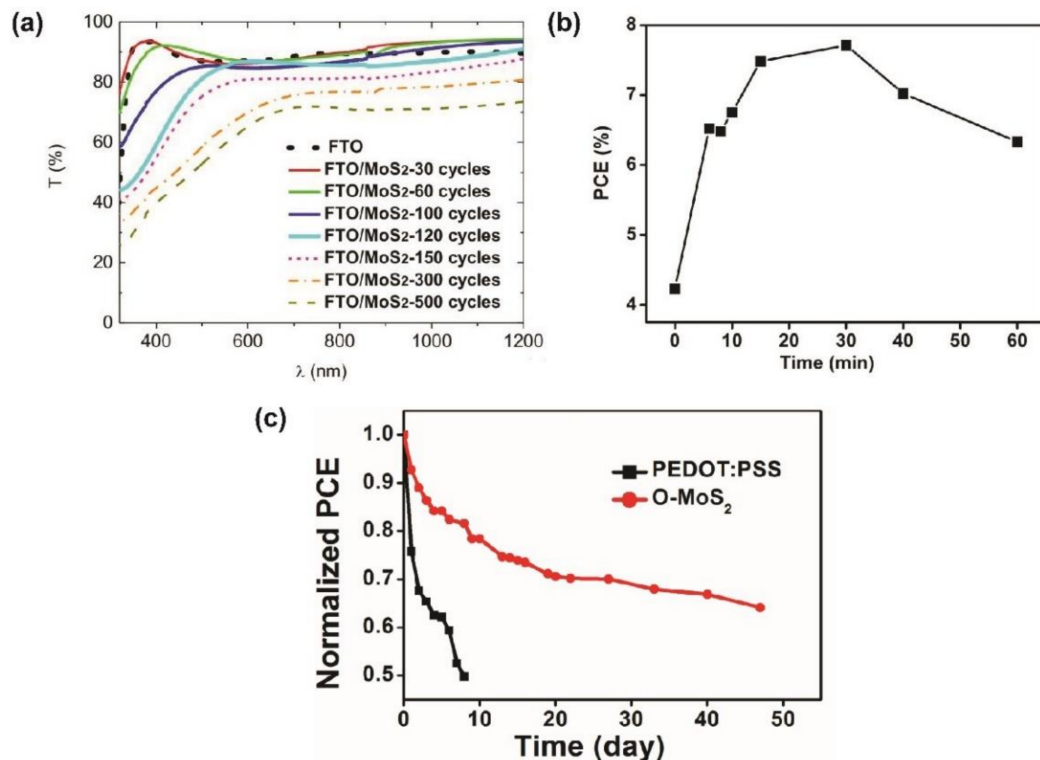


Figure 8. (a) Transmission spectra of FTO/ MoS_2 at various numbers of scan cycles. Adapted with permission from [199]. Copyright 2017, Elsevier. (b) Dependence of PCE on the duration of the UVO treatment and (c) stability of devices using UVO- MoS_2 QDs compared with PEDOT:PSS. Adapted with permission from [200]. Copyright 2016, American Chemical Society.

4.2.2. Tungsten Disulfide

Adilbekova et al. used a liquid-phase exfoliation technique to manufacture WS_2 HTL using aqueous ammonia that does not require high-temperature post-treatments [202]. Stabilizers or post-processing treatments were excluded from obtaining WS_2 nanosheets since stoichiometric quality and structural properties were unchanged after performing the top-down method. Due to the *p*-type character of the 2D nanosheets, the HTLs were selective to hole transport toward the anode, achieving a PCE of 15.6% in the PBDBT-2F:PC₇₁BM BHJ cells. Following the same line, Lin et al. fabricated uniform WS_2 layers on

ITO [203]. WS₂ flakes were wider and thinner than MoS₂, covering the whole surface of ITO. The surface coverage was dependent on the shape and size of the selected material obtained by the exfoliation procedure and its interaction with the substrate. WS₂-based HTL in ternary BHJ OSCs (PBDB-T-2F:Y6:PC₇₁BM) increased PCE by up to 17%. Ram et al. demonstrated that the use of WS₂ as HTL increased the PCE of PBDB-T-2F:Y6:SF(BR)₄ ternary cells by 20.87% [204]. The low hygroscopic nature and low acidity of WS₂ reduced the contact resistance between the active layer and the ITO.

4.2.3. Nickel Sulfide

Taking advantage of the dependence of the phase diagrams of NiS with the sulfur content, Hilal and Han synthesized the hexagonal phase of NiS as HTL in OSCs processed by the simple solvothermal method at room temperature [205]. The surface morphology of NiS was smoothed by increasing the sulfur content to 2 g, forming a globular flower-like NiS morphology with increased surface area (see Figure 9). In addition to the enhancement in the hole transport, NiS stabilized the OSC; hence, P3HT:PCBM-based cells retained 26% of their initial efficiency value after 15 days.

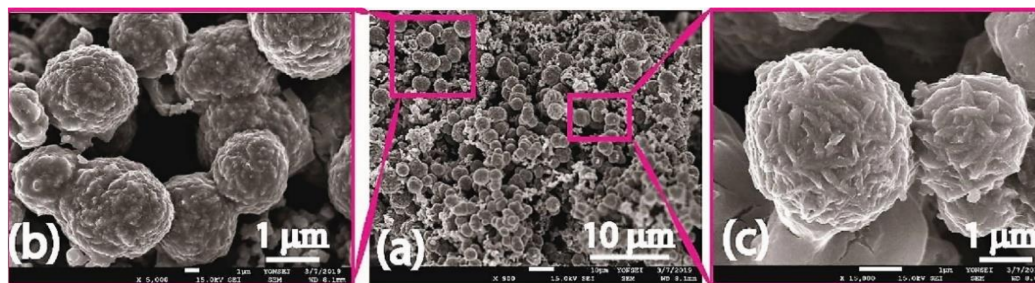


Figure 9. FE-SEM images of globular flower-shaped NiS at magnifications of (a) 10 μm and (b,c) 1 μm . Adapted with permission from [205]. Copyright 2019, Elsevier.

4.2.4. Other Sulfides

An efficient OSC was achieved by Bhargav et al. using an inorganic HTL made of CuS by a low-cost and efficient manufacturing process [206]. CuS thin films were deposited onto ITO by a solution process instead of vacuum deposition, resulting in a high transparency of 84%. Due to the decreased ohmic resistance, the device structure ITO/CuS/PTB7:P₇₁BM/Al reached a high PCE of 4.32% due to the improved FF of 50.1%. A new room-temperature method known as Successive Ionic Layer Adsorption and Reaction (SILAR) was reported by Jose et al. to produce efficient *p*-type Zn-doped CuS HTLs [207]. Due to the high conductivity and low light absorption in the visible region, a PCE of 1.87% was obtained with enhanced charge mobility of 1.5 cm² V⁻¹s⁻¹. The use of 2D materials like antimonene quantum dots (AMQS) in HTLs has emerged in OSCs production due to their facile synthesis and unique properties [208]. Wang et al. reached an enhanced PCE of 8.8% by the surface passivation of copper(I) thiocyanate (CuSCN) HTL with AMQs [209]. The AMQs smoothed the film surface of CuSCN, tuned the WF, and raised the exciton generation rate from 8.79 $\times 10^{27}$ m⁻³s⁻¹ to 9.95 $\times 10^{27}$ m⁻³s⁻¹. Compared with PEDOT:PSS HTLs, CuSCN/AMQs HTLs were more stable at room temperature, retaining 68% of the initial PCE over 1 month not only in fullerene systems such as PTB7- Th:PC₇₁BM, but also in non-fullerene systems. Other strategies involving triple-interface passivation [210], multifunctional interface layer using lead sulfide quantum dots (QDs) [211], and self-polymerization of the monomer have been also reported to passivate surface roughness and interface defects [212]. The surface passivation is key in the construction of OSCs to reduce non-radiative recombination losses which in turns affect the charge separation rate once excitons achieve the donor/acceptor interface, resulting in a low V_{oc} and FF. The *p*-doping of CuSCN with C₆₀F₄₈, an electron acceptor, is an effective method to obtain highly conductive HTLs for its application in OSC devices [213]. By adding 0.5 mol% of C₆₀F₄₈ that also acts as a nucleating agent, the CuSCN:C₆₀F₄₈ film was more dense than the pristine

CuSCN surface. Moreover, reduced surface roughness, leakage current (see Figure 10a), and improved hole mobility of $0.18 \text{ cm}^2\text{V}^{-1}\text{s}^{-1}$ were attributed to the percolation conduction mechanism, resulting in a PCE of 6.6% in the PCDTBT:PC₇₀BM-based OSCs. Wang et al. achieved a PCE of 15.28% in OSCs based on the non-fullerene PM6:Y6 blend by doping CuSCN film with 1% of TFB (see Figure 10b) [214]. Worakajit et al. increased the hole mobility in CuSCN from 0.01 to $0.05 \text{ cm}^2\text{V}^{-1}\text{s}^{-1}$ by passivating surface morphology and the crystallinity with diethyl sulfide (DES) molecules and acetone as antisolvent treatment [215]. Suresh Kumar et al. succeeded in fabricating Cu₂CdSnS₄ (CCTS) HTLs over ITO substrates deposited by spin coating at room temperature [216]. A PCE of 3.63% in the P3HT:PC₇₁BM blend was achieved by controlling the distribution particle size. The bandgap decreases with an increase in the size of CCTS and layer thickness. Minimum surface roughness of 11.07 nm was found after deposition of three layers of CCTS thin films, improving the thin film's compactness, hole-transport efficiency, and stability in environmental conditions.

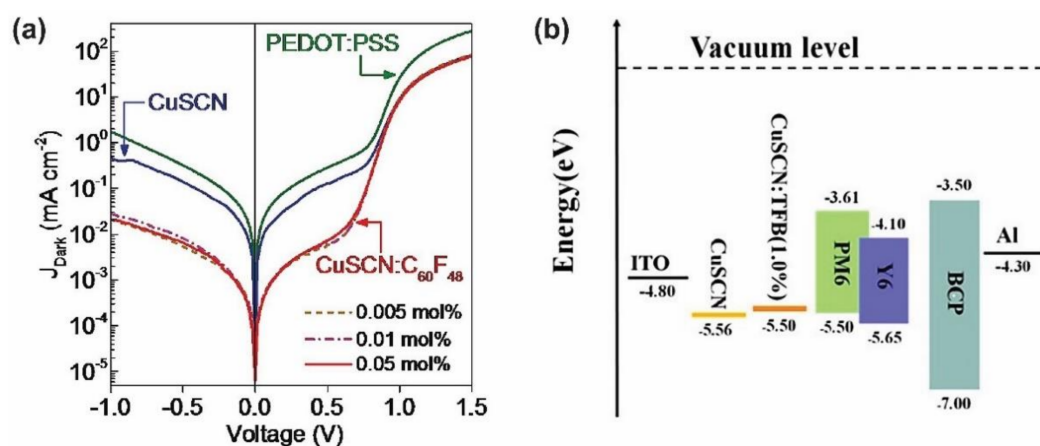


Figure 10. (a) J-V curves of CuSCN:C₆₀F₄₈ under dark conditions. Adapted with permission from [213]. Copyright 2018, John Wiley and Sons. (b) Energy level alignment of ITO/CuSCN, CuSCN:TFB(1.0%)/PM6:Y6/BCP/Al OSCs. Adapted with permission from [214]. Copyright 2020, American Chemical Society.

4.3. Nanocarbons

4.3.1. Graphene Oxide

Nanocarbon materials like graphene have been applied as HTLs in OSCs due to their unique electrical, optical, and structural properties [217]. Due to the low water dispersibility caused by the nonpolar sp^2 hybridized carbon structure, the oxidized form of graphene, graphene oxide (GO), has also been used in OSCs by the high solubility in eco-friendly water solvents [218]. The hydroxyl groups and epoxy groups located in the basal plane of the graphene sheet and carboxylic acids at the edge limit the conductivity of GO [219]. In fact, an excess of 25% of oxygen atoms on the GO sheet's surface reduced its conductivity until it became an insulator material [220]. Thus, it is crucial to control the concentration and thickness of GO for suitable performance as HTLs. Rafique et al. tested the thickness and concentrations of spin-coated GO, selecting 1 mg/mL to form thin conductive films in BHJ OSCs with a PCE of 2.73% [221]. The reduction process is another feasible way to increase the conductivity of GO layers. The reduction removes the excess of oxygen atoms from the GO surface and recovers the conjugated honeycomb structure [222]. Huang et al. succeeded in synthesizing eco-friendly reduced graphene oxide (rGO) by using a modified Hummer's method to produce GO and thermal treatment to reduce it [223]. A mild temperature of 280 °C was used to obtain rGO and enhance OSCs' conductivity based on P3HT:PC₇₁BM and PTB7:PC₇₁BM with a PCE of 3.39% and 7.62%, respectively. The dispersibility must be controlled to ensure good coverage of the underlying substrate. Lee et al. mixed highly dispersible semiconducting fullerene surfactant with GO, obtaining water-dispersible and conductive films [224]. The conductivity increased from $5 \times 10^{-4} \text{ Scm}^{-1}$ for the pristine GO

layer to $1 \times 10^{-2} \text{ Scm}^{-1}$ for the fullereneol-GO layer, resulting in a PCE of 3.15%. Chemical and physical methods involving the reduction of GO seek to tune the WF, improve electrical properties, reduce absorption, and increase hole mobility and charge collection capability. Kwon et al. obtained rGO by electron-beam irradiation with shorter processing times than reported gamma (γ)-rays [225]. Following the same line, Fakharian et al. applied a YAG-pulsed laser to produce rGO in formic acid for OPVs with a PCE of 4.02% [226]. They also highlighted the solvent's role in manufacturing devices to achieve an rGO with superior physical and electrical features. Unlike the traditional chemical-reduction methods, pulsed laser or electron-beam allowed the reduction of graphene over the in-situ formation of reducing species selectively. Dericiler et al. reported graphene nanosheets prepared from the electrochemical exfoliation of graphene powder followed by dispersion in DMF solvent [227]. They used the graphene nanosheets suspension as an additive to PEDOT:PSS HTLs to enhance the stability and charge mobility in the P3HT:PC₆₀BM, achieving 66% enhancement in the PCE compared with the reference cell based on pure PEDOT:PSS HTLs.

The application of UVO irradiation has shown excellent efficiency in reducing GO in large-scale OSCs manufacturing. Xia et al. [228] and Rafique et al. [229] exposed GO to UVO treatment, resulting in optimized performance in P3HT:PC₇₁BM and PCDTBT:PC₇₁BM blend systems. UVO oxidizes the surface of GO and removes CO₂ molecules, leaving a uniform, smoothed, and conductive film. Ultraviolet irradiation was controlled to remove only C-O bonds from the GO surface. UVO-treated GO films allowed for exceeding the value of FF and J_{sc} obtained from PEDOT:PSS. Taking advantage of graphene's chemical structure, the functionalization is very promising for obtaining desirable properties in HTLs, such as high hole mobility, charge collection, transparency, and stability, among others. Zhao et al. fabricated highly stable P3HT:PC₇₁BM-based OSCs with a PCE of 3.56% by forming covalent bonds between graphene and sulfanilic acid through C-N linkers [230]. The covalent functionalization increased the WF that enhance the interface's charge transport and the overall photovoltaic characteristics (see Figure 11a). Ali et al. confirmed the potential for tuning the bandgap and electrical properties when reduced and sulfonated GO films were applied as HTLs for a wide range of donor-acceptor systems [231]. Other approaches like non-covalent phosphorylation and fluorination have been remarkably effective in enhancing the charge collection and transport via inducing low ohmic contact [232,233]. The presence of the phosphate ester or fluor in the surface of GO increased the WF of ITO/GO and tuned the HOMO level of the donor by the p-doping effect. Fluorinated GO (F₅-GO) was reported to work as an interlayer between ITO and PEDOT:PSS [234]. This material improved hole transport, resulting in a low R_s of 2 Ωcm^2 and a PCE of 7.67% for PTB7:PC₇₁BM-based OSCs. Park et al. reported an orthogonal printable HTL by spray casting a highly stable dispersion of fluorine-functionalized reduced graphene oxide (FrGO) [235]. By decreasing the sheet size to 0.3 μm , the PCE increased to 9.27 and 9.02% for PTB7-Th:EH-IDTBR and PTB7-Th:PC₇₁BM-based OSCs, respectively. This improvement was attributed to the hole-transport efficiency, decreased leakage current, and higher conductivity of the FrGO layers. Zhen et al. reported graphene-MoS₂ hybrid thin films via liquid-phase graphene exfoliation, improving the charge transportation as an interlayer to achieve a PCE 9.5% [236]. This interlayer increased the device stability by retaining 93% of the initial PCE after 1000 h at room temperature. Shoyiga et al. reported reduced graphene oxide-anatase titania (RGOT) nanocomposites by hydrothermal synthesis [237]. RGOT HTL is an efficient charge-transport channel whose higher conductivity and exciton dissociation efficiency decreased the rates of electron-hole recombination (see Figure 11b), resulting in a high J_{sc}, low R_s, and, thus, improved photovoltaic performance.

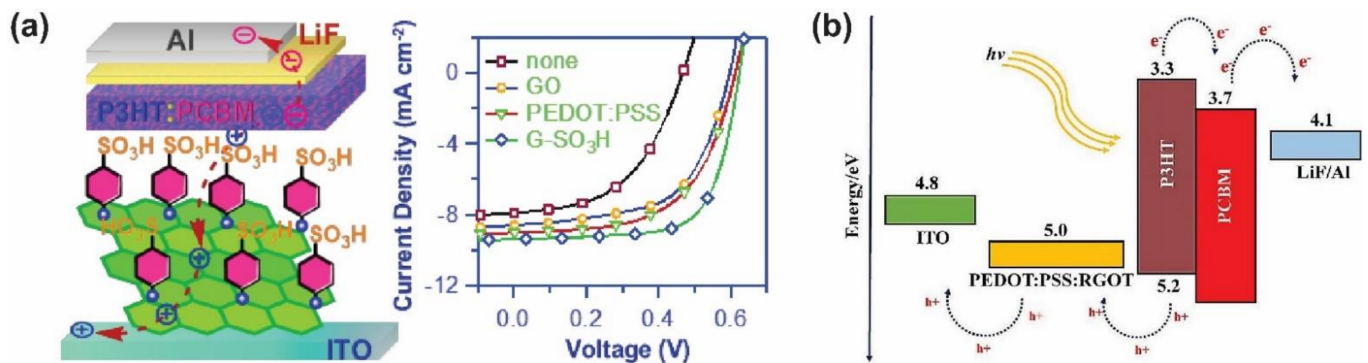


Figure 11. (a) J-V curve of the OSCs with G-SO₃H films as HTL. Adapted with permission from [230]. Copyright 2018, American Chemical Society. (b) Energy level diagram of an OSC with RGOT-modified HTL. Adapted with permission from [237]. Copyright 2020, John Wiley and Sons.

Lee et al. improved the performance of rGO by chemical doping with tetrafluorotetracyanoquinodimethane (F₄TCNQ) [238]. The *p*-doping of rGO with F₄TCNQ increased the WF by 0.2 eV and the conductivity by inducing charge transfer between the F₄TCNQ and the graphene layer. F₄TCNQ enhanced the interchain interaction and crystallization of the P3HT film to improve the hole mobility from the active layer to the anode. Lee et al. [239] and Sun et al. [240] reported that GO modified with alkali chlorides such as AuCl₃ or CuCl₂ dopants in a conventional architecture exhibited an average PCE of 3.77% and 7.68%, respectively. The AuCl₃-doped graphene increased the electrical conductivity ($\sim 2.0 \times 10^5 \text{ Sm}^{-1}$) compared with the reported fullerene-rGO layer ($1 \times 10^{-2} \text{ Scm}^{-1}$). GO:CuCl₂ layers formed a uniform and continuous film. Although the efficiency achieved by the dopants is even comparable to that of the control devices with PEDOT:PSS, the stability was superior. Graphene-based derivatives (GBD) do not corrode the metal substrate as PEDOT:PSS, leading to the development of OSCs' efficient performance by controlling the properties and deposition conditions of GBD as reported by Capasso et al. [241]. Sarkar et al. embedded Au NPs into GO for increasing the light trapping in the active layer [242]. The exerted plasmonic effect and the plasmon-exciton interaction of NPs increased the light harvested by the active layer, resulting in enhanced J_{sc} and PCE. Besides, the enhanced conductivity of GO helped to reduce the leakage current, thereby improving the photogenerated current, R_s, and FF of the device. A composite of 1 wt% of graphene nanosheet and water-dispersible polyaniline-poly(2-acrylamido-2-methyl-1-propanesulfonic acid) complex was used as HTL in OSCs [243]. The graphene nanostacks (GN) from the composite penetrated the BHJ of the OSC and facilitated the charge transport by forming additional pathways (see Figure 12a). The electric field generated from the edges of the GN increased the exciton dissociation. As a result, the composite performance raised the PCE from 2.12% (PANI) to 2.92% (G-PANI) in the P3HT:PC₇₀BM cells. Aatif et al. also reported the surface morphology's planarization after applying GO/molybdenum composite, resulting in a PCE of 5.1% with the PCDTBT:PC₇₁BM-based OSCs [244]. Quasi-3D GO:NiO_x nanocomposites are potential *p*-type HTLs in ITO/ZnO/PTB7-Th:PC₇₁BM/HTL/Ag architectures [245]. Using the solvothermal method, NiO_x NPs interacted with the low oxidized form of GO by hydrogen bonds to form the quasi-3-D arrangement (see Figure 12b). The high performance of these nanocomposite HTLs is due to the enhanced vertical conductivity with low recombination rates and enhanced electron-blocking ability by the small conduction band of NiO_x NPs (1.55 eV) (see Figure 12c). The metallic nature of NiO_x NPs improved the stability by retaining half of the initial PCE (12.3%) in environmental conditions. Dang et al. reported a solution-processed hybrid graphene-MoO₃ (G-MoO₃), via the hydrothermal method, to apply as HTL in OSCs [246]. The G-MoO₃ exhibited higher transparency in the visible region compared with the thermal-evaporated MoO₃. Moreover, the low injection barrier (0.2 eV) and the higher hole mobility in G-MoO₃ ($4.16 \times 10^{-5} \text{ cm}^2\text{V}^{-1}\text{s}^{-1}$) than in MoO₃ ($1.25 \times 10^{-5} \text{ cm}^2\text{V}^{-1}\text{s}^{-1}$) were beneficial to achieve a PCE of 7.07%. The rGO and pery-

lene derivative 3,4,9,10-perylenetetracarboxylic dianhydride (PTCDA) nanohybrid HTL showed an increased cell performance up 4.70% in PBDTTT-CT:PC₇₁BM-based cells [247]. The rGO:PTCDA nanohybrid HTL formed permanent dipoles by the PTCDA_rGO bond formation, increasing the hole extraction, electrical conductivity, and tuning the WF.

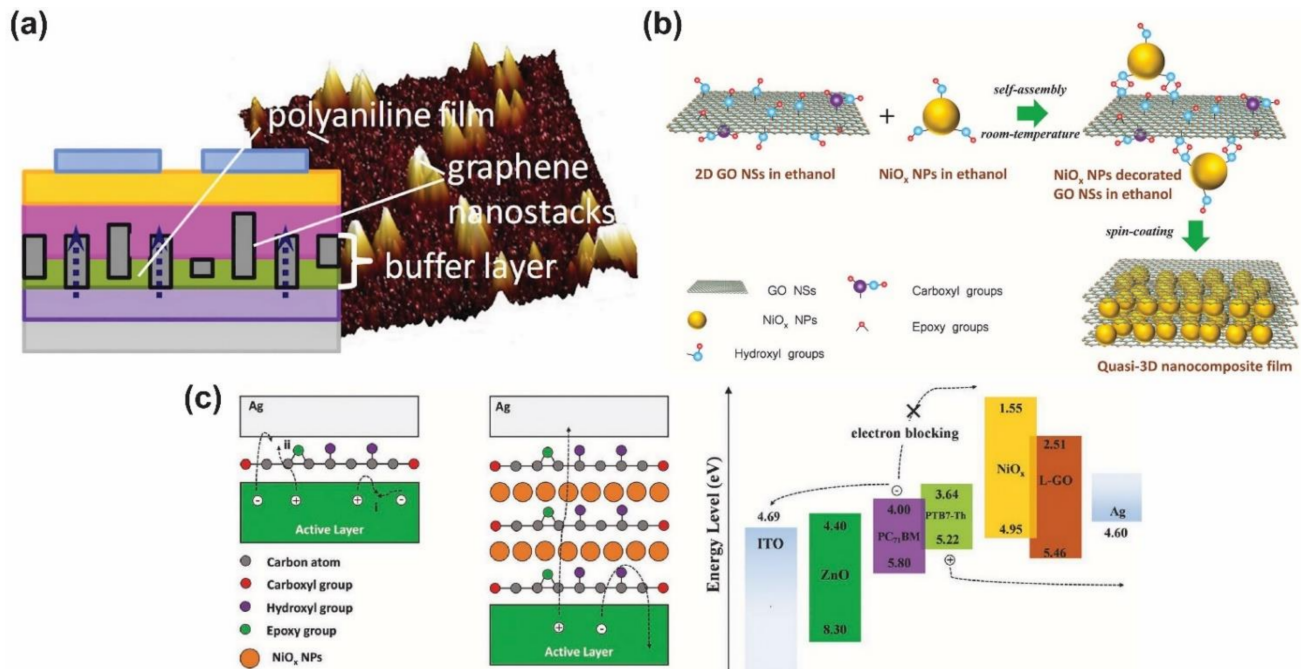


Figure 12. (a) Topography AFM-images of G/PANI-PAMPSA nanocomposite layer. Adapted with permission from [243]. Copyright 2018, Elsevier. (b) Schematic representation of the preparation at room temperature of self-assembled quasi-3D GO:NiO_x nanocomposite and (c) hole extraction properties and dynamics at the interface. Adapted with permission from [245]. Copyright 2018, John Wiley and Sons.

4.3.2. Other Nanocarbons

The production efficiency of graphene quantum dots (GQDs) in the photovoltaic field has been limited by the expensive manufacturing methods, materials availability, and the time-consuming manufacturing [248,249]. However, the development of green and low-cost methods, such as the synthesis of GQDs from carbon fibers by acid treatment and chemical exfoliation or doping with nitrogen, has boosted its potential application in the fabrication of large-area OSCs [250]. Hoang et al. succeeded in the green synthesis of GQDs from graphene using the microwave-assisted hydrothermal method for 10 min [251]. An enhancement of 44% in PCE was achieved by doping the active layer with 2 mg of GQDs. The GQDs filled the interstitial positions between P3HT and PC₆₀BM to increase the charge transport of holes and electrons and the photocurrent generation. Zhang et al. reported amino-functionalized multi-walled carbon nanotubes (a-MWNTs), via hydrothermal synthesis, as HTLs in conventional OSCs with the configuration ITO/a-MWNTs/PCDTBT/PC₇₁BM/LiF/Al [252]. Compared with the carboxylic acids, the amino functionalization reduced the defects and the resistivity of a-MWNTs (see Figure 13a). The a-MWNTs enhanced the device's charge mobility, collection, and performance by 6.9%. Single-walled carbon nanotubes (SWCNTs) are promising *p*-type transparent conductors owing to their superior hole mobility, conductivity, and facile tuning of the WF by doping method [253]. A highly-conductive composite of unzipped single-walled carbon nanotubes (u-SWNTs) and PEDOT:PSS was synthesized by a facile solution processing method as reported by Zhang et al. (see Figure 13b) [254]. The hybrid PEDOT:PSS doped with u-SWNTs decreased the surface roughness. Oxygen-containing groups of u-SWNTs improved the compatibility between u-SWNTs and PEDOT:PSS to block electrons and increase the hole

transport. Using 0.1 mg mL^{-1} of u-SWNTs, the conductivity of the uSWNTs/PEDOT:PSS increased to 2.08 Scm^{-1} . The R_s was insensitive to the layer thickness, resulting in improved charge-carrier transport through the gap of u-SWNTs (see Figure 13c). Thus, PBDB-T-2F:IT-4F devices with u-SWNTs/PEDOT:PSS HTLs exhibited an enhancement in the PCE from 13.72% to 14.60% (see Figure 13d).

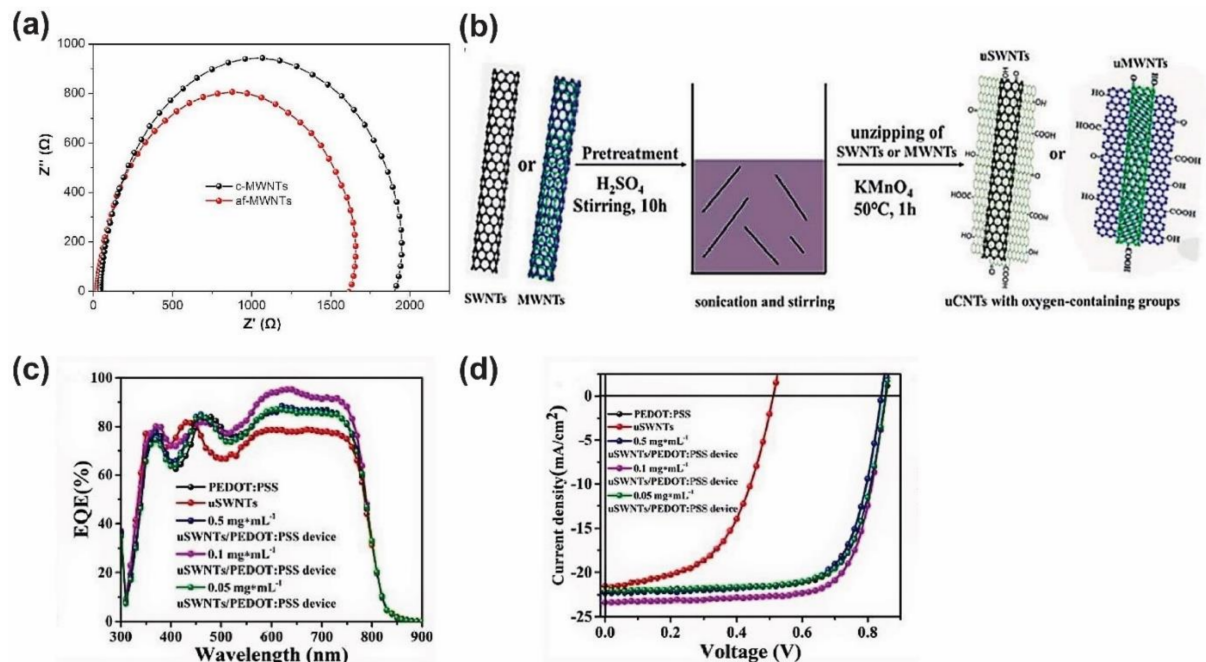


Figure 13. (a) Impedance spectra of OSCs with c-MWNTs and af-MWNTs HTLs. Adapted with permission from [252]. Copyright 2019, Elsevier. (b) Schematic representation of u-SWNTs and u-MWNTs synthesis, (c) EQE of u-SWNTs, SWNTs, and PEDOT:PSS, and (d) J-V curves of the OSCs with u-SWNTs HTLs. Adapted with permission from [254]. Copyright 2020, Royal Society of Chemistry.

Table 1 enlists a series of HTLs reviewed up to this point. The anode configuration with its work function, deposition technique for the HTL, active layer composition, and the OSCs performance parameter such as V_{OC} , J_{SC} , FF, and PCE are provided as well as the reference where the information is available.

Table 1. Performance parameters of OSCs with inorganic films as HTLs.

Anode Configuration and WF (eV)	Deposition Technique	Active Layer	V_{OC} (V)	J_{SC} (mA cm^{-2})	FF (%)	PCE (%)	Ref.
<i>Metallic oxides</i>							
ITO/s-MoO ₃ (4.92)	spin coating	PBDB-T-2F:Y6	0.84	27.53	73.10	17.00	[107]
ITO/PCM4 (5.4)	blade coating	PBDB-T-2F:Y6	0.83	16.06	68.28	14.30	[119]
HVO/Ag (6.7)	spin coating	PBDTT-FTTE:PC71BM	0.82	22.51	60.19	11.14	[159]
ITO/MoO ₃ (5.3)	spin coating	PBDB-T:PC71BM	0.88	17.48	71.00	10.86	[102]
MoO ₃ :NiO _x (5.1)	spin coating	PBDB-T:IT-M	0.94	17.26	66.63	10.81	[113]
e-MoO _x /Ag (5.4)	spin coating	PTB7-Th:PC71BM	0.79	18.70	69.20	10.42	[99]
VO _x :PEDOT:PSS/Ag (5.28)	spin coating	TPD-3F:IT-4F	0.87	16.80	69.10	10.10	[164]
MoO ₃ /AgAl/MoO ₃ /AgAl	thermal evaporation	PTB7-Th:PC71BM	0.78	19.60	61.90	9.79	[100]
CuBr-MoO ₃ /Ag (5.03)	thermal evaporation	PTB7:PC71BM	0.75	19.65	65.20	9.56	[117]
MoO _x NPs/Ag (5.40)	spin coating	PTB7-Th:PC71BM	0.79	18.05	65.20	9.50	[99]
ITO/MoO ₃ (5.29)	spin coating	PBDB-T:ITIC	0.91	15.19	66.59	9.17	[106]
ITO/NiO _x NPs(5.25)	spin coating	PTB7-Th:PC71BM	0.79	18.32	63.10	9.16	[176]
ITO/s-MoO ₃ (4.92)	spin coating	PTB7-Th:PC71BM	0.79	16.69	67.10	8.90	[107]
ITO/CuO _x (5.06)	spin coating	PTB7:PC71BM	0.74	16.44	71.00	8.68	[187]
MoO ₃ /Ag (5.52)	thermal evaporation	PTB7-Th:PC70BM	0.81	15.90	67.80	8.67	[98]

Table 1. Cont.

Anode Configuration and WF (eV)	Deposition Technique	Active Layer	V _{OC} (V)	J _{SC} (mA cm ⁻²)	FF (%)	PCE (%)	Ref.
ITO/p-MoO ₃ (5.26)	spin coating	PTB7:PC71BM	0.73	17.02	68.10	8.46	[104]
ITO/CTAB-MoO ₃ (5.18)	spin coating	PTB7:PC71BM	0.72	16.88	68.10	8.34	[118]
ITO/VO _x ·nH ₂ O (5.0)	spin coating	PTB7-th:PC71BM	0.78	15.76	64.62	8.11	[156]
ITO/V ₂ O ₅	spin coating	PTB7:PC70BM	0.71	17.35	65.00	8.05	[154]
ITO/NiO _x NPs(5.25)	spin coating	PTB7:PC71BM	0.74	16.10	66.42	7.96	[176]
ITO/NP-V ₂ O ₅ (4.7)	spin coating	PTB7:PC70BM	0.72	15.81	69.01	7.89	[165]
WO _x nanosheets/Ag	spin coating	PTB7: PC71BM	0.81	16.42	58.19	7.76	[150]
ITO/s-VO _x (5.3)	spin coating	PTB7:PC71BM	0.73	15.79	66.82	7.70	[160]
ITO/MoO ₃ /AuNPs/MoO ₃ (5.6)	spin coating	PTB7:PC70BM	0.73	14.40	73.00	7.68	[122]
ITO/ESD-VO _x (5.6)	spray casting	PTB7:PC71BM	0.74	15.30	67.00	7.61	[168]
ITO/V ₂ O _x (5.42)	spin coating	PBDTDTT-S-T:PC71BM	0.68	16.29	67.21	7.44	[114]
ITO/MoO _x (5.30)	spin coating	PBDTDTT-S-T:PC71BM	0.69	16.14	66.02	7.35	[114]
ITO/sMoO _x	spin coating	PV10:PC70BM	0.73	13.57	72.55	7.19	[101]
FTO/Cu:NiO _x	spin coating	PCDTBT:PC71BM	0.89	12.40	63.85	7.05	[181]
FTO/c-NiO (5.0)	spin coating	PTB7:PC71BM	0.72	14.28	66.98	6.91	[178]
ITO/MoO _x	thermal evaporation	PTB7:PC71BM	0.67	14.00	67.00	6.57	[103]
ITO/H _y MoO _{3-x} (5.6)	spin coating	PTB7:PC70BM	0.77	13.90	61.20	6.55	[129]
ITO/NiO _x NPs(5.25)	spin coating	PCDTBT:PC71BM	0.90	11.36	62.35	6.42	[176]
ITO/NiO _x (5.6)	spin coating	TQ1:PC70BM	0.87	10.30	71.30	6.39	[175]
ITO/s-V ₂ O _x (5.25)	spin coating	PFDT2BT-8:PC70BM	0.87	10.20	67.10	6.30	[162]
V ₂ O _x /Ag (5.42)	spin coating	PBDTDTT-S-T:PC71BM	0.63	15.81	61.02	6.08	[114]
MoO _x /Ag (5.30)	spin coating	PBDTDTT-S-T:PC71BM	0.61	15.68	62.78	6.00	[114]
ITO/V ₂ O ₅ ·H ₂ O (5.04)	spin coating	PBDSe-DT2PyT:PC71BM	0.72	13.96	59.00	5.87	[155]
ITO/CTAB-MoO ₃ (5.18)	spin coating	P3HT:ICBA	0.82	10.40	67.40	5.80	[118]
ITO/MoO _x	thermal evaporation	PTB7-Th:PC71BM	0.74	14.50	44.80	5.52	[103]
FTO/s-MoO ₃ (5.3)	spin coating	P3HT:ICBA	0.82	11.50	58.00	5.40	[105]
FTO/MoO _x (5.6)	spin coating	P3HT:PC71BM	0.65	12.72	61.00	5.00	[110]
<i>Metallic sulfides</i>							
ITO/WS ₂ (5.3)	spin coating	PBDB-T-2F:Y6:SF(BR) ₄	0.89	29.31	80.00	20.87	[204]
ITO/WS ₂ (5.5)	spin coating	PBDB-T-2F: Y6: PC71BM	0.84	26.00	78.00	17.00	[203]
ITO/WS ₂ (5.1)	spin coating	PBDB-T-2F:Y6:PC71BM	0.83	26.00	72.00	15.60	[202]
ITO/CuSCN:TFB (1.0%) (5.50)	spin coating	PM6:Y6	0.85	24.35	73.84	15.28	[214]
ITO/MoS ₂ (5.04)	spin coating	PBDB-T-2F:Y6:PC71BM	0.81	25.30	71.00	14.90	[202]
ITO/CuSCN:AMQS	spin coating	PBDB-T-2F:IT-4F	0.80	18.70	67.80	10.14	[209]
ITO/CuSCN:AMQS	spin coating	PTB7-Th:PC71BM	0.79	17.10	65.20	8.80	[209]
ITO/O-MoS ₂ QDs (5.2)	spin coating	PTB7-Th: PC71BM	0.79	16.90	65.00	8.66	[200]
ITO/MoS _x (5.10)	spin coating	PTB7-Th: PC71BM	0.77	18.16	53.56	7.50	[201]
ITO/CuSCN:AMQSS	spin coating	PTB7-Th:ITIC	0.82	15.07	59.06	7.15	[209]
ITO/CuSCN:C ₆₀ F ₄₈ (5.40)	spin coating	PCDTBT:PC70BM	0.92	11.50	61.00	6.60	[213]
<i>Nanocarbon materials</i>							
ITO/uSWNTs/PEDOT:PSS	spin coating	PBDB-T-2F:IT-4F	0.85	23.39	73.17	14.60	[254]
ITO/FrGO (4.9)	spray casting	PM6:Y6 PSC.	0.77	24.64	69.60	13.26	[235]
L-GO:NiO/Ag	spin coating	PBDB-T:IT-M	0.91	17.81	71.00	12.13	[245]
G-MoS ₂ /Ag (4.42)	spin coating	PTB7-Th:PC71BM	0.80	17.10	67.70	9.50	[236]
ITO/G-MoS ₂ /PEDOT:PSS (5.0)	spin coating	PTB7-Th:PC71BM	0.77	17.20	72.00	9.40	[236]
ITO/FrGO (4.9)	spray casting	PTB7-Th:EH-IDTBR	1.00	14.86	61.80	9.22	[236]
ITO/FrGO (5.1)	spin coating	PTB7-Th:PC71BM	0.79	16.89	64.80	8.60	[233]
ITO/P-GO (4.70)	spin coating	PTB7:PC71BM	0.71	16.12	68.40	7.90	[232]
ITO/GO:CuCl ₂ (5.1)	spin coating	PTB7-Th:PC71BM	0.79	15.52	63.00	7.74	[240]
ITO/G-MoO ₃ (5.32)	spin coating	PCDTBT:PC71BM	0.86	12.83	63.67	7.07	[246]
af-MWNTs (5.22)	spin coating	PCDTBT:PC71BM	0.87	12.65	63.50	6.97	[252]
ITO/GO:NPs (4.9)	spin coating	PTB7:PC71BM	0.75	11.55	67.91	5.88	[242]
ITO/F ₅ -rGO (5.1)	spin coating	PTB7:PC71BM	0.68	14.78	57.30	5.82	[234]
ITO/GBD (4.9)	spin coating	PBDT-T-C-T:PC70BM	0.71	13.38	52.54	5.01	[241]
ITO/GO:MoO ₃ (5.3)	spin coating	PCDTBT:PC71BM	0.66	16.16	47.11	5.10	[244]

4.4. Conducting Polymers and Their Composites

4.4.1. PEDOT

PEDOT:PSS is the most common conducting polymer used as hole-transporting material in OSCs due to its easy solution processing, suitable WF around 5.1 eV, high conductivity, good transparency, good mechanical properties, and adapted wettability on the BHJ layer [255]. For instance, a patterning interfacial PEDOT:PSS layer formed by a nanoimprint-

ing technique using poly(dimethylsiloxane) (PDMS) stamp was employed on OSCs based on poly(3-hexylthiophene):phenyl-C61-butyric acid methyl ester (P3HT:PCBM), showing an increased PCE of 1.53% [256]. PEDOT:PSS was incorporated on an inverted OSC based on P3HT:O-IDTBR with an evaporated Ag back electrode, showing an enhanced device performance [257]. The incorporation of PEDOT:PSS into P3HTN:PEG-C₆₀ based OSCs increased the V_{oc} to 1.3 V, attributed to the large collection barrier [258]. PEDOT:PSS has strong acidic nature due to the polystyrene sulfonate (PSS, pH~2), which deteriorates the anode material and the photoactive layer, affecting the performance and stability of the device. Besides, this polyelectrolyte has high affinity for environmental water (hygroscopic), making it necessary to encapsulate the OSC's before the durability test. Humidity is a major problem in this type of device. Accordingly, different modifications to the PEDOT:PSS layer have been developed to overcome these issues. Some post-treatments to the PEDOT:PSS layer have been tested using solvents, surfactants, and by exchange of PSS with less acidic dopants as well as the addition of small molecules. These modifications aim to reach a uniform morphology, increase the interface contact, and produce a neutral pH hole-transporting polymer to improve the stability and cell performance. The use of a layer composed of PEDOT and grafted sulfonated-acetone-formaldehyde lignin (GSL) instead of PSS resulted in a better photovoltaic performance than conventional PEDOT:PSS [259]. GSL is a less acidic copolymer of lignin. A homogeneous surface of the PEDOT:GSL HTL in a PTB7-Th:PC₇₁BM/poly[(9,9bis(3'-(*N,N*-dimethylamino)propyl)-2,7-fluorene)-alt-2,7-(9,9dioctylfluorene)] (PFN)-based OSC resulted in a PCE of 8.47%. PEDOT:PSS treatment with solvents as isopropanol (IPA) also shows a better performance, mainly due to more uniform morphology, increased J_{sc} , and improved cell-light absorption [260]. 2-Methoxyethanol (EGME) and dimethyl sulfoxide (DMSO) solvents were added to a PEDOT:PSS solution [261]. The conductivity after doping was about seven times higher and the OSCs based on P3HT:PCBM improved the PCE from 2.8% to 3.9% owing to increased J_{sc} 16.5 mA cm⁻² and FF of 38.0%. Another approach includes the addition of commercial surfactants such as Zonyl FS-31, which improves the wettability of the interface between the hydrophobic photoactive layer and the PEDOT:PSS HTL [262]. The fluorination of PEDOT:PSS HTL by fluorinated molecules showed an increased device efficiency [263]. On the other hand, a PSS-free, stable PEDOT HTL was obtained by using solid-state polymerization resulting in robust, stable, and solution-processable OSCs based on PCDTBT:PC₇₁BM [264]. Water-soluble polyelectrolyte poly(4-(2,3-dihydrothieno[3,4-b][1,4]dioxin-2-yl-methoxy)-1-butanefulfonic acid) (PEDOT-S), which shows the same PEDOT backbone containing an ethoxyalkylsulfonate branch, showed better performance than conventional PEDOT:PSS layers [265]. PEDOT-sulfonated polyelectrolyte complexes were also tested as an anode buffer layer [266]. Different commercial grades of PEDOT:PSS and additive solvent EG were used to form a hybrid PEDOT:PSS (PH 1000:Al 4083) layer tested as an HTL and anode electrode for inverted OSCs based on P3HT:PCBM [267]. An OSCs based on PTB7-Th:PC₇₁BM was built using a hole-transport double layer made of pyridine-based tetrathiafulvalene derivative (TTF-py) on PEDOT:PSS [268]. This modification resulted in an increased short circuit current (J_{sc}) of 17.19 mA cm⁻² and a PCE of 9.37%. The anode configuration showed a WF of 5.28 eV for the TTF-py layer, resulting in a closer valence band toward the donor material (see Figure 14). PEDOT:PSS/TTF-py had better wettability and enhanced hole mobility, resulting in charge-loss reduction and charge-recombination suppression. Furthermore, TTF-py's molecular structure allowed molecular π - π stacking and formed an orderly molecular arrangement for hole transfer. TTF-py modification also improved the device stability, retaining 96% of the initial PCE after storing for 28 days by the suppression PEDOT:PSS permeation.

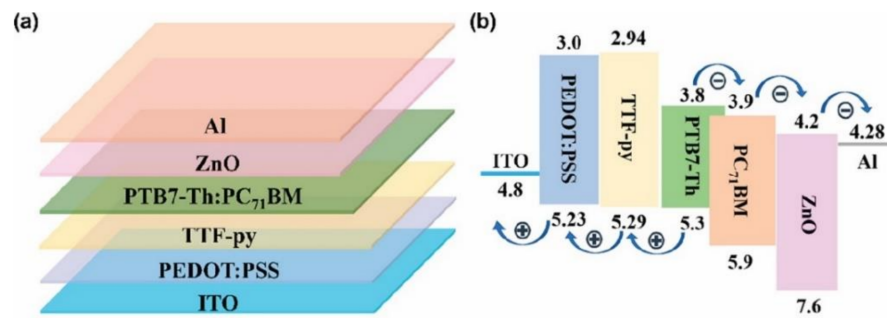


Figure 14. (a) Schematic illustration of device structure of ITO/PEDOT:PSS/TTF-py/PTB7-Th:PC₇₁BM/ZnO/Al and (b) energy level diagram of an OSC with the TTF-py modified PEDOT:PSS as HTL. Adapted with permission from [268]. Copyright 2019, American Chemical Society.

Other modifications on PEDOT:PSS have introduced an inorganic transition metal salt, such as nickel formate dihydrate (NFD), to tune the surface free energy (γ_s) and control the molecular orientation in the BHJ [269]. An enhanced PCE of 10.76% was achieved for the PM6:PC₇₁BM-based OSCs. The NFD:PEDOT:PSS HTL had a WF of 5.01 eV that well-matched the donor material and an increased γ_s of 68.96 mN m⁻¹, which led to increased FF and J_{sc} . Polymeric donor material PM6 preferred a face-on molecular orientation. Enhanced molecular stacking was promoted with an increased γ_s of PEDOT:PSS induced by NFD. This modification improved the molecular orientation along the charge-transport direction; thus, carrier mobility was enhanced, and the charge recombination was suppressed. The modified HTL was also tested in non-fullerene OSCs based on PM6: IT-4F, obtaining an enhanced PCE of 14.08% with FF of 78.75%. Oxoammonium salts (TEMPO⁺ Br⁻, 2,2,6,6-tetramethylpiperidine-1-oxoammonium) were tested as a p-type dopant of PEDOT:PSS layers, resulting in an enhanced PCE of 16.1% in OSCs based on PM6:Y6 [270]. PEDOT:PSS was further oxidized by oxoammonium salt, improving the doping level of PEDOT:PSS. Doped PEDOT:PSS (TEMPO⁺ Br⁻) possess higher conductivity and better energy alignment. Metallo phthalocyanines (PC) such as vapor-deposited vanadylphthalocyanine (VoPC), NiPC, and SnPC were tested as buffer layers with PEDOT:PSS, enhancing the efficiency of P3HT:PCBM-based OSCs [271]. PEDOT:PSS:In₂S₃ was also employed as HTL material for OSCs based on PBDB-T:ITIC and PM6:Y6; these showed an enhanced PCE of 11.22% and 15.89%, respectively [272]. Improved device performance was observed because of increased J_{sc} and FF, and reduced R_s with bimolecular recombination suppression due to partial removal of PSS from the surface. PEDOT also suffered a benzoic-quinoid transition (coil-linear structure) which delocalized charge carriers, enhancing the layer conductivity. Furthermore, device performance stability showed a retained 36% PCE for modified HTLs after 48 h compared with a non-modified PEDOT:PSS HTL, which showed a retained 10% PCE. OSCs based on ITO/PEDOT:PSS-Dopamine (DA)/PM6:Y6/poly[[2,7-bis(2-ethylhexyl)-1,2,3,6,7,8-hexahydro-1,3,6,8-tetraoxobenzo[lmn] [3,8]phenanthroline-4,9-diyl]-2,5-thiophenediyl[9,9-bis[3'((N,N-dimethyl)-N-ethylammonium)]propyl]-9H-fluorene-2,7-diyl]-2,5-thiophenediyl] (PNDIT-F3N)/Ag showed an increased PCE from 16.01% to 16.55% [273]. The DA-doped PEDOT:PSS layer showed an enhanced conductivity ascribed to (i) a more regular stack by the enhanced intermolecular packing of DA:PSS, (ii) an increased WF of 5.14 eV compatible with HOMO level of PM6 donor polymer, and (iii) enhanced film uniformity. PEDOT:PSS-DA was also tested for devices based on different active layers such as PBDB-T:ITIC, PM6: IDIC, and P3HT:PCBM, resulting in improved performances as well. PEDOT:PSS was also used together with various polymers as HTLs, such as nanoimprinted poly(methylmethacrylate) (PMMA) [274], and conjugated polyelectrolytes (CPEs), e.g., poly[(9,9-bis(4-sulfonatobutyl sodium) fluorene-alt-phenylene)-ran-(4,7-di-2-thienyl-2,1,3-benzothiadiazole-alt-phenylene)] (PSFP-DTBTP), that resulted in a PCE improvement of 13% for PCDTBT:PC₇₁BM-based OSCs [275]. Microporous polymer networks are a class of conjugated material that shows high specific surface areas and porosity with potential

application in various fields including organic photovoltaics [276–283]. For instance, a porous organic polymer, poly(carbazolyl triphenylethylene) derivative (PTPCz), obtained by electropolymerization was used in the HTL PEDOT:PSS/PTPCz for OSCs based on PTB7:PC₇₁BM, resulting in a smooth surface morphology, increased WF of 5.23 eV, J_{sc} , and FF, reduced R_s , and increased R_{sh} , reaching an improved PCE of 8.54% [284]. Electropolymerized polytriphenylcarbazole fluoranthene (p-TPCF) and PEDOT:PSS were used for OSCs based on PTB7-Th:PC₇₁BM, obtaining enhanced J_{sc} , FF, V_{oc} , and a PCE of 8.99% [285]. Modification of PEDOT:PSS with a neutral conjugated polymer electrolyte poly[9,9-bis(4'-sulfonatobutyl)fluorene-*alt*-thiophene] (PFT-D) composite layer improved the device performance (PCE from 7.8% to 8.2%) and the half-lives of PTB7-Th:PC₇₁BM-based OSCs [286]. PFT-D molecular dipole screened the attraction between PEDOT and PSS chains; additionally, the $-SO_3^-$ ions of PFT-D act as a conjugate base of PSS, improving current generation. Poly(3-hexylthiophene)-*b*-poly(p-styrenesulfonate) (P3HT₅₀-*b*-PSS₂₃) block polymers were incorporated between HTL PEDOT:PSS and the active-layer P3HT:PCBM [287]. The OSCs with P3HT-*b*-PSS interfacial layer improved PCE by 12% due to increased V_{oc} and FF that compensate for the decreased J_{sc} caused by the blocked light irradiance to the P3HT. The energy level matching was improved. HOMO level of P3HT-*b*-PSS (−4.68 eV) was higher than P3HT of active layer, which facilitates the hole transport. In addition, P3HT-*b*-PSS film had a smoother surface than PEDOT:PSS, enhancing the interfacial contact and thus improving the FF of the device. Modification of the commonly used PEDOT:PSS with metallic NPs contributes with some features such as an enhanced localized field and light scattering by the localized surface-plasmon resonance (LSPR) that improves the absorption of the active layer [288]. NPs also assist in the charge transport at the interface. NPs are synthesized by different methods such as chemical reduction, the polyol method, and ultrasonochemical synthesis [289]. Hao et al. reported mixed AuNPs (rod, bone-like, cube and spheres shape) doped in PEDOT:PSS HTLs in OSCs based on PTB7:PC₇₁BM [290]. The addition of mixed AuNPs generated wide absorption spectra covering from the visible to the near-infrared region and induced an increase of enhancement of internal field in the active layer, resulting in improved absorption and enhanced device performance up to 9.26%. AuNPs also contributed to decrease the bulk resistance of PEDOT:PSS. Periodic Ag nanodot (Ag ND) arrays were fabricated by laser-interference lithography (LIL) between ITO and PEDOT:PSS layers in OSCs based on PTB7:PC₇₀BM (see Figure 15) [291]. This HTL showed increased J_{sc} of 23.26 mA/cm², enhanced EQE induced by the plasmonic and light-scattering effect, and improved PCE of 10.11%. LSPR band matched optimally with the absorption of the photoactive layer, increasing its light-absorption.

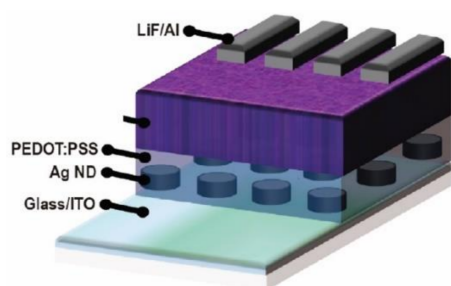


Figure 15. Schematic representation of an OPV device with Ag NDs. Adapted with permission from [291]. Copyright 2016, American Chemical Society.

AuNPs and AgNPs blended with PEDOT:PSS were used as HTLs in OSCs [292]. Both PEDOT:PSS:NPs showed an enhanced device performance in comparison with pristine PEDOT:PSS. An optimized PCE of 5.65% was obtained for PEDOT:PSS:AuNPs HTLs in rrP3HT:PC₇₁BM-based OSCs. Better device performances were obtained with NPs because of the surface-plasmon effect (at the visible region for AuNPs) that increased the photoabsorption length and the trapping of scattering and incident light. Segmented silver nanowires (AgNWs) were incorporated in PEDOT:PSS HTLs in OSCs with configuration

ITO/PEDOT:PSS:AgNWs/P3HT:PC₆₁BM/ZnO/Al [289]. These OSCs exhibited enhanced device performance with a PCE of 3.3%, increased J_{sc} and FF due to LSPR, and optical-scattering properties from the AgNWs. Sah et al. reported the fabrication of OSCs based on PTB7-Th:PC₇₁BM with bimetallic Ag-Au-Ag nanorods (NRs) in PEDOT:PSS HTLs [293]. These devices showed improved performances up to 7.36% owing to an increased FF and J_{sc} . The enhancement was ascribed to an improved charge transport, broad absorption region covering visible to the near-infrared region, light-scattering-induced absorption enhancement, electric field enhancement, and improved EQE by the LSPR effect. Incorporation of copper, a cheaper and more abundant metal, as Cu-Au NPs in PEDOT:PSS for OSC based on P3HT:PC₆₁BM and PTB7-Th:PC₇₁BM showed improved PCEs of 3.63% and 8.48%, respectively [294]. Cu-AuNPs:PEDOT:PSS presented an absorption enhancement by LSPR and light-scattering effect. The improved PCE in the device was attributed to an increased J_{sc} , higher hole mobility, and reduced R_s . However, the FF decreased compared with pristine PEDOT:PSS HTLs, mainly due to an induced charge recombination by the NP doping. Adedeji et al. employed copper sulfide NPs in PEDOT:PSS HTLs to fabricate OSCs based on P3HT:PC₆₁BM [295]. These devices showed an enhanced PCE of 4.51% (an increase of 115% over the pristine PEDOT:PSS HTLs) and good stability, retaining up to 40% of their initial PCEs after 48 h. CuNPs exhibited surface-plasmon resonance absorption near-infrared region and induced an electric field beneficial to exciton dissociation and photon harvesting. The incorporation of nickel sulphide NPs in PEDOT:PSS layers exhibited an enhanced device performance of 6.03% in OSC based on P3HT:PC₆₁BM [288]. An improved photogenerated current was attributed to the effective trapping of light through scattering and improved charge collection. OSCs based on NiS NPs:PEDOT:PSS HTLs showed reduced R_s , indicative of an improved conductivity at the interface, and improved optical transparency enhancing the internal quantum efficiency. Furthermore, the device showed higher hole mobility, and thus reduced carrier recombination and enhanced charge transport. PCE enhancement was ascribed to the LSPR absorption (in the visible and infrared region) and light-scattering process. ZnTe quantum dots (QDs) incorporated into PEDOT:PSS HTL showed an improved device performance in OSC based on P3HT:PC₇₁BM due to improved mobility and enhanced light absorption, attributed to surface-plasmon resonance [296]. Zhang et al. reported OSCs based on PTB7-Th:PC₇₁BM and PM6:IT-4F with high PCEs of 9.11% and 12.81%, respectively, by the insertion of black phosphorous quantum dots (BPQDs) on PEDOT:PSS [297]. BPQDs is a 2D p-type semiconductor, which, inside the device, formed a cascade band structure between the anode and the active layer. The valence band of BPQDs (−4.92 eV) was higher than the valence band of donor polymers PTB7-Th (−5.24 eV) and PM6 (−5.5 eV), providing enough driving force for the hole injection from the active layer to the BPQDs layer. The increased efficiency in devices with BPQDs interfacial layer was attributed to an increased J_{sc} and FF due to excellent hole mobility in BPQDs and better energy alignment in the device, indicating improved charge extraction and exciton dissociation. Other metal NPs incorporated in PEDOT:PSS involve Al micro-stars [298], Al NPs [299], and Au NPs, gold nanorods (Au NRs) [300], and Au QDs [301]. Up-conversion NP process converts low-energy photons into high-energy photons (in the absorption region of organic polymers) to enhance the optical-to-electrical conversion performance [302]. Mei et al. incorporated sodium yttrium fluoride (β -NaYF₄):Er³⁺, Yb³⁺ up-conversion NPs into PEDOT:PSS HTLs in OSCs based on P3HT:PC₆₁BM, resulting in enhanced J_{sc} and PCE of 3.02% [303]. These results were ascribed to light scattering and photoluminescence (PL) emission from up-conversion NPs. Silver-zinc bimetallic NPs were incorporated between the PEDOT:PSS HTL and the photoactive layer of P3HT:PCBM [304]. OSCs exhibited an improved PCE of 3.6%, which was 90% higher than the reference device. This effect was attributed to LSPR of the Ag:Zn NPs, which enhanced the optical absorption and charge-carrier collection. Another modification to PEDOT:PSS was reported by Michalska et al. using wet ultra-sonochemical synthesized titanium dioxide TiO₂ anatase decorated with Ag NPs [305]. TiO₂/Ag solution was added to PEDOT:PSS HTLs showing an improved PCE of 2.07%. Au NPs on PEDOT:PSS in

vacuum-free OSCs improved the device performance resulting from the increased J_{sc} [306]. The absorption of the active layer and the device PCE were enhanced, especially by Au nanorods' presence. Many studies have been focused on improving the performance of PEDOT:PSS HTL by addressing the acidic and hygroscopic nature of PEDOT:PSS that affects the stability and efficiency of the photovoltaic devices. Incorporating metal oxides (MO) can enhance the stability, efficiency, and electron-blocking properties of the HTL. Among these MOs that have been incorporated in PEDOT:PSS are vanadium oxides (V_2O_5), sol-gel synthesized VO_x , continuous-spray pyrolyzed-synthesized molybdenum oxide (MoO_3), and tungsten oxide (WO) [307]. Spin-coated V_2O_5 NWs prepared by the hydrothermal method on PEDOT:PSS HTL (see Figure 16a) showed improved V_{oc} and FF in OSCs based on P3HT:PCBM [308]. The PCE improved a 15.58% in comparison with the pristine PEDOT:PSS reference cell. The LUMO level of V_2O_5 (2.4 eV) is higher than P3HT LUMO, and thus better electron blocking properties than pristine PEDOT:PSS are expected (see Figure 16b). Modified HTL had increased incident light paths by reflection and refraction caused by V_2O_5 NWs.

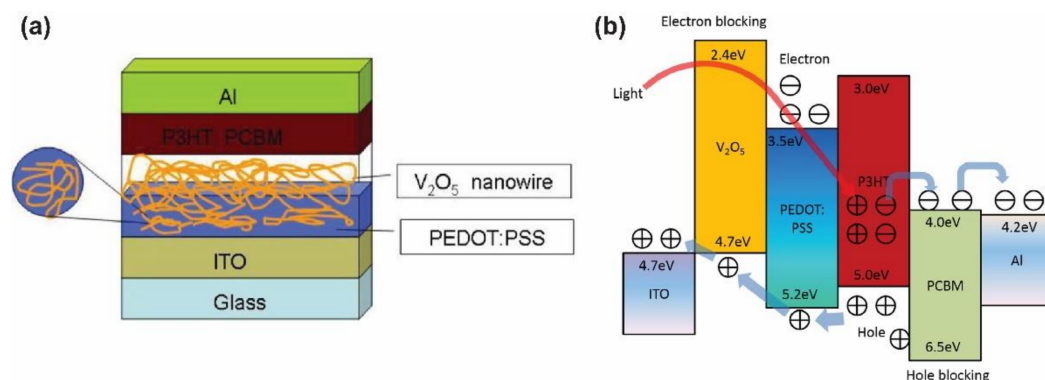


Figure 16. (a) Schematic representation of polymer photovoltaic cell based on PEDOT:PSS/ V_2O_5 HTL and (b) energy level alignment for the cell components. Adapted with permission from [308]. Copyright 2016, Elsevier.

Li et al. reported a PCE of 9.44% for OSCs with V_2O_5 :PEDOT:PSS as HTL due to an enhanced J_{sc} and FF, smaller R_s , and larger R_{sh} [309]. The incorporation of V_2O_5 offered an effective path for exciton extraction and suppressed charge recombination, reflected by a larger hole mobility and a higher conductivity. The composite HTL surface was uniform and smooth, related to V_2O_5 NPs filling the pinholes in PEDOT:PSS. Furthermore, better wetting and physical contact were obtained between the photoactive layer and the HTL as well as enhanced crystallinity of the active layer. Molybdenum oxide (MoO_x) NPs/PEDOT:PSS HTLs were blade coated in inverted OSCs based on PTB7-Th:PC₆₀BM, resulting in an increased FF and enhanced PCE of 7.4% [310]. The modification of PEDOT:PSS with MoO_3 mitigated the degradation of non-fullerene OSCs based on PM6:IT-4F by suppressing the interfacial reaction between PEDOT:PSS and IT-4F [311]. MoO_3 -PEDOT:PSS hybrid HTL improved the device's operational stability, which was five times longer than reference devices. The hybrid HTL also improved the hole mobility favoring the charge extraction. Zinc oxide-doped single-carbon nanotubes (CNT) were incorporated in PEDOT:PSS as an anode buffer layer (ZnO:CNT/PEDOT:PSS), showing excellent transmittance and a smooth morphology [312]. P3HT:PCBM-based OSCs with an HTL containing 2.5% ZnO:CNT showed an improved PCE of 4.1%, enhanced J_{sc} and FF, and reduced R_s . CNT provided surface homogeneity, and ZnO prevented humidity uptake. The device parameters decreased at a slower rate than PEDOT:PSS devices under a nitrogen environment. Zheng et al. fabricated fullerene-free OSCs with tungsten oxide WO_x NPs in PEDOT:PSS as HTL [313]. The system architecture ITO/ WO_x :PEDOT:PSS/PM6:IT-4F/PFN-Br/Al achieved a high FF of 80.79% and enhanced PCE of 14.57%. A more balanced hole and electron mobility was obtained for WO_x :PEDOT:PSS based of BHJ OSCs measured as a ratio μ_e/μ_h

of 0.88, which contributed to increase the FF. The longer lifetime of carriers and faster extract time of WO_x :PEDOT:PSS also benefited the device parameters. WO_3 /PEDOT:PSS bilayer was used as HTL in inverted SMD2: ITIC-Th-based OSCs [314]. An optimized cell achieved a high PCE of 10.3%, with enhanced J_{sc} , V_{oc} , and FF. The WO_3 /PEDOT:PSS device presented increased R_{sh} and decreased R_s by a well-matched energy level alignment, high hole mobility, a more balanced charge-carrier transport, and increased photostability. Furthermore, flexible inverted OSC modules were fabricated by slot-die coating achieving a PCE of 5.25% and a power output of 419.6 mW. A layer of hydrogen molybdenum bronze (H_xMoO_3) with PEDOT:PSS layer was also used in all solution-processed non-fullerene OSCs based on PM6:IDIC:Y6 [315]. Phosphomolybdic acid (PMA) in PEDOT:PSS layers were tested in different organic fullerene-based OSCs, showing good performances [316]. GO, a two-dimensional carbon material, has also been investigated to modified PEDOT:PSS as hole-transport materials in different OSCs. The Oleyamine-functionalized GO/PEDOT:PSS layer on PBDB-T:ITIC [317], PEDOT:PSS treated with GO layers on PTB7:PC₇₁BM devices [318], on P3HT:PC₆₀BM devices [319], on P3HT:PCBM devices [320], on inverted P3HT:PCBM OSCs [321], on inverted P3HT:PC₇₁BM OSCs [322], and on reduced GO-germanium QDs modified PEDOT:PSS on P3HT:PCBM [323]. Raj et al. reported the fabrication of PTB7:PC₇₀BM-based OSCs with PEDOT:PSS:GO, resulting in enhanced PCE of 7.68% [324]. The modified HTL showed a fine fiber-like structure that improved the conductivity. GO showed to increase the device resistance degradation. GO is generally prepared by variations of the Hummers method using graphite powder as the starting material [325,326]. PEDOT:PSS:GO was also tested on P3HT:PC₆₁BM-based OSCs, showing an increased J_{sc} , FF, and a 14% higher PCE than a reference device [327]. GO in the HTL reduced the HOMO-LUMO gap and the R_s , improving the hole mobility and the energy level matching. A double-decked GO/PEDOT:PSS HTL in PCDTBT:PC₇₁BM-based OSCs was reported by Rafique et al. [328]. The modified HTL provided a better hole extraction and transportation by a suitable WF of GO (4.9 eV) and PEDOT:PSS (5.1 eV) that well-matched energy levels. This device showed an improved PCE of 4.28% ascribed to an increased charge-carrier mobility, J_{sc} , V_{oc} , and FF, and a reduced R_s . Besides, better stability than PEDOT:PSS was reached, since GO served as a barrier that protected ITO corrosion due to the acidic nature of PEDOT:PSS (see Figure 17). Similarly, improved photovoltaic stability was achieved with GO/PEDOT:PSS HTLs in P3HT:PC₆₀BM devices [329]. This device showed an increased R_{sh} and a decreased R_s , which facilitate the hole transportation. The composite HTL was smooth and uniform, contributing to an improved device performance with a PCE of 4.82%. Nitrogen-doped graphene quantum dots (nGQDs) were blended with PEDOT:PSS HTLs in PTB7:PC₇₁BM-based OSCs, resulting in an enhanced PCE of 8.5% [330]. The modified HTL improved the charge-carrier transport, increased the hole mobility, and suppressed charge recombination. The nitrogen doping led to a high content of quaternary nitrogen, enhancing the electrical conductivity of GQDs. UV-ozone (UVO)-treated GO/PEDOT:PSS bilayer in OSCs based on PCDTBT:PC₇₁BM presented an improved PCE of 5.24% [331]. An increased J_{sc} , V_{oc} , and FF were obtained in the cells using the modified HTL and improved ambient stability, retaining above 90% of initial PCE after 240 h. The enhanced conductivity was ascribed to the reduction of oxygen content in GO after UVO treatment.

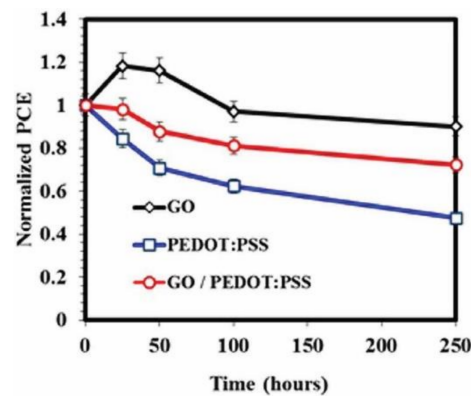


Figure 17. Stability test of various OSCs over 250 h. Adapted with permission from [328].

Other modifications on PEDOT:PSS have also been reported with a graphene analog, the two-dimensional transition metal dichalcogenides. For instance, hybrid PEDOT:PSS/ WS_2 was incorporated as HTL in OSCs [332]. PEDOT:PSS worked as an effective exfoliating agent to the WS_2 2D structure. The photovoltaic device based on P3HT:PC₆₁BM and PTB7-Th:PC₇₁BM exhibited enhanced PCE of 3.07% and 7.24%, respectively, attributed to increased J_{sc} and FF as well as to enhanced hole mobility and enhanced conductivity of the PEDOT:PSS/ WS_2 layer. Besides, PEDOT:PSS/ WS_2 -based OSCs had improved stability, retaining 77.3% of initial PCE after 36 days. Koo et al. fabricated PTB7:PC₇₁BM-based OSCs with tungsten diselenide (WSe_2)/PEDOT:PSS HTLs (see Figure 18a), showing an enhanced PCE of 8.5% [333]. The composite HTL exhibited a homogeneous film formation. WSe_2 negative surface induced the segregation of PEDOT and PSS, which enhanced the layer conductivity. Furthermore, photoluminescence peak intensity decreased, indicating diminished recombination (see Figure 18b). Thus, PEDOT:PSS- WSe_2 showed improved hole-transport ability and a better charge extraction than the reference device. Oleyamine-functionalized molybdenum disulfide MoS_2 has also been reported in the modification of PEDOT:PSS HTLs [334].

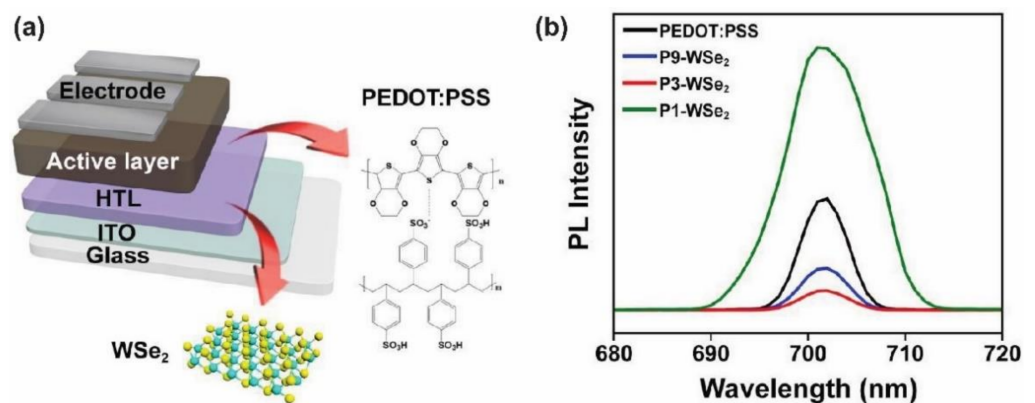


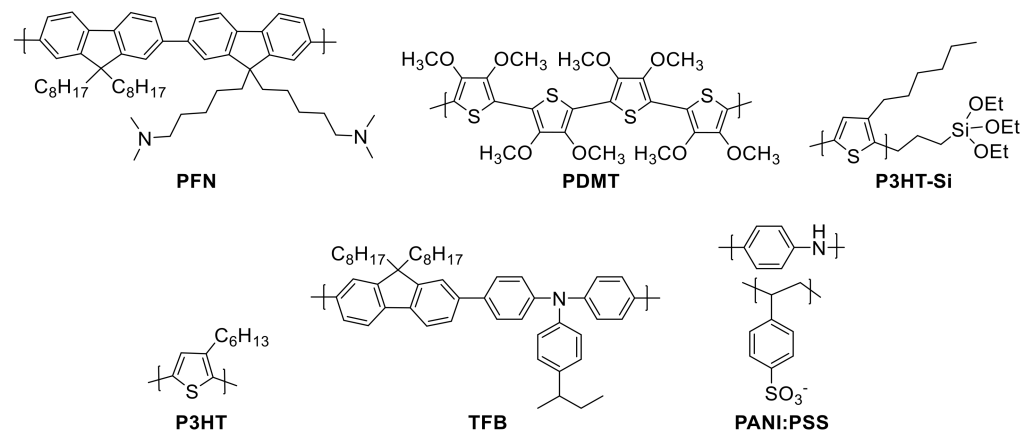
Figure 18. (a) Schematic representation of a WSe_2 -PEDOT:PSS HTL-based OSC and (b) PL spectra measured from structure of glass/PEDOT:PSS and P- WSe_2 -based devices. Adapted with permission from [333]. Copyright 2018, IOP Publishing Ltd.

Boronic acid functionalized multi-walled CNs (bf-MWCNTs)-doped PEDOT:PSS HTLs showed excellent hole mobility and electrical conductivity [335]. The OSC with PEDOT:PSS:bf-MWCNTs showed reduced R_s and increased R_{sh} , exhibiting excellent hole collectivity. A 28% increased PCE for PCDTBT:PC₇₁BM based OSC was attributed to an enhanced J_{sc} and FF. PL intensity of HTL doped with bf-MWCNTs was reduced, indicating an enhancement in charge transport from the active layer. The WF increased to 5.39 eV that well-matched with the HOMO energy level of PCDTBT. Graphitic carbon nitrile ($g-C_3N_4$) was used as a secondary dopant for PEDOT:PSS in OSCs based on PM6:Y6, leading to

an improved PCE of 16.38% [336]. The g-C₃N₄:PEDOT:PSS HTL showed a higher conductivity, an improved charge transport, and a suppressed charge recombination. This modified HTL had increased hole mobility, leading to more balanced charge transport. The g-C₃N₄ insulated the PSS moiety, so the conducting PEDOT chain was exposed. A two-dimensional titanium carbide (Ti₃C₂T_x) bilayer was incorporated into PEDOT:PSS HTLs in non-fullerene PBDB-T:ITIC and PM6:Y6 OSCs [337]. This bilayer enhanced the conductivity of PEDOT:PSS by a reduced coulombic attraction between PEDOT and PSS, causing the conformational transition of PEDOT from coil to linear structures. The HTL roughness increased upon Ti₃C₂T_x incorporation, which enlarged the contact area between HTL and the photoactive layer. The hole mobility increased because of the interconnected conducting network between PEDOT and Ti₃C₂T_x. The PL peak was reduced, indicating improved hole transmission. As a consequence, the PCE of devices improved to 11.02% and 14.55% for PBDB-T:ITIC- and PM6:Y6-based OSCs, respectively. Moreover, PEDOT:PSS/Ti₃C₂T_x HTLs enhanced the nitrogen atmosphere's long-term stability, retaining 79.67% of the initial PCE after 300 h.

4.4.2. Other Conjugated Polymers

Another approach aims to replace the use of PEDOT:PSS with different conjugated polymers. The chemical structure of a series of conjugated polymers used as HTL for OSCs are shown in Scheme 1.

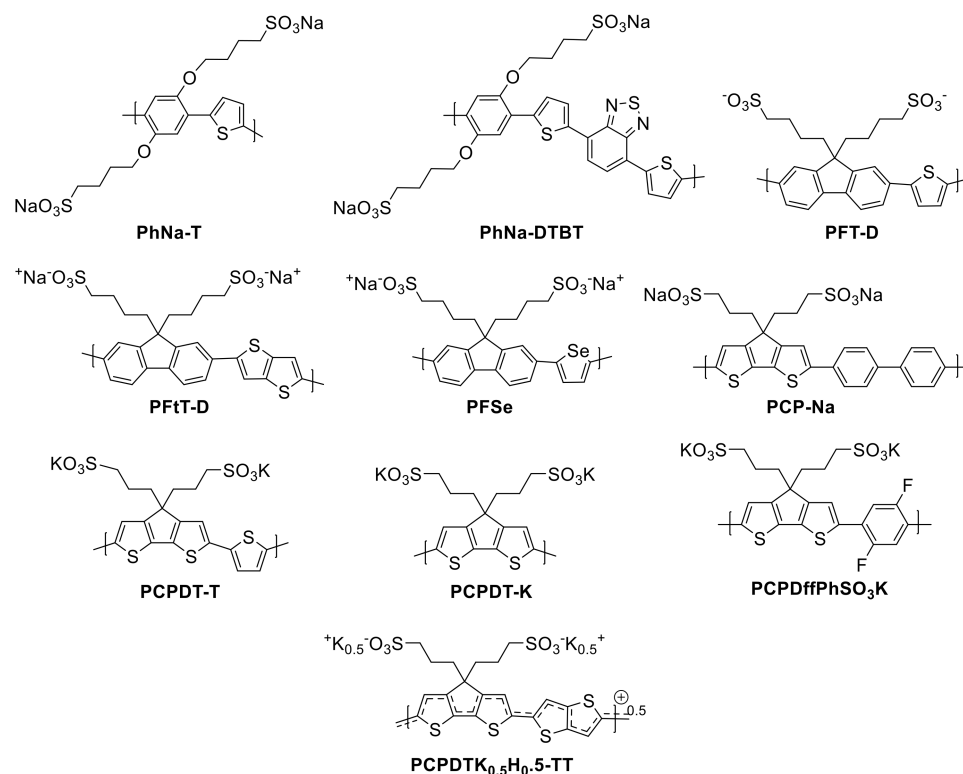


Scheme 1. Chemical structure of some conjugated polymers used as HTLs.

A HTL nanocomposite based on fluorene derivatives, poly[(9,9-bis(3'-(*N,N*-dimethylamino)propyl)-2,7-fluorene)-alt-2,7-(9,9-dioctyl)fluorene] and nickel oxide (PFN/NiO_x), showed a PCE of 6.2% in PBDTTBO-C₈:PC₇₁BM-based OSCs [338]. The device performance improvement was related to the interaction between PFN and NiO_x, p-doping effect in NiO_x, and good energy alignment. A blend of 5,6-difluorobenzothiadiazole conjugated polymer and metal oxide (Cu₂O/FBT-TH4) produced a PCE of 9.56% for OSCs based on PffBT4T-2OD:PC₇₁BM [339]. Better charge transfer properties and stability were determined, maintaining 75% of the original PCE for up to 30 days. This result was attributed to the hydrophobic character of the HTL. Poly(3,4-dimethoxythiophene) (PDMT) deposited via oxidative chemical vapor deposition were also used as hole-transport materials in OSCs [340]. Awada et al. fabricated OSCs based on hydrophobic triethoxysilane-terminated poly(3-hexylthiophene) (P3HT-Si) HTLs exhibiting a slightly enhanced device stability [341]. Some other polymers and composites used as hole-transport layers include P3HT:SWCNTs [342] and polyaniline/gold and silver NPs composites (Au₁₀Ag₁₀PANI) [343]. The interconnected network of grafted CNTs, polythiophenic agents, and conjugated PANI bottlebrushes (CNT-g-PDDT:P3ThEt-g-PANI) were used as HTL in OSCs based on PBDT-DTNT:PC₆₁BM, showing smooth morphology, low sheet resistance, and a PCE of 5.65% [344]. A network of CNTs and polythiophene/polyaniline bottlebrushes (CNT:P3ThEt-g-PANI) was tested as HTL in OSCs based on P3HT:PC₇₁BM, reaching an improved PCE of

5.30% [345]. Another approach involves the use of low acidic water-stable PSS-doped PANI as HTL based on P3HT:ICBA OSCs [346]. The PANI:PSS layer presented a well-matched WF, high conductivity, and transmittance around 90% that resulted in OSCs with PCE of 4.5%. Additionally, PANI:PSS HTL has also been tested for indoor photovoltaics [347,348]. The OSCs based on P3HT:ICBA showed a lower PCE than a device using PEDOT:PSS, but possessed better stability over 1176 h, retaining 39% of its initial PCE. PANI was also tested with GO as an acid-free composite HTL in OSCs based on P3HT:PCBM and PCDTBT:PC₇₁BM, resulting in optimized performance for the nanocomposite with a GO loading of 7.3 wt% [349]. A hole-transporting bilayer of copper(I) thiocyanate and poly[(9,9-dioctylfluorenyl-2,7-diyl)-alt-(4,4'-(N-(4-butylphenyl)))] (CuSCN/TFB) was tested in OSCs based on non-fullerene PM6:Y6 and fullerene PTB7-Th:PC₇₁BM by Dong et al. [350]. Better photovoltaic performance with the CuSCN/TFB bilayer than with pristine CuSCN HTL was related to enhanced J_{sc} and FF. The decreased roughness and increased contact angle of the bilayer favored the interfacial contact of the HTL and the active layer, leading to better energy matching and device performance (up to 15.10%). Furthermore, the CuSCN/TFB-based device presented improved hole mobility, higher exciton dissociation efficiency, and lower recombination loss, which contributed to its enhanced exciton dissociation and charge transportation and extraction.

CPEs composed of conjugated backbone and side chains containing ionic groups are attractive materials due to their intrinsic dual electronic and ionic conductivity, and good solubility in polar solvents [351–356]. Some examples of the chemical structure of CPEs used as HTLs are shown in Scheme 2.



Scheme 2. Chemical structure of some CPEs used as HTLs.

Poly[1,4-bis(4-sulfonatobutoxy)benzene-thiophene] (PhNa-1T) self-doped in a neutral state achieved an increased WF of 5.21 eV, resulting in PCEs of 9.89% and 8.38% for ITO/PhNa-1T/PTB7-Th:PC₇₁BM/fullerene derivative (bis-C₆₀)/Ag and ITO/PhNa-1T/PTB7:PC₇₁BM/TiO₂/Al cells, respectively [357]. The enhanced device performance was ascribed to improved interfacial properties, a high WF, and a smoother surface resulting in a favorable contact, improved charge extraction, and an efficient hole collection. PhNa-DTBT CPE, which is based on a weakly electron-donating 2-phenyl thiophene,

an electron-acceptor, 2,1,3-benzothiadiazole, and sulfonate sodium salt as an ionic functional group were used in PTB7-Th:PC71BM OSCs, reaching a PCE of 9.29% [358]. PhNa-DTBT showed a high electrical conductivity, improved J_{sc} and FF, and high WF (5.39 eV). The device also showed improved stability with a retained PCE of ca. 40% after 96 h. A pH-neutral self-doped polymer based on phenyl and thienyl units, poly[2,6-(4,4-bis-(propane-1-sulfonate sodium)-4*H*-cyclopenta[2,1-*b*;3,4-*b'*]dithiophene)-alt-(4,4'-biphenyl)] (PCP-Na), was used as HTL for PBDT-TS1:PC71BM-based OSCs [359]. PCP-Na had a suitable HOMO level, smooth surface, and a high electrical conductivity due to the presence of polaronic states (radical cations). PCP-Na exhibited appreciable hole collection and charge-transport properties. The photovoltaic device using PCP-Na showed a PCE of 9.89% that resulted mainly from an enhanced FF. Following the same line, pH neutral poly[9,9-bis(4'-sulfonatobutyl)fluorene-alt-selenophene] (PFSe) was used as HTL in OSCs with architecture ITO/PFSe/PTB7:PC71BM/PFN/Al, exhibiting a PCE of 7.2% [360]. The increased J_{sc} and FF were ascribed to a strong dipole moment at the interface. A WF of 5.15 eV of PFSe assured a good ohmic contact and a better matching energy level. Moreover, the air stability of the cell was improved by the neutral nature of the HTL polymer. Xu et al. reported a pH-neutral CPE, 3,4-dithia-7*H*-cyclopenta[*a*]pentalene and thienyl units (PCPDT) used in OSCs based on PTB7-Th:PC71BM with a PCE of 9.3% [361]. Improved device performance by using PCPDT HTL was attributed mainly to a reduced leakage current and R_s . A tuned WF of -4.87 eV, enhanced transmittance, and improved and homogeneous mobility of HTL were related to the strong p-type self-doped nature of this HTL. Moreover, the hole layer showed improved interface compatibility, evidenced by the reduced surface energy (30.7 mN m⁻¹). The use of PCPDT-K HTL in OSC based on P3HT:PCBM showed improved device performance, increased J_{sc} , reduced R_s , a smooth surface, and better stability than a PEDOT:PSS reference device [362]. PCPDffPhSO₃K, a neutral CPE based on 3,4-dithia-7*H*-cyclopenta[*a*]pentalene and 1,4-difluorobenzene units, was used as HTL for ITO/HTL/PTB7-Th:PC71BM/PFN/Al OSCs, resulting in PCE of 9.5% [363]. The self-doping effect in PCPDffPhSO₃K improved its conductivity. A WF around -5.18 eV ensured a better energy level alignment, achieving a higher V_{oc} , J_{sc} , and hole mobility. Lee et al. utilized poly[9,9-bis(4'-sulfonatobutyl)fluorene-alt-thieno[3,2-*b*]thiophene] (PFfT-D) HTLs showing a PCE of 8.3% for OSCs based on PTB7-Th:PC71BM [364]. The WF of the modified electrode with PFfT-D was 5.19 eV, which resulted in superior ohmic contact due to well-matched energy levels facilitating the hole transportation. The modification of WF was attributed to the molecular dipole orientations. The device showed an improved lifetime because of the neutral nature of CPE; the PCE slowly decreased with a half-life of 153 h. PCPDTK_{0.50}H_{0.50}-TT, a neutral self-doped CPE, was used as HTL for the OSCs based on PM6:Y6:PC71BM [365]. Potassium ions were exchanged to protons through ion-exchange chromatography using acid-sulfonated polystyrene resin. PCPDTK_{0.50}H_{0.50}-TT HTL had a higher WF and increased mobility, and it also exhibited a higher hole-extraction efficiency. The device performance with this HTL was improved with a PCE of 16.3%. The V_{oc} increased due to the improved hole mobility, and the J_{sc} and FF were also improved, ascribed to reduced carrier recombination and reduced bulk resistance. The device showed improved stability, and the PCE was retained by a longer time than PEDOT:PSS-based reference cells. OSCs with an area of 1.0 cm² prepared by wire-bar coating achieved a PCE greater than 10%, showing potential for large-area printing techniques (see Figure 19).

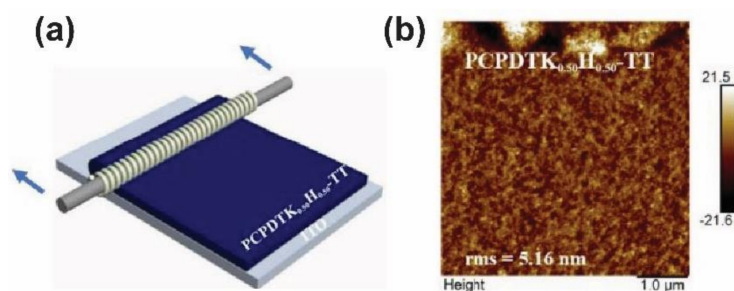
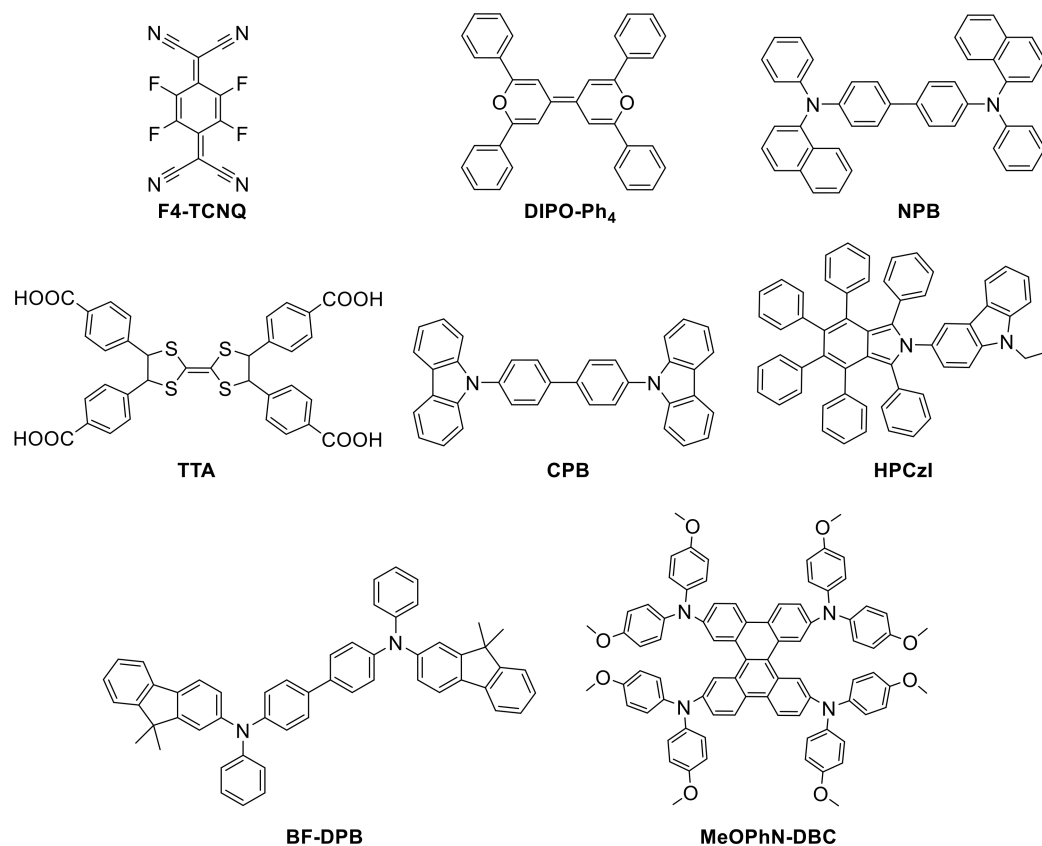


Figure 19. (a) Wire-bar coating process and (b) AFM image of the PCPDTK0.50H0.50-TT film prepared by the wire-bar coating process. Adapted with permission from [365]. Copyright 2021, American Chemical Society.

4.5. Small Organic Molecules

As an alternative to conjugated polymers, small organic molecules can be used as HTLs for photovoltaic applications [36]. Polymeric materials shown in the previous section have several drawbacks e.g., complicated synthesis, costly purification processes, and precise control of their molecular weight. In general, polymeric HTL materials used in OSCs usually have molar mass over $10,000 \text{ g mol}^{-1}$, which makes them expensive [366]. Moreover, the hole mobilities of polymers such as PTAA are sensitive to molecular weights, polydispersity indices, and purities [367]. HTLs based on small organic molecules, compared with inorganic and polymeric materials, present a variety of benefits such as simple synthesis, structural versatility, high purity, and tunable energy levels [368]. Some examples of the molecular structure of small molecules used as HTL are shown in Scheme 3.



Scheme 3. Chemical structure of some small organic molecules used as HTLs.

NDP9 doped *N,N'*-((diphenyl-*N,N'*-bis(9,9-dimethyl-fluoren-2-yl)-benzidine (BF-DPB) was used as a hole-transport material in OSCs based on zinc phthalocyanine (ZnPC):fullerene

C₆₀ [369]. Spin-coated BF-DPB HTLs over AgNWs electrodes exhibited a PCE of 4.4%. BF-DPB smoothed the AgNWs topography. Cheng et al. fabricated NiOx/2,3,5,6-tetrafluoro-7,7,8,8-tetracyanoquinodimethane (F4-TCNQ) composite HTLs for the fabrication of OSCs without pre-treatment of ITO nor post-treatment on the HTL [370]. The device performance of one-step ethanol-processed NiOx:F4-TCNQ in P3HT:PC₆₁BM-based OSCs was 15.8% better than one-step PEDOT:PSS-based OSCs. NiOx:F4-TCNQ HTL was also used on PTB7-Th:PC₇₁BM-based OSCs, resulting in an enhanced PCE of 8.59%. A planar quinoid molecule, 2,2',6,6'-tetraphenyl-dipyranilidene (DIPO-Ph₄), was tested as an anodic interfacial layer with PEDOT:PSS in P3HT:PCBM OSCs [371]. Vacuum-deposited DIPO-Ph₄ (10 nm thickness) on spin-coated PEDOT:PSS (5 nm thickness) increased OSCs' current and enhanced efficiency to 4.6%. DIPO-Ph₄'s needle-like morphology increased the contact area between the active layer and the anode with high hole conductivity. 1,3,4,5,6,7-Hexaphenyl-2-(3'-(9-ethylcarbazolyl))-isoindole (HPCzI) HTLs exhibited improved performance in comparison with MoO₃-based OSCs, reaching a PCE of 1.69% for CuPC:C60-based OSCs, due to larger FF and J_{sc} [372]. *N,N'*-bis(1-naphthalenyl)*N,N'*-bis-phenyl-(1,1'-biphenyl)-4,4'-diamine (NPB) was incorporated as HTL on inverted P3HT:PC₇₁BM OSCs, resulting in a PCE of 2.63%, a J_{sc} of 9.49 mA cm⁻², and low R_s [373]. These results suggested the formation of an ohmic contact between the photoactive layer and anode, which contributed to the hole extraction efficiency. Alternatively, the NPB layer was inserted between the MoO₃ layer and the photoactive layer in inverted OSCs based on P3HT:PC₆₁BM [374]. The PCE was enhanced from 3.20% to 3.94%, owing to the increased J_{sc} and reduced R_s by an improved charge transportation and reduced recombination at the interface. MoO₃ p-doped 4,4'-*N,N'*-dicarbazole-biphenyl (CBP:MoO₃) was also utilized as HTLs in inverted P3HT:PC₆₁BM-based OSCs [375]. A 3,6,11,14-Tetramethoxyphenylamine-dibenzo[g,p]chrysene (MeOPhN-DBC) layer was incorporated between MoO₃ and active-layer P3HT:PC₆₁BM-inverted OSCs, showing an enhanced PCE of 3.68%, attributed to improved J_{sc} and FF, and reduced leakage current [376]. Liu et al. reported a tetrathiafulvalene derivative with four carboxyl groups (TTA) as an HTL in OSCs (see Figure 20a) [377]. This HTL displayed a well-matched energy level (see Figure 20b) and an enhanced PCE of 9.09% in comparison with a PEDOT:PSS-based OSC (see Figure 20c). The improved FF and J_{sc} were related to the smooth surface of the TTA layer, improved charge transfer and hole mobility, and reduced charge recombination.

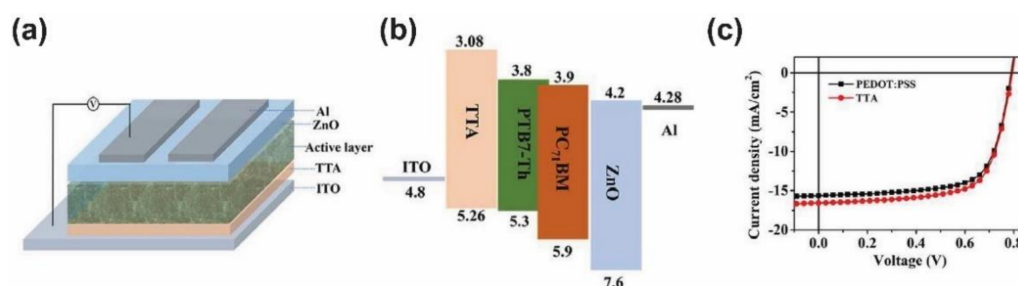


Figure 20. (a) Illustration of OSCs structure based on TTA, (b) energy level diagram of different layers, and (c) J-V curves of devices with TTA and PEDOT:PSS as HTLs. Adapted with permission from [377]. Copyright 2020, Elsevier.

Large-scale printing processes, like roll-to roll, require that the prepared small molecules present good adhesion and compatibility between the anode and the active layer, high carrier transport, good stability, and high solubility in non-pollutant solvents. Flexible devices will additionally require having mechanical flexibility of the layer. Convenient modification of certain functional groups allows the tuning of the electronic properties of the material to match the work function and conductivity. The research activity in these fields is very active, representing the main challenges to pave the road towards the wide commercialization of the OSCs [78].

Finally, Table 2 enlists a series of HTLs based on organic conjugated polymers and small molecules. The anode configuration with its work function, deposition technique for the HTL, active layer composition, and the OSCs performance parameters are provided as well as the reference where the information was taken from.

Table 2. Performance parameters of some representative OSCs with different organic conjugated polymers and small molecules as HTLs.

Anode Configuration and WF (eV)	Deposition Technique	Active Layer	VOC (V)	JSC (mA cm ⁻²)	FF (%)	PCE (%)	Ref.
<i>PEDOT:PSS</i>							
ITO/PEDOT:PSS-DA (5.14)	spin coating	PM6:Y6	0.84	25.52	77.1	16.55	[273]
ITO/g-C ₃ N ₄ :PEDOT:PSS (4.89)	spin coating	PM6:Y6	0.84	26.71	73.0	16.38	[336]
ITO/PEDOT:PSS:TEMPO ⁺ Br ⁻ (4.95)	spin coating	PM6:Y6	0.82	27.18	72.6	16.10	[270]
ITO/PEDOT:PSS:a-In ₂ Se ₃ (5.06)	spin coating	PM6:Y6	0.84	25.47	74.5	15.89	[272]
ITO/WO _x :PEDOT:PSS (4.7)	spin coating	PM6:IT-4F	0.87	20.73	80.8	14.57	[313]
ITO/PEDOT:PSS/Ti ₃ C ₂ T _x (5.0)	selectively etching/spin coating	PM6:Y6	0.83	25.63	68.4	14.55	[337]
ITO/PEDOT:PSS-MoO ₃ (5.22)	spin coating	PBDB-T-2F:IT-4F	0.86	21.71	70.6	13.19	[311]
ITO/PEDOT:PSS/BPQD (4.92)	spin coating	PM6:IT-4F	0.85	21.14	71.3	12.81	[297]
AgNWs/PEDOT:PSS/H _x MoO ₃ (5.44)	transfer printing	PM6:IDIC:Y6	0.83	21.00	68.0	11.90	[315]
ITO/PEDOT:PSS:a-In ₂ Se ₃ (5.06)	spin coating	PBDB-T:ITIC	0.91	17.31	71.1	11.22	[272]
ITO/PEDOT:PSS/Ti ₃ C ₂ T _x (5.0)	selectively etching/spin coating	PBDB-T:ITIC	0.91	17.08	70.9	11.02	[337]
ITO/NiFD:PEDOT:PSS (5.01)	spin coating	PM6:PC ₇₁ BM	0.98	13.82	79.4	10.76	[269]
WO ₃ /PEDOT:PSS/Ag (5.27)	spin coating	SMD2:ITIC-Th	0.90	17.30	66.0	10.30	[314]
ITO/Ag ND/PEDOT:PSS	LIL/spin coating	PTB7:PC ₇₀ BM	0.73	23.26	61.0	10.11	[291]
ITO/PEDOT:PSS-AuNRs	spin coating	PTB7-Th:PC ₇₁ BM-Au NRs	0.80	17.90	68.8	9.89	[300]
ITO/V ₂ O ₅ : PEDOT:PSS	spin coating	PTB7-Th:PC ₇₁ BM	0.80	16.83	70.1	9.44	[309]
ITO/PEDOT:PSS/TTF-py (5.29)	spin coating	PTB7-Th:PC ₇₁ BM	0.79	17.19	70.6	9.37	[268]
ITO/PEDOT:PSS + Au NPs (5.4)	spin coating	PTB7:PC ₇₁ BM	0.74	18.30	68.0	9.26	[290]
ITO/PEDOT:PSS/BPQD (4.92)	spin coating	PTB7-Th:PC ₇₁ BM	0.80	16.40	69.4	9.11	[297]
ITO/PEDOT:PSS/p-TPCF (5.28)	electrochemical cyclic voltammetry	PTB7-Th:PC ₇₁ BM	0.80	16.98	66.2	8.99	[285]
ITO/GO _s /PEDOT:PSS (4.55)	spin coating	PBDB-T:ITIC	0.90	15.10	65.7	8.93	[317]
PMA:PEDOT:PSS/Al (5.02)	spin coating	PTB7-Th:PC ₇₁ BM	0.79	17.10	68.0	8.88	[316]
PMA:PEDOT:PSS/Al (5.02)	spin coating	PffBT4T-2OD:PC ₇₁ BM	0.77	18.44	64.0	8.75	[316]
ITO/PEDOT:PSS/PTPCz (5.23)	spin coating/electrodeposition	PTB7:PC ₇₁ BM	0.74	16.23	71.1	8.54	[284]
ITO/PEDOT:PSS-WSe ₂	spin coating	PTB7:PC ₇₁ BM	0.78	16.60	65.5	8.50	[333]
ITO/PEDOT:PSS-Cu-Au NPs	spin coating	PTB7-Th:PC ₇₁ BM	0.79	17.78	60.1	8.48	[294]
ITO/PEDOT:GSL (5.05)	spin coating	PTB7-Th:PC ₇₁ BM	0.77	15.82	68.7	8.47	[259]
ITO/GO/PEDOT:PSS (4.9)	chemical vapor deposition/drop casting	PTB7:PC ₇₁ BM	0.75	16.10	69.5	8.40	[318]
ITO/PEDOT:PSS:FOS (4.90)	spin coating	PTB7:PC ₇₀ BM	0.70	16.94	69.3	8.26	[263]
ITO/PEDOT:PSS+PFT-D (5.0)	spin coating	PTB7-Th:PC ₇₁ BM	0.77	14.90	71.3	8.20	[286]
FTO/PMMA/PEDOT:PSS	nanoimprinting/spin coating	PTB7:PC ₇₀ BM	0.73	16.30	68.2	8.12	[274]
ITO/PSS:PEDOT:PSS (4.80)	spin coating	PDCBT:PC ₇₁ BM	0.83	12.44	77.2	7.97	[269]
ITO/PEDOT:PSS:GO (5.1)	spin coating	PTB7:PCBM	0.75	14.90	67.5	7.68	[324]
PEDOT:PSS+MoO ₃ NPs/Ag (5.0)	spin coating/blade coated	PTB7-Th:PC ₆₀ BM	0.78	14.99	63.0	7.39	[310]
ITO/PEDOT:PSS:Ag-Au-Au NRs	spin coating	PTB7:PC ₇₁ BM	0.73	16.87	60.0	7.36	[293]
ITO/PEDOT:PSS/WS ₂	spin coating	PTB7-Th:PC ₇₁ BM	0.79	15.67	58.6	7.24	[332]
ITO/PEDOT:PSS:Cu-Au NPs	spin coating	PTB7-Th:PC ₆₁ BM	0.80	15.50	57.9	7.13	[294]
ITO/PEDOT:PSS:bf-MWCNTs (5.39)	spin coating	PCDTBT:PC ₇₁ BM	0.88	12.51	63.1	6.95	[335]
ITO/PEDOT-S (5.2)	spin coating	P3TI:PC ₇₁ BM	0.73	12.80	72.0	6.70	[265]
ITO/PEDOT:PSS-NiS	spin coating	P3HT:PC ₆₁ BM	0.58	18.65	55.9	6.03	[288]
ITO/PEDOT:PSS + Au NPs (5.0)	spin coating	rrP3HT:PC ₇₁ BM	0.58	16.10	61.0	5.65	[292]
ITO/PEDOT:PSS + Au NPs (5.0)	spin coating	rrP3HT:PC ₇₁ BM	0.58	14.70	61.0	5.29	[292]
ITO/PEDOT:PSS:PSFP-DTBTP (5.14)	spin coating	PCDTBT:PC ₇₁ BM	0.88	9.46	66.3	5.26	[275]
ITO/GO/PEDOT:PSS (4.9)	spin coating	PCDTBT:PC ₇₁ BM	0.85	10.82	57.0	5.24	[331]
ITO/PEDOT:PSS:GO (5.52)	spin casting	PTB7:PC ₇₁ BM	0.65	15.17	53.0	5.22	[327]
ITO/PEDOT:PSS-MoO ₃ (5.3)	spray deposition	PTB7:PC ₇₁ BM	0.69	15.20	48.3	5.11	[307]
PMA:PEDOT:PSS/Ag NWs (5.02)	doctor-blade coating	PTB7-Th:PC ₇₁ BM	0.78	11.28	57.0	5.01	[316]

Table 2. Cont.

Anode Configuration and WF (eV)	Deposition Technique	Active Layer	VOC (V)	JSC (mA cm ⁻²)	FF (%)	PCE (%)	Ref.
<i>Other conjugated polymers</i>							
ITO/PCPDKH-TT (5.24)	wire-bar coating	PM6:Y6:PC ₇₁ BM	0.85	25.10	75.9	16.30	[365]
ITO/CuSCN/TFB (5.32)	spin coating	PM6:Y6	0.85	24.45	72.7	15.10	[350]
ITO/PhNa-1T (5.21)	spin coating	PTB7-Th:PC ₇₁ BM	0.79	16.98	71.1	9.89	[357]
ITO/PCP-Na (5.22)	spin coating	PBDT-TS1:PC ₇₁ BM	0.80	17.46	70.6	9.89	[359]
ITO/Cu ₂ O/FBT-TH4 (5.08)	sputtered method	PffBT4T-2OD:PC ₇₁ BM	0.77	17.50	70.7	9.56	[339]
ITO/PCPDffPhSO3K (5.18)	spin coating	PTB7-Th:PC ₇₁ BM	0.79	18.08	67.0	9.50	[363]
ITO/PCPDT-T (4.87)	spin casting	PTB7-Th:PC ₇₁ BM	0.77	18.92	63.5	9.30	[361]
ITO/PhNa-DTBT (5.3)	spin coating	PTB7-Th:PC ₇₁ BM	0.79	16.92	69.5	9.29	[358]
ITO/CuSCN/TFB (5.32)	spin coating	PTB7-Th:PC ₇₁ BM	0.79	16.42	66.3	8.56	[350]
ITO/PhNa-1T (5.21)	spin coating	PTB7:PC ₇₁ BM	0.75	16.17	68.6	8.38	[357]
ITO/PfT-D (5.19)	spin coated	PTB7-Th:PC ₇₁ BM	0.76	16.00	68.4	8.30	[364]
ITO/PFSe (5.1)	spin casting	PTB7:PC ₇₁ BM	0.68	14.40	69.0	7.20	[360]
ITO/NiO _x :PFN (5.34)	spin casting	PBDTTBO-C8:PC ₇₁ BM	0.71	13.75	63.7	6.20	[338]
ITO/CNT-g-PDDT:P3ThEt-g-PANI	spin coating	PBDT-DTNT:PC ₆₁ BM	0.71	12.84	62.0	5.65	[344]
ITO/CNt:P3ThEt-g-PANI	spin coating	P3HT:PC ₇₁ BM	0.68	12.85	60.7	5.30	[345]
<i>Small organic molecules</i>							
ITO/TTA (5.26)	spin coating	PTB7-Th:PC ₇₁ BM	0.80	16.56	69.04	9.09	[377]
ITO/NiO _x :F ₄ -TCNQ (5.30)	spin coating	PTB7-Th:PC ₇₁ BM	0.78	16.80	65.20	8.59	[370]
ITO/DIPO-Ph ₄ /PEDOT:PSS (4.7)	vacuum deposition/spin coating	P3HT:PC ₆₁ BM/	0.60	11.50	47.00	4.60	[371]
NPB/MoO ₃ /Ag (5.4)	thermal evaporation	P3HT:PC ₆₁ BM	0.60	10.04	63.00	3.94	[374]
MeOPhN-DBC/MoO ₃ /Al (5.0)	vacuum deposition	P3HT:PC ₆₁ BM	0.63	12.44	47.00	3.68	[376]
ITO/NiO _x :F ₄ -TCNQ (5.30)	spin coating	P3HT:PC ₆₁ BM	0.59	9.89	61.60	3.59	[370]
NPB/Ag (5.4)	vacuum deposition	P3HT:PC ₇₁ BM	0.57	9.49	48.90	2.63	[373]
ITO/BF-DPB:NDP9 (5.23)	spin coating	ZnPC:C60	0.51	7.50	55.00	2.10	[369]
Ag NWs/BF-DPB:NDP9 (5.23)	spin coating	ZnPC:C60	0.49	7.60	55.00	2.10	[369]
ITO/MoO ₃ :HPCzI (5.3/5.1)	thermal evaporation	CuPC:C60	0.49	6.63	53.00	1.71	[372]
ITO/HPCzI (5.1)	thermal evaporation	CuPC:C60	0.49	6.22	53.00	1.62	[372]

5. Conclusions

In summary, HTLs are fundamental to assure the high performance and stability of OSCs. Inorganic and nanocarbon materials including MoO₃, WO₃, V₂O₅, NiO_x, CuO_x, CoO_x, CuCrO_x, CuSCN, MoS₂, WS₂, NiS, CuS and GO, QCDs, and CNTs have shown great potential as HTLs in conventional and inverted OSCs. These hole-extracting materials can form an ohmic contact between the active and electrodes depending on their optical and electrical properties. Their high transparency enables them to absorb high light into the active layer to afford the hole-electron pairs generation, and the tuning of the Fermi levels with the donor allows the hole collection. Usually, the hole transport takes place in the HTL valence band, but in *n*-type metals such as MoO₃, it has been found that the conduction band facilitates the hole transport. Thus, the type of hole-transport path will vary with the WF and energy levels of the inorganic and nanocarbon materials as HTLs. Modification in the particles' size or addition of metal NPs results in the LSPR effect, which increases the light absorption. Inorganic materials such as Mo and Ni were doped with V and Cu to tune the WF and increase conductivity and transparency, resulting in a high V_{oc}, FF, and J_{sc}. Hybrid layers, such as MoS₂:MoO₃, improved the electron-blocking properties and increased conductivity of the layer. Nanocarbon materials such as GO were doped with F₄TCNQ to induce a change in the WF by shifting the Fermi levels, resulting in an enhanced hole transport. CNTs were functionalized with amino groups to increase the charge-carrier properties and reduce R_s, improving FF and J_{sc}. HTLs can also be subjected to ultraviolet ozone (UVO), annealing, and microwave-annealing post-treatments to increase V_{oc}, FF, and J_{sc} due to the reduction of oxygen defects in the surface morphology. The most-used conjugated polymer is the PEDOT:PSS and its composites such as PEDOT:PSS with NPs, MOs, and GO either in bilayer or composite monolayer. PANI was the second choice of conducting polymers as HTLs. The different modification to PEDOT:PSS in many cases increases the J_{sc}, improves the conductivity, and decreases the recombination

loss of the device. In general, the addition of metallic NPs to PEDOT:PSS enhances the absorption ability of the photoactive layer, increases the conductivity, and improves the charge carrier collection by increasing the device performance. The incorporation of metal oxides mainly helps to (i) increase the stability of the device (e.g., MoO_3) by mitigating the degradation, (ii) serve as an electron blocking layer (e.g., V_2O_5), and (iii) suppress the charge recombination. On the other hand, GO addition to PEDOT:PSS improves the conductivity and increases the device resistance to degradation. Furthermore, CPEs were also used as HTL for OSCs; in general, these materials were pH-neutral layers that improved the stability of the devices and showed high electrical conductivity and good interface compatibility. In the last decade, the standard HTL small molecule has been spiro-OMeTAD; nevertheless, this review pointed out that research to optimize these materials is growing in activity and importance. Important points like shorter and more efficient chemical synthesis, access from cheaper starting materials, analysis of the active layer (perovskite or organic) interactions with the HTL small molecules, as well as better understanding of the charge transport process (carrier diffusion, recombination process) makes this field very important for optimization of the solar cells.

Additionally, large-area deposition techniques are mandatory to facilitate the commercialization of organic photovoltaics. Compared with the conventional spin-coating technique, laser-assisted and electrospray techniques allow the control of the surface morphology and thickness at low temperatures and short-time processing. The roll-to-roll technique is also attractive for large industrial-scale manufacturing of metal oxides, such as the inkjet printing of NiO_x . Overall, inorganic and nanocarbon HTLs are very favorable for OSCs, mainly because of their high stability, improved electrical properties, and transparency in the visible range. Solution processing is a great advantage of using small organic molecules as HTL. The continuous investigation of a vast number of new inorganic and organic HTLs, which can assure high efficiency, high stability, low costs, facile preparation, and improved film-forming properties over large areas, is essential for the future commercialization of OSCs. Therefore, not only the chemical or electrochemical properties of the prepared HTL materials are important to study, but also it is required to develop materials that fulfill the technological requirements to apply them at large scales. The future in this direction looks very promising.

Author Contributions: The manuscript was written through contributions of all authors. C.A.-C. and K.P.-I. wrote the draft manuscript. B.A.F.-U. and A.P.-C. revised the manuscript. A.P.-C. supervised the writing process and edited the manuscript. All authors have read and agreed to the published version of the manuscript.

Funding: This research was funded by German Academic Exchange Service (DAAD), grant number 57552347 and PAPIIT-DGAPA-UNAM project IN208919.

Acknowledgments: We kindly thank Prof. Dr. Ullrich Scherf for his sponsorship. A.P.-C. thanks the German Academic Exchange Service (DAAD) for the funding through the Re-invitation Programme for Former Scholarship Holders 2021 No. 57552347 and the University Yachay Tech for the internal grant No. Chem19-17. B.A.F.-U. recognizes the economic support through PAPIIT-DGAPA-UNAM project IN208919. Citlalit Martinez Soto is acknowledged for the technical support.

Conflicts of Interest: The authors declare no conflict of interest.

Abbreviations

Y6	(2,2'-((2Z,2Z)-((12,13-bis(2-ethylhexyl)-3,9-diundecyl-12,13-dihydro-[1,2,5]thiadiazolo[3,4-e]thieno[2'',3'':4',50]thieno[2',3':4,5]pyrrolo[3,2-g]thieno[2',3':4,5]thieno[3,2-b]indole-2,10-diyl)bis(methanylylidene))bis(5,6-difluoro-3-oxo-2,3-dihydro-1H-indene-2,1-diylidene))dimalononitrile)
O-IDTBR	(5Z,5'Z)-5,5'-[[7,7'-(4,4,9,9-tetraoctyl-4,9-dihydro-s-indaceno[1,2-b:5,6-b']dithiophene-2,7-diyl)bis(benzo[c][1,2,5]thiadiazole-7,4-diyl)]bis(methanylylidene)]bis(3-ethyl-2-thioxothiazolidin-4-one)
PC ₇₁ BM	(6,6)-phenyl-C71-butyric acid methyl ester
HPCzI	1,3,4,5,6,7-hexaphenyl-2-{3'-(9-ethylcarbazolyl)}-isoindole
ICBA	1',1'',4',4''-Tetrahydro-di[1,4]methanonaphthaleno[1,2:2',3',56,60:2'',3'']][5,6]fullerene-C60
TEMPO	2,2,6,6-tetramethylpiperidine-1-oxoammonium
IDIC	2,2'-[(4,4,9,9-tetrahexyl-4,9-dihydro-s-indaceno[1,2-b:5,6-b']dithiophene-2,7-diyl)bis[methylidyne(3-oxo-1H-indene-2,1(3H)-diylidene)]]bis-propanedinitrile
DIPO-Ph ₄	2,2',6,6'-tetraphenyl-dipyranlylidene
F4-TCNQ	2,3,5,6-tetrafluoro-7,7,8,8-tetracyanoquinodimethane
EGME	2-methoxyethanol
PTCDA	3,4,9,10-perylenetetracarboxylic dianhydride
IT-4F	3,9-bis(2-methylene-(3-(1,1-dicyanomethylene)-6,7-difluoro)-indanone))-5,5,11,11-tetrakis(4-hexylphenyl)-dithieno[2,3-d:2',3'-d']-s-indaceno[1,2-b:5,6-b']dithiophene
ITIC	3,9-bis(2-methylene-(3-(1,1-dicyanomethylene)-indanone))-5,5,11,11-tetrakis(4-hexylphenyl)-dithieno[2,3-d:2',3'-d']-s-indaceno[1,2-b:5,6-b']dithiophene
ITIC-Th	3,9-bis(2-methylene-(3-(1,1-dicyanomethylene)-indanone))-5,5,11,11-tetrakis(5-hexylthienyl)-dithieno[2,3-d:2',3'-d']-s-indaceno[1,2-b:5,6-b']dithiophene
CBP	4,4'-N,N'-dicarbazole-biphenyl
a-MWNTs	Amino-functionalized multi-walled carbon nanotubes
AHM	Ammonium heptamolybdate
AIL	Anode interfacial layer
AFM	Atomic force microscope
BPQDs	Black phosphorous quantum dots
bf-MWCNTs	Boronic acid functionalized multi-walled carbon nanotubes
BHJ	Bulk heterojunction
CNT	Carbon nanotubes
CTAB	Cetyltrimethylammonium bromide
CoO _x	Cobalt oxide
CPEs	Conjugated polyelectrolytes
CIGS	Copper indium gallium diselenide
CuO _x	Copper oxide
CuS _x	Copper sulfide
MeOPhN-DBC	Dibenzo[g,p]chrysene derivative, 3,6,11,14-tetramethoxyphenylamine-dibenzo[g,p]chrysene
DMSO	Dimethyl sulfoxide
DMF	Dimethylformamide
DC	Direct current
DA	Dopamine
ETL	Electron transport layer
EQE	External quantum efficiency
FF	Fill factor
GSL	Grafted sulfonated-acetone-formaldehyde lignin
GO	Graphene oxide
GQDs	Graphene quantum dots
g-C ₃ N ₄	Graphitic carbon nitrile
HOMO	High occupied molecular orbital

HTL	Hole transport layer
H _y MoO _{3-x}	Hydrogenated molybdenum oxide
ITO	Indium tin oxide
P _{in}	Input power
IPA	Isopropanol
LIL	Laser interference lithography
LSPR	Localized surface plasmon resonance
LUMO	Lowest unoccupied molecular orbital
P _{max}	Maximum power output
MO	Metal oxides
MW	Microwave
NPB	<i>N,N'</i> -bis(1-naphthalenyl) <i>N,N'</i> -bis-phenyl-(1,1'-biphenyl)-4,4'-diamine
BF-DPB	<i>N,N'</i> -((diphenyl- <i>N,N'</i> -bis)9,9,-dimethyl-fluoren-2-yl)-benzidine
NDs	Nanodots
NPs	Nanoparticles
NRs	Nanorods
NWs	Nanowires
NFD	Nickel formate dihydrate
NiO _x	Nickel oxide
NiS _x	Nickel sulfide
nGQDs	Nitrogen doped graphene quantum dots
V _{oc}	Open circuit voltage
OLEDs	Organic light-emitting diodes
OSCs	Organic solar cells
P _{out}	Output power
PCBM	Phenyl-C61-butyric acid methyl ester
PMA	Phosphomolybdic acid
PL	Photoluminescence
PV	Photovoltaic
PC	Phthalocyanine
PTB7	Poly [[4,8-bis[(2-ethylhexyl)oxy]benzo[1,2-b:4,5-b']dithiophene-2,6-diyl][3-fluoro-2-[(2-ethylhexyl)carbonyl]thieno[3,4-b]thiophenediyl]]
PCPDT	Poly 3,4-dithia-7 <i>H</i> -cyclopenta[a]pentalene
FBT-TH4	Poly 5,6-difluorobenzothiadiazole
PDMT	Poly(3,4-dimethoxythiophene)
PEDOT	Poly(3,4-ethylenedioxythiophene)
PEDOT:PSS	Poly(3,4-ethylenedioxythiophene)-poly(styrene sulfonate)
P3HT	Poly(3-hexylthiophene)
P3HT ₅₀ -b-PSS ₂₃	Poly(3-hexylthiophene)- <i>b</i> -poly(p-styrenesulfonate)
PEDOT-S	Poly(4-(2,3-dihydrothieno[3,4-b][1,4]dioxin-2-yl-methoxy)-1-butanefluoric acid)
PTPCz	Poly(carbazolyl triphenylethylene) derivative
PDMS	Poly(dimethylsiloxane)
PMMA	Poly(methylmethacrylate)
PSS	Poly(styrenesulfonate)
PM6	Poly[(2,6-(4,8-bis(5-(2-ethylhexyl)-4-fluorothiophen-2-yl)benzo[1,2-b:4,5-b']dithiophene))-co-(1,3-di(5-thiophene-2-yl)-5,7-bis(2-ethylhexyl)-benzo[1,2-c:4,5-c']dithiophene-4,8-dione)]
PBDB-T	Poly[(2,6-(4,8-bis(5-(2-ethylhexyl)thiophen-2-yl)benzo[1,2-b:4,5-b']dithiophene))-co-(1,3-di(5-thiophene-2-yl)-5,7-bis(2-ethylhexyl)benzo[1,2-c:4,5-c']dithiophene-4,8-dione)]
PffBT4T-2OD	Poly[(5,6-difluoro-2,1,3-benzothiadiazol-4,7-diyl)-alt-(3,3'''-di(2-octyldodecyl)-2,2';5',2'';5'',2'''-quaterthiophen-5,5'''-diyl)]
PFN	Poly[(9,9bis(3'-(<i>N,N</i> -dimethylamino)propyl)-2,7-fluorene)-alt-2,7-(9,9dioctylfluorene)]
PSFP-DTBTP	Poly[(9,9-bis(4-sulfonatobutyl sodium) fluorene-alt-phenylene)-ran-(4,7-di-2-thienyl-2,1,3-benzothiadiazole-alt-phenylene)]
TFB	Poly[(9,9-dioctylfluorenyl-2,7-diyl)-alt-(4,4'-(<i>N</i> -(4-butylphenyl)))]

PNDIT-F3N	Poly[[2,7-bis(2-ethylhexyl)-1,2,3,6,7,8-hexahydro-1,3,6,8-tetraoxobenzo[Imn][3,8]phenanthroline-4,9-diyl]-2,5-thiophenediyl[9,9-bis[3'((N,N-dimethyl)-N-ethylammonium)]propyl]-9H-fluorene-2,7-diyl]-2,5-thiophenediyl]
PhNa-1T	Poly[1,4-bis(4-sulfonatobutoxy)benzene-thiophene]
PCP-Na	Poly[2,6-(4,4-bis-(propane-1-sulfonate sodium)-4H-cyclopenta[2,1-b;3,4-b'] dithiophene)-alt-(4,4'-biphenyl)]
P3HTN	Poly[3-(6'-N,N,N-trimethyl ammonium)-hexylthiophene] bromide
PTB7-Th	Poly[4,8-bis(5-(2-ethylhexyl)thiophen-2-yl)benzo[1,2-b;4,5-b']dithiophene-2,6-diyl-alt-(4-(2-ethylhexyl)-3-fluorothieno[3,4-b]thiophene)-2-carboxylate-2-6-diyl]
PBDT-TS1	Poly[4,8-bis(5-(octylthio)thiophen-2-yl)benzo[1,2-b;4,5-b']dithiophene-2,6-diyl-alt-(4-(2-ethylhexyl)-3-fluorothieno[3,4-b]thiophene)-2-carboxylate-2-6-diyl]
PFtT-D	Poly[9,9-bis(4'-sulfonatobutyl)fluorene-alt-thieno[3,2-b]thiophene]
PFSe	Poly[9,9-bis(4'-sulfonatobutyl)fluorene-alt-selenophene]
PFT-D	Poly[9,9-bis(4'-sulfonatobutyl)fluorene-alt-thiophene]
PBDT-DTNT	Poly[benzodithiophene-bis(decyltetradecyl-thien)naphthothiadiazole]
PCDTBT	Poly[N-9'-heptadecanyl-2,7-carbazole-alt-5,5(4',7'-di-2-thienyl-2',1',3'-benzothiadiazole)]
PANI	Polyaniline
PEG	Polyethylene glycol
PSC	Polymer solar cell
PMC	Polyuclear metal-oxo clusters
p-TPCF	Polytriphenylcarbazole fluoranthene
PCE	Power conversion efficiency
QDs	Quantum dots
rrP3HT	Regioregular poly(3-hexylthiophene-2,5-diyl)
RMS	Root meand square
SEM	Scanning electron microscopy
R _s	Series resistance
J _{sc}	Short circuit current
R _{sh}	Shunt resistance
SWCNTs	Single-walled carbon nanotubes
SILAR	Successive ionic layer adsorption and reaction
F ₄ TCNQ	Tetrafluorotetracyanoquino-dimethane
TTA	Tetrathiafulvalene
TTF-py	Tetrathiafulvalene pyridine derivative
P3HT-Si	Triethoxysilane terminated poly(3-hexylthiophene)
WO _x	Tungsten oxide
WS _x	Tungsten sulfide
UVO	Ultraviolet ozone
uSWNT	Unzipped single-walled carbon nanotubes
VO _x	Vanadium oxide
VoPC	Vanadylphthalocyanine
WF	Work function

References

- Owusu, P.A.; Asumadu-Sarkodie, S. A review of renewable energy sources, sustainability issues and climate change mitigation. *Cogent Eng.* **2016**, *3*, 1167990. [[CrossRef](#)]
- Ellabban, O.; Abu-Rub, H.; Blaabjerg, F. Renewable energy resources: Current status, future prospects and their enabling technology. *Renew. Sustain. Energy Rev.* **2014**, *39*, 748–764. [[CrossRef](#)]
- Luqman, M.; Ahmad, S.R.; Khan, S.; Ahmad, U.; Raza, A.; Akmal, F. Estimation of Solar Energy Potential from Rooftop of Punjab Government Servants Cooperative Housing Society Lahore Using GIS. *Smart Grid Renew. Energy* **2015**, *6*, 128–139. [[CrossRef](#)]
- Kabir, E.; Kumar, P.; Kumar, S.; Adelodun, A.A.; Kim, K.-H. Solar energy: Potential and future prospects. *Renew. Sustain. Energy Rev.* **2018**, *82*, 894–900. [[CrossRef](#)]
- Hosenuzzaman, M.; Rahim, N.A.; Selvaraj, J.; Hasanuzzaman, M.; Malek, A.B.M.A.; Nahar, A. Global prospects, progress, policies, and environmental impact of solar photovoltaic power generation. *Renew. Sustain. Energy Rev.* **2015**, *41*, 284–297. [[CrossRef](#)]

6. Kannan, N.; Vakeesan, D. Solar energy for future world:—A review. *Renew. Sustain. Energy Rev.* **2016**, *62*, 1092–1105. [[CrossRef](#)]
7. Goswami, D.Y.; Vijayaraghavan, S.; Lu, S.; Tamm, G. New and emerging developments in solar energy. *Sol. Energy* **2004**, *76*, 33–43. [[CrossRef](#)]
8. Li, G.; Zhu, R.; Yang, Y. Polymer solar cells. *Nat. Photonics* **2012**, *6*, 153–161. [[CrossRef](#)]
9. Lin, Y.; Shao, Y.; Dai, J.; Li, T.; Liu, Y.; Dai, X.; Xiao, X.; Deng, Y.; Gruverman, A.; Zeng, X.C.; et al. Metallic surface doping of metal halide perovskites. *Nat. Commun.* **2021**, *12*, 7. [[CrossRef](#)]
10. Ur Rehman, S.; Noman, M.; Khan, A.D.; Saboor, A.; Ahmad, M.S.; Khan, H.U. Synthesis of polyvinyl acetate /graphene nanocomposite and its application as an electrolyte in dye sensitized solar cells. *Optik* **2020**, *202*, 163591. [[CrossRef](#)]
11. Liu, M.; Johnston, M.B.; Snaith, H.J. Efficient planar heterojunction perovskite solar cells by vapour deposition. *Nature* **2013**, *501*, 395–398. [[CrossRef](#)]
12. Mathew, S.; Yella, A.; Gao, P.; Humphry-Baker, R.; Curchod, B.F.E.; Ashari-Astani, N.; Tavernelli, I.; Rothlisberger, U.; Nazeeruddin, M.K.; Grätzel, M. Dye-sensitized solar cells with 13% efficiency achieved through the molecular engineering of porphyrin sensitizers. *Nat. Chem.* **2014**, *6*, 242–247. [[CrossRef](#)] [[PubMed](#)]
13. Liu, S.; Yuan, J.; Deng, W.; Luo, M.; Xie, Y.; Liang, Q.; Zou, Y.; He, Z.; Wu, H.; Cao, Y. High-efficiency organic solar cells with low non-radiative recombination loss and low energetic disorder. *Nat. Photonics* **2020**, *14*, 300–305. [[CrossRef](#)]
14. Chuang, C.-H.M.; Brown, P.R.; Bulović, V.; Bawendi, M.G. Improved performance and stability in quantum dot solar cells through band alignment engineering. *Nat. Mater.* **2014**, *13*, 796–801. [[CrossRef](#)] [[PubMed](#)]
15. Bernède, J.C. Organic photovoltaic cells: History, principle and techniques. *J. Chil. Chem. Soc.* **2008**, *53*. [[CrossRef](#)]
16. Kearns, D.; Calvin, M. Photovoltaic Effect and Photoconductivity in Laminated Organic Systems. *J. Chem. Phys.* **1958**, *29*, 950–951. [[CrossRef](#)]
17. Tang, C.W. Two-layer organic photovoltaic cell. *Appl. Phys. Lett.* **1986**, *48*, 183–185. [[CrossRef](#)]
18. Sariciftci, N.S.; Smilowitz, L.; Heeger, A.J.; Wudl, F. Semiconducting polymers (as donors) and buckminsterfullerene (as acceptor): Photoinduced electron transfer and heterojunction devices. *Synth. Met.* **1993**, *59*, 333–352. [[CrossRef](#)]
19. Yu, G.; Gao, J.; Hummelen, J.C.; Wudl, F.; Heeger, A.J. Polymer Photovoltaic Cells: Enhanced Efficiencies via a Network of Internal Donor-Acceptor Heterojunctions. *Science* **1995**, *270*, 1789–1791. [[CrossRef](#)]
20. Yin, Z.; Wei, J.; Zheng, Q. Interfacial Materials for Organic Solar Cells: Recent Advances and Perspectives. *Adv. Sci.* **2016**, *3*, 1500362. [[CrossRef](#)]
21. Green, M.A. Recent developments in photovoltaics. *Sol. Energy* **2004**, *76*, 3–8. [[CrossRef](#)]
22. Darling, S.B.; You, F. The case for organic photovoltaics. *RSC Adv.* **2013**, *3*, 17633. [[CrossRef](#)]
23. Liu, Q.; Jiang, Y.; Jin, K.; Qin, J.; Xu, J.; Li, W.; Xiong, J.; Liu, J.; Xiao, Z.; Sun, K.; et al. 18% Efficiency organic solar cells. *Sci. Bull.* **2020**, *65*, 272–275. [[CrossRef](#)]
24. Green, M.; Dunlop, E.; Hohl-Ebinger, J.; Yoshita, M.; Kopidakis, N.; Hao, X. Solar cell efficiency tables (version 57). *Prog. Photovolt. Res. Appl.* **2021**, *29*, 3–15. [[CrossRef](#)]
25. Salim, M.B.; Nekovei, R.; Jeyakumar, R. Organic tandem solar cells with 18.6% efficiency. *Sol. Energy* **2020**, *198*, 160–166. [[CrossRef](#)]
26. Dennler, G.; Scharber, M.C.; Brabec, C.J. Polymer-Fullerene Bulk-Heterojunction Solar Cells. *Adv. Mater.* **2009**, *21*, 1323–1338. [[CrossRef](#)]
27. Zhao, W.; Li, S.; Yao, H.; Zhang, S.; Zhang, Y.; Yang, B.; Hou, J. Molecular Optimization Enables over 13% Efficiency in Organic Solar Cells. *J. Am. Chem. Soc.* **2017**, *139*, 7148–7151. [[CrossRef](#)]
28. Hou, J.; Inganäs, O.; Friend, R.H.; Gao, F. Organic solar cells based on non-fullerene acceptors. *Nat. Mater.* **2018**, *17*, 119–128. [[CrossRef](#)]
29. Jacoby, M. The future of low-cost solar cells. *Chem. Eng. News* **2016**, *94*, 30–35.
30. Riede, M.; Spoltore, D.; Leo, K. Organic Solar Cells—The Path to Commercial Success. *Adv. Energy Mater.* **2021**, *11*, 2002653. [[CrossRef](#)]
31. Krebs, F.C.; Espinosa, N.; Hösel, M.; Søndergaard, R.R.; Jørgensen, M. 25th anniversary article: Rise to power—OPV-based solar parks. *Adv. Mater.* **2014**, *26*, 29–39. [[CrossRef](#)] [[PubMed](#)]
32. Yan, C.; Barlow, S.; Wang, Z.; Yan, H.; Jen, A.K.Y.; Marder, S.R.; Zhan, X. Non-fullerene acceptors for organic solar cells. *Nat. Rev. Mater.* **2018**, *3*, 18003. [[CrossRef](#)]
33. Duan, C.; Huang, F.; Cao, Y. Solution processed thick film organic solar cells. *Polym. Chem.* **2015**, *6*, 8081–8098. [[CrossRef](#)]
34. Scharber, M.C.; Sariciftci, N.S. Efficiency of bulk-heterojunction organic solar cells. *Prog. Polym. Sci.* **2013**, *38*, 1929–1940. [[CrossRef](#)]
35. Yeh, N.; Yeh, P. Organic solar cells: Their developments and potentials. *Renew. Sustain. Energy Rev.* **2013**, *21*, 421–431. [[CrossRef](#)]
36. Park, J.H.; Lee, T.-W.; Chin, B.-D.; Wang, D.H.; Park, O.O. Roles of Interlayers in Efficient Organic Photovoltaic Devices. *Macromol. Rapid Commun.* **2010**, *31*, 2095–2108. [[CrossRef](#)]
37. Lai, T.-H.; Tsang, S.-W.; Manders, J.R.; Chen, S.; So, F. Properties of interlayer for organic photovoltaics. *Mater. Today* **2013**, *16*, 424–432. [[CrossRef](#)]
38. Steim, R.; Kogler, F.R.; Brabec, C.J. Interface materials for organic solar cells. *J. Mater. Chem.* **2010**, *20*, 2499. [[CrossRef](#)]
39. Po, R.; Carbonera, C.; Bernardi, A.; Camaioni, N. The role of buffer layers in polymer solar cells. *Energy Environ. Sci.* **2011**, *4*, 285–310. [[CrossRef](#)]

40. Roman, L.S.; Mammo, W.; Pettersson, L.A.A.; Andersson, M.R.; Inganäs, O. High Quantum Efficiency Polythiophene. *Adv. Mater.* **1998**, *10*, 774–777. [[CrossRef](#)]
41. Tian, L.; Xue, Q.; Hu, Z.; Huang, F. Recent advances of interface engineering for non-fullerene organic solar cells. *Org. Electron.* **2021**, *93*, 106141. [[CrossRef](#)]
42. Palilis, L.C.; Vasilopoulou, M.; Verykios, A.; Soultati, A.; Polydorou, E.; Argitis, P.; Davazoglou, D.; Mohd Yusoff, B.A.R.; Nazeeruddin, M.K. Inorganic and Hybrid Interfacial Materials for Organic and Perovskite Solar Cells. *Adv. Energy Mater.* **2020**, *10*, 2000910. [[CrossRef](#)]
43. Gusain, A.; Faria, R.M.; Miranda, P.B. Polymer Solar Cells—Interfacial Processes Related to Performance Issues. *Front. Chem.* **2019**, *7*, 61. [[CrossRef](#)]
44. Amollo, T.A.; Mola, G.T.; Nyamori, V.O. Organic solar cells: Materials and prospects of graphene for active and interfacial layers. *Crit. Rev. Solid State Mater. Sci.* **2020**, *45*, 261–288. [[CrossRef](#)]
45. Wu, C.; Wang, K.; Batmunkh, M.; Bati, A.S.R.; Yang, D.; Jiang, Y.; Hou, Y.; Shapter, J.G.; Priya, S. Multifunctional nanostructured materials for next generation photovoltaics. *Nano Energy* **2020**, *70*, 104480. [[CrossRef](#)]
46. Huang, Z.; Ouyang, D.; Shih, C.; Yang, B.; Choy, W.C.H. Solution-Processed Ternary Oxides as Carrier Transport/Injection Layers in Optoelectronics. *Adv. Energy Mater.* **2020**, *10*, 1900903. [[CrossRef](#)]
47. Li, Y. Molecular Design of Photovoltaic Materials for Polymer Solar Cells: Toward Suitable Electronic Energy Levels and Broad Absorption. *Acc. Chem. Res.* **2012**, *45*, 723–733. [[CrossRef](#)] [[PubMed](#)]
48. Yao, H.; Ye, L.; Zhang, H.; Li, S.; Zhang, S.; Hou, J. Molecular Design of Benzodithiophene-Based Organic Photovoltaic Materials. *Chem. Rev.* **2016**, *116*, 7397–7457. [[CrossRef](#)]
49. Kim, J.Y.; Lee, K.; Coates, N.E.; Moses, D.; Nguyen, T.-Q.; Dante, M.; Heeger, A.J. Efficient Tandem Polymer Solar Cells Fabricated by All-Solution Processing. *Science* **2007**, *317*, 222–225. [[CrossRef](#)]
50. Meillaud, F.; Shah, A.; Droz, C.; Vallat-Sauvain, E.; Miazza, C. Efficiency limits for single-junction and tandem solar cells. *Sol. Energy Mater. Sol. Cells* **2006**, *90*, 2952–2959. [[CrossRef](#)]
51. Lee, Y.-J.; Adkison, B.L.; Xu, L.; Kramer, A.A.; Hsu, J.W.P. Comparison of conventional and inverted organic photovoltaic devices with controlled illumination area and extraction layers. *Sol. Energy Mater. Sol. Cells* **2016**, *144*, 592–599. [[CrossRef](#)]
52. Nunzi, J.-M. Organic photovoltaic materials and devices. *Comptes Rendus Phys.* **2002**, *3*, 523–542. [[CrossRef](#)]
53. Shrotriya, V.; Li, G.; Yao, Y.; Moriarty, T.; Emery, K.; Yang, Y. Accurate Measurement and Characterization of Organic Solar Cells. *Adv. Funct. Mater.* **2006**, *16*, 2016–2023. [[CrossRef](#)]
54. Qi, B.; Wang, J. Fill factor in organic solar cells. *Phys. Chem. Chem. Phys.* **2013**, *15*, 8972. [[CrossRef](#)] [[PubMed](#)]
55. Parker, I.D. Carrier tunneling and device characteristics in polymer light-emitting diodes. *J. Appl. Phys.* **1994**, *75*, 1656–1666. [[CrossRef](#)]
56. Elumalai, N.K.; Uddin, A. Open circuit voltage of organic solar cells: An in-depth review. *Energy Environ. Sci.* **2016**, *9*, 391–410. [[CrossRef](#)]
57. Ratcliff, E.L.; Zacher, B.; Armstrong, N.R. Selective Interlayers and Contacts in Organic Photovoltaic Cells. *J. Phys. Chem. Lett.* **2011**, *2*, 1337–1350. [[CrossRef](#)] [[PubMed](#)]
58. Mihailetchi, V.D.; Blom, P.W.M.; Hummelen, J.C.; Rispens, M.T. Cathode dependence of the open-circuit voltage of polymer:fullerene bulk heterojunction solar cells. *J. Appl. Phys.* **2003**, *94*, 6849–6854. [[CrossRef](#)]
59. Günes, S.; Neugebauer, H.; Sariciftci, N.S. Conjugated Polymer-Based Organic Solar Cells. *Chem. Rev.* **2007**, *107*, 1324–1338. [[CrossRef](#)]
60. Street, R.A.; Song, K.W.; Cowan, S. Influence of series resistance on the photocurrent analysis of organic solar cells. *Org. Electron.* **2011**, *12*, 244–248. [[CrossRef](#)]
61. Servaites, J.D.; Yeganeh, S.; Marks, T.J.; Ratner, M.A. Efficiency Enhancement in Organic Photovoltaic Cells: Consequences of Optimizing Series Resistance. *Adv. Funct. Mater.* **2010**, *20*, 97–104. [[CrossRef](#)]
62. Antohe, S.; Iftimie, S.; Hrostea, L.; Antohe, V.A.; Girtan, M. A critical review of photovoltaic cells based on organic monomeric and polymeric thin film heterojunctions. *Thin Solid Films* **2017**, *642*, 219–231. [[CrossRef](#)]
63. Antohe, S.; Ion, L.; Tomozeiu, N.; Stoica, T.; Barna, E. Electrical and photovoltaic properties of photosensitised ITO/a-Si:H p-i-n/TPyP/Au cells. *Sol. Energy Mater. Sol. Cells* **2000**, *62*, 207–216. [[CrossRef](#)]
64. Antohe, S.; Ruxandra, V.; Tugulea, L.; Gheorghe, V.; Ionascu, D. Three-Layered Photovoltaic Cell with an Enlarged Photoactive Region of Codeposited Dyes. *J. Phys. III* **1996**, *6*, 1133–1144. [[CrossRef](#)]
65. Proctor, C.M.; Nguyen, T.-Q. Effect of leakage current and shunt resistance on the light intensity dependence of organic solar cells. *Appl. Phys. Lett.* **2015**, *106*, 083301. [[CrossRef](#)]
66. Wurfel, U.; Cuevas, A.; Wurfel, P. Charge Carrier Separation in Solar Cells. *IEEE J. Photovolt.* **2015**, *5*, 461–469. [[CrossRef](#)]
67. Yip, H.-L.; Jen, A.K.Y. Recent advances in solution-processed interfacial materials for efficient and stable polymer solar cells. *Energy Environ. Sci.* **2012**, *5*, 5994. [[CrossRef](#)]
68. Braun, S.; Salaneck, W.R.; Fahlman, M. Energy-Level Alignment at Organic/Metal and Organic/Organic Interfaces. *Adv. Mater.* **2009**, *21*, 1450–1472. [[CrossRef](#)]
69. Tokito, S.; Noda, K.; Taga, Y. Metal oxides as a hole-injecting layer for an organic electroluminescent device. *J. Phys. D Appl. Phys.* **1996**, *29*, 2750–2753. [[CrossRef](#)]

70. Meyer, J.; Hamwi, S.; Kröger, M.; Kowalsky, W.; Riedl, T.; Kahn, A. Transition Metal Oxides for Organic Electronics: Energetics, Device Physics and Applications. *Adv. Mater.* **2012**, *24*, 5408–5427. [[CrossRef](#)]
71. Chen, L.-M.; Xu, Z.; Hong, Z.; Yang, Y. Interface investigation and engineering—Achieving high performance polymer photovoltaic devices. *J. Mater. Chem.* **2010**, *20*, 2575. [[CrossRef](#)]
72. Curiel, D.; Más-Montoya, M. Hole Transporting Layers in Printable Solar Cells. In *Printable Solar Cells*; John Wiley & Sons, Inc.: Hoboken, NJ, USA, 2017; pp. 93–161.
73. Shrotriya, V.; Li, G.; Yao, Y.; Chu, C.-W.; Yang, Y. Transition metal oxides as the buffer layer for polymer photovoltaic cells. *Appl. Phys. Lett.* **2006**, *88*, 073508. [[CrossRef](#)]
74. Han, S.; Shin, W.S.; Seo, M.; Gupta, D.; Moon, S.-J.; Yoo, S. Improving performance of organic solar cells using amorphous tungsten oxides as an interfacial buffer layer on transparent anodes. *Org. Electron.* **2009**, *10*, 791–797. [[CrossRef](#)]
75. Irwin, M.D.; Buchholz, D.B.; Hains, A.W.; Chang, R.P.H.; Marks, T.J. p-Type semiconducting nickel oxide as an efficiency-enhancing anode interfacial layer in polymer bulk-heterojunction solar cells. *Proc. Natl. Acad. Sci. USA* **2008**, *105*, 2783–2787. [[CrossRef](#)]
76. Wang, K.; Ren, H.; Yi, C.; Liu, C.; Wang, H.; Huang, L.; Zhang, H.; Karim, A.; Gong, X. Solution-Processed Fe₃O₄ Magnetic Nanoparticle Thin Film Aligned by an External Magnetostatic Field as a Hole Extraction Layer for Polymer Solar Cells. *ACS Appl. Mater. Interfaces* **2013**, *5*, 10325–10330. [[CrossRef](#)]
77. Gu, X.; Cui, W.; Li, H.; Wu, Z.; Zeng, Z.; Lee, S.-T.; Zhang, H.; Sun, B. A Solution-Processed Hole Extraction Layer Made from Ultrathin MoS₂ Nanosheets for Efficient Organic Solar Cells. *Adv. Energy Mater.* **2013**, *3*, 1262–1268. [[CrossRef](#)]
78. Xu, H.; Xu, H.; Yuan, F.; Zhou, D.; Liao, X.; Chen, L.; Chen, Y.; Chen, Y. Hole transport layers for organic solar cells: Recent progress and prospects. *J. Mater. Chem. A* **2020**, *8*, 11478–11492. [[CrossRef](#)]
79. Kawano, K.; Pacios, R.; Poplavskyy, D.; Nelson, J.; Bradley, D.D.C.; Durrant, J.R. Degradation of organic solar cells due to air exposure. *Sol. Energy Mater. Sol. Cells* **2006**, *90*, 3520–3530. [[CrossRef](#)]
80. Wang, T.; Scarratt, N.W.; Yi, H.; Dunbar, A.D.F.; Pearson, A.J.; Watters, D.C.; Glen, T.S.; Brook, A.C.; Kingsley, J.; Buckley, A.R.; et al. Fabricating High Performance, Donor-Acceptor Copolymer Solar Cells by Spray-Coating in Air. *Adv. Energy Mater.* **2013**, *3*, 505–512. [[CrossRef](#)]
81. Krebs, F.C. Fabrication and processing of polymer solar cells: A review of printing and coating techniques. *Sol. Energy Mater. Sol. Cells* **2009**, *93*, 394–412. [[CrossRef](#)]
82. Terán-Alcocer, Á.; Bravo-Plascencia, F.; Cevallos-Morillo, C.; Palma-Cando, A. Electrochemical Sensors Based on Conducting Polymers for the Aqueous Detection of Biologically Relevant Molecules. *Nanomaterials* **2021**, *11*, 252. [[CrossRef](#)] [[PubMed](#)]
83. Zhitomirsky, I.; Niewczas, M.; Petric, A. Electrodeposition of hybrid organic–inorganic films containing iron oxide. *Mater. Lett.* **2003**, *57*, 1045–1050. [[CrossRef](#)]
84. Krebs, F.C. Polymer solar cell modules prepared using roll-to-roll methods: Knife-over-edge coating, slot-die coating and screen printing. *Sol. Energy Mater. Sol. Cells* **2009**, *93*, 465–475. [[CrossRef](#)]
85. Jung, J.W.; Jo, W.H. Annealing-Free High Efficiency and Large Area Polymer Solar Cells Fabricated by a Roller Painting Process. *Adv. Funct. Mater.* **2010**, *20*, 2355–2363. [[CrossRef](#)]
86. Yang, B.; Chen, Y.; Cui, Y.; Liu, D.; Xu, B.; Hou, J. Over 100-nm-Thick MoO_x Films with Superior Hole Collection and Transport Properties for Organic Solar Cells. *Adv. Energy Mater.* **2018**, *8*, 1800698. [[CrossRef](#)]
87. Lou, X.W.; Zeng, H.C. Complex α -MoO₃ Nanostructures with External Bonding Capacity for Self-Assembly. *J. Am. Chem. Soc.* **2003**, *125*, 2697–2704. [[CrossRef](#)]
88. Pan, W.; Tian, R.; Jin, H.; Guo, Y.; Zhang, L.; Wu, X.; Zhang, L.; Han, Z.; Liu, G.; Li, J.; et al. Structure, Optical, and Catalytic Properties of Novel Hexagonal Metastable h-MoO₃ Nano- and Microrods Synthesized with Modified Liquid-Phase Processes. *Chem. Mater.* **2010**, *22*, 6202–6208. [[CrossRef](#)]
89. Kyaw, A.K.K.; Sun, X.W.; Jiang, C.Y.; Lo, G.Q.; Zhao, D.W.; Kwong, D.L. An inverted organic solar cell employing a sol-gel derived ZnO electron selective layer and thermal evaporated MoO₃ hole selective layer. *Appl. Phys. Lett.* **2008**, *93*, 221107. [[CrossRef](#)]
90. Lee, D.; Kim, J.; Park, G.; Bae, H.W.; An, M.; Kim, J.Y. Enhanced Operating Temperature Stability of Organic Solar Cells with Metal Oxide Hole Extraction Layer. *Polymers* **2020**, *12*, 992. [[CrossRef](#)]
91. Liao, X.; Jeong, A.R.; Wilks, R.G.; Wiesner, S.; Rusu, M.; Félix, R.; Xiao, T.; Hartmann, C.; Bär, M. Tunability of MoO₃ Thin-Film Properties Due to Annealing in Situ Monitored by Hard X-ray Photoemission. *ACS Omega* **2019**, *4*, 10985–10990. [[CrossRef](#)]
92. Boudaoud, L.; Benramdane, N.; Desfeux, R.; Khelifa, B.; Mathieu, C. Structural and optical properties of MoO₃ and V₂O₅ thin films prepared by Spray Pyrolysis. *Catal. Today* **2006**, *113*, 230–234. [[CrossRef](#)]
93. Inzani, K.; Nematollahi, M.; Selbach, S.M.; Grande, T.; Waalekalv, M.L.; Brakstad, T.; Reenaas, T.W.; Kildemo, M.; Vullum-Bruer, F. Tailoring properties of nanostructured MoO₃-x thin films by aqueous solution deposition. *Appl. Surf. Sci.* **2018**, *459*, 822–829. [[CrossRef](#)]
94. Bortoti, A.A.; de Gavanski, A.F.; Velazquez, Y.R.; Galli, A.; de Castro, E.G. Facile and low cost oxidative conversion of MoS₂ in α -MoO₃: Synthesis, characterization and application. *J. Solid State Chem.* **2017**, *252*, 111–118. [[CrossRef](#)]
95. Ji, R.; Cheng, J.; Yang, X.; Yu, J.; Li, L. Enhanced charge carrier transport in spray-cast organic solar cells using solution processed MoO₃ micro arrays. *RSC Adv.* **2017**, *7*, 3059–3065. [[CrossRef](#)]
96. Kim, J.-H.; Park, E.-K.; Kim, J.-H.; Cho, H.J.; Lee, D.-H.; Kim, Y.-S. Improving charge transport of P3HT:PCBM organic solar cell using MoO₃ nanoparticles as an interfacial buffer layer. *Electron. Mater. Lett.* **2016**, *12*, 383–387. [[CrossRef](#)]

97. Choy, W.C.H.; Ren, X. Plasmon-Electrical Effects on Organic Solar Cells by Incorporation of Metal Nanostructures. *IEEE J. Sel. Top. Quantum Electron.* **2016**, *22*, 1–9. [CrossRef]
98. Bobeico, E.; Mercaldo, L.V.; Morvillo, P.; Usatii, I.; Della Noce, M.; Lancellotti, L.; Sasso, C.; Ricciardi, R.; Delli Veneri, P. Evaporated MoO_x as General Back-Side Hole Collector for Solar Cells. *Coatings* **2020**, *10*, 763. [CrossRef]
99. Jagadamma, L.K.; Hu, H.; Kim, T.; Ndjawa, G.O.N.; Mansour, A.E.; El Labban, A.; Faria, J.C.D.; Munir, R.; Anjum, D.H.; McLachlan, M.A.; et al. Solution-processable MoO_x nanocrystals enable highly efficient reflective and semitransparent polymer solar cells. *Nano Energy* **2016**, *28*, 277–287. [CrossRef]
100. Wang, J.; Jia, X.; Zhou, J.; Pan, L.; Huang, S.; Chen, X. Improved Performance of Polymer Solar Cells by Thermal Evaporation of AgAl Alloy Nanostructures into the Hole-Transport Layer. *ACS Appl. Mater. Interfaces* **2016**, *8*, 26098–26104. [CrossRef]
101. Cong, S.; Hadipour, A.; Sugahara, T.; Wei, T.; Jiu, J.; Ranjbar, S.; Hirose, Y.; Karakawa, M.; Nagao, S.; Aernouts, T.; et al. Modifying the valence state of molybdenum in the efficient oxide buffer layer of organic solar cells via a mild hydrogen peroxide treatment. *J. Mater. Chem. C* **2017**, *5*, 889–895. [CrossRef]
102. Jung, S.; Lee, J.; Kim, U.; Park, H. Solution-Processed Molybdenum Oxide with Hydroxyl Radical-Induced Oxygen Vacancy as an Efficient and Stable Interfacial Layer for Organic Solar Cells. *Sol. RRL* **2020**, *4*, 1900420. [CrossRef]
103. Kobori, T.; Kamata, N.; Fukuda, T. Effect of annealing-induced oxidation of molybdenum oxide on organic photovoltaic device performance. *Org. Electron.* **2016**, *37*, 126–133. [CrossRef]
104. Li, Y.; Yu, H.; Huang, X.; Wu, Z.; Chen, M. A simple synthesis method to prepare a molybdenum oxide hole-transporting layer for efficient polymer solar cells. *RSC Adv.* **2017**, *7*, 7890–7900. [CrossRef]
105. Cheng, F.; Wu, Y.; Shen, Y.; Cai, X.; Li, L. Enhancing the performance and stability of organic solar cells using solution processed MoO₃ as hole transport layer. *RSC Adv.* **2017**, *7*, 37952–37958. [CrossRef]
106. Cai, P.; Ren, P.; Huang, X.; Zhang, X.; Zhan, T.; Xiong, J.; Xue, X.; Wang, Z.; Zhang, J.; Chen, J. An Ultraviolet-Deposited MoO₃ Film as Anode Interlayer for High-Performance Polymer Solar Cells. *Adv. Mater. Interfaces* **2020**, *7*, 1901912. [CrossRef]
107. Tran, H.N.; Park, S.; Wibowo, F.T.A.; Krishna, N.V.; Kang, J.H.; Seo, J.H.; Nguyen-Phu, H.; Jang, S.; Cho, S. 17% Non-Fullerene Organic Solar Cells with Annealing-Free Aqueous MoO_x. *Adv. Sci.* **2020**, *7*, 2002395. [CrossRef]
108. Irfan; Ding, H.; Gao, Y.; Small, C.; Kim, D.Y.; Subbiah, J.; So, F. Energy level evolution of air and oxygen exposed molybdenum trioxide films. *Appl. Phys. Lett.* **2010**, *96*, 243307. [CrossRef]
109. Vasilopoulou, M.; Soultati, A.; Argitis, P.; Stergiopoulos, T.; Davazoglou, D. Fast Recovery of the High Work Function of Tungsten and Molybdenum Oxides via Microwave Exposure for Efficient Organic Photovoltaics. *J. Phys. Chem. Lett.* **2014**, *5*, 1871–1879. [CrossRef]
110. Soultati, A.; Kostis, I.; Argitis, P.; Dimotikali, D.; Kennou, S.; Gardelis, S.; Speliotis, T.; Kontos, A.G.; Davazoglou, D.; Vasilopoulou, M. Dehydration of molybdenum oxide hole extraction layers via microwave annealing for the improvement of efficiency and lifetime in organic solar cells. *J. Mater. Chem. C* **2016**, *4*, 7683–7694. [CrossRef]
111. Chang, F.-K.; Huang, Y.-C.; Jeng, J.-S.; Chen, J.-S. Band offset of vanadium-doped molybdenum oxide hole transport layer in organic photovoltaics. *Solid-State. Electron.* **2016**, *122*, 18–22. [CrossRef]
112. Marchal, W.; Verboven, I.; Kesters, J.; Moeremans, B.; De Dobbelaere, C.; Bonneux, G.; Elen, K.; Conings, B.; Maes, W.; Boyen, H.G.; et al. Steering the properties of MoO_x hole transporting layers in OPVs and OLEDs: Interface morphology vs. electronic structure. *Materials* **2017**, *10*, 123. [CrossRef] [PubMed]
113. Bai, Y.; Zhao, C.; Guo, Q.; Zhang, J.; Hu, S.; Liu, J.; Hayat, T.; Alsaedi, A.; Tan, Z. Enhancing the electron blocking ability of n-type MoO₃ by doping with p-type NiO for efficient nonfullerene polymer solar cells. *Org. Electron.* **2019**, *68*, 168–175. [CrossRef]
114. Li, X.; Xie, F.; Zhang, S.; Hou, J.; Choy, W.C.H. MoO_x and V₂O_x as hole and electron transport layers through functionalized intercalation in normal and inverted organic optoelectronic devices. *Light Sci. Appl.* **2015**, *4*, e273. [CrossRef]
115. Li, X.; Xie, F.; Zhang, S.; Hou, J.; Choy, W.C.H. Over 1.1 eV Workfunction Tuning of Cesium Intercalated Metal Oxides for Functioning as Both Electron and Hole Transport Layers in Organic Optoelectronic Devices. *Adv. Funct. Mater.* **2014**, *24*, 7348–7356. [CrossRef]
116. Yoon, S.; Kim, H.; Shin, E.-Y.; Bae, I.-G.; Park, B.; Noh, Y.-Y.; Hwang, I. Enhanced hole extraction by interaction between CuI and MoO₃ in the hole transport layer of organic photovoltaic devices. *Org. Electron.* **2016**, *32*, 200–207. [CrossRef]
117. Li, Z.; Guo, W.; Liu, C.; Zhang, X.; Li, S.; Guo, J.; Zhang, L. Impedance investigation of the highly efficient polymer solar cells with composite CuBr₂ /MoO₃ hole transport layer. *Phys. Chem. Chem. Phys.* **2017**, *19*, 20839–20846. [CrossRef] [PubMed]
118. Li, Y.; Yu, H.; Huang, X.; Wu, Z.; Xu, H. Improved performance for polymer solar cells using CTAB-modified MoO₃ as an anode buffer layer. *Sol. Energy Mater. Sol. Cells* **2017**, *171*, 72–84. [CrossRef]
119. Kang, Q.; Zu, Y.; Liao, Q.; Zheng, Z.; Yao, H.; Zhang, S.; He, C.; Xu, B.; Hou, J. An inorganic molecule-induced electron transfer complex for highly efficient organic solar cells. *J. Mater. Chem. A* **2020**, *8*, 5580–5586. [CrossRef]
120. Kwon, K.C.; Lee, T.H.; Choi, S.; Choi, K.S.; Gim, S.O.; Bae, S.-R.; Lee, J.-L.; Jang, H.W.; Kim, S.Y. Synthesis of atomically thin alloyed molybdenum-tungsten disulfides thin films as hole transport layers in organic light-emitting diodes. *Appl. Surf. Sci.* **2021**, *541*, 148529. [CrossRef]
121. Cheng, P.-P.; Zhou, L.; Li, J.-A.; Li, Y.-Q.; Lee, S.-T.; Tang, J.-X. Light trapping enhancement of inverted polymer solar cells with a nanostructured scattering rear electrode. *Org. Electron.* **2013**, *14*, 2158–2163. [CrossRef]
122. Zhang, W.; Lan, W.; Lee, M.H.; Singh, J.; Zhu, F. A versatile solution-processed MoO₃/Au nanoparticles/MoO₃ hole contact for high performing PEDOT:PSS-free organic solar cells. *Org. Electron.* **2018**, *52*, 1–6. [CrossRef]

123. Hofmann, M.; Hofmann, H.; Hagelüken, C.; Hool, A. Critical raw materials: A perspective from the materials science community. *Sustain. Mater. Technol.* **2018**, *17*, e00074. [[CrossRef](#)]
124. Peñafiel-Vicuña, S.; Rendón-Enríquez, I.; Vega-Poot, A.; López-Téllez, G.; Palma-Cando, A.; Frontana-Urbe, B.A. Recovering Indium Tin Oxide Electrodes for the Fabrication of Hematite Photoelectrodes. *J. Electrochem. Soc.* **2020**, *167*, 126512. [[CrossRef](#)]
125. Chen, S.; Dai, Y.; Zhao, D.; Zhang, H. ITO-free flexible organic photovoltaics with multilayer MoO₃ /LiF/MoO₃ /Ag/MoO₃ as the transparent electrode. *Semicond. Sci. Technol.* **2016**, *31*, 055013. [[CrossRef](#)]
126. Lee, H.-M.; Kim, S.-S.; Kim, H.-K. Artificially MoO₃ graded ITO anodes for acidic buffer layer free organic photovoltaics. *Appl. Surf. Sci.* **2016**, *364*, 340–348. [[CrossRef](#)]
127. Sun, J.; Zheng, Q.; Cheng, S.; Zhou, H.; Lai, Y.; Yu, J. Comparing molybdenum oxide thin films prepared by magnetron sputtering and thermal evaporation applied in organic solar cells. *J. Mater. Sci. Mater. Electron.* **2016**, *27*, 3245–3249. [[CrossRef](#)]
128. Chaturvedi, N.; Swami, S.K.; Dutta, V. Electric field assisted spray deposited MoO₃ thin films as a hole transport layer for organic solar cells. *Sol. Energy* **2016**, *137*, 379–384. [[CrossRef](#)]
129. Dong, W.J.; Ham, J.; Jung, G.H.; Son, J.H.; Lee, J.-L. Ultrafast laser-assisted synthesis of hydrogenated molybdenum oxides for flexible organic solar cells. *J. Mater. Chem. A* **2016**, *4*, 4755–4762. [[CrossRef](#)]
130. Meyer, J.; Hamwi, S.; Bülow, T.; Johannes, H.-H.; Riedl, T.; Kowalsky, W. Highly efficient simplified organic light emitting diodes. *Appl. Phys. Lett.* **2007**, *91*, 113506. [[CrossRef](#)]
131. Tao, C.; Ruan, S.; Xie, G.; Kong, X.; Shen, L.; Meng, F.; Liu, C.; Zhang, X.; Dong, W.; Chen, W. Role of tungsten oxide in inverted polymer solar cells. *Appl. Phys. Lett.* **2009**, *94*, 043311. [[CrossRef](#)]
132. Miyake, K.; Kaneko, H.; Sano, M.; Suedomi, N. Physical and electrochromic properties of the amorphous and crystalline tungsten oxide thick films prepared under reducing atmosphere. *J. Appl. Phys.* **1984**, *55*, 2747–2753. [[CrossRef](#)]
133. Vida, G.; Josepovits, V.K.; Győr, M.; Deák, P. Characterization of Tungsten Surfaces by Simultaneous Work Function and Secondary Electron Emission Measurements. *Microsc. Microanal.* **2003**, *9*, 337–342. [[CrossRef](#)] [[PubMed](#)]
134. Stubhan, T.; Li, N.; Luechinger, N.A.; Halim, S.C.; Matt, G.J.; Brabec, C.J. High Fill Factor Polymer Solar Cells Incorporating a Low Temperature Solution Processed WO₃ Hole Extraction Layer. *Adv. Energy Mater.* **2012**, *2*, 1433–1438. [[CrossRef](#)]
135. Brabec, C.J. Organic photovoltaics: Technology and market. *Sol. Energy Mater. Sol. Cells* **2004**, *83*, 273–292. [[CrossRef](#)]
136. Lee, Y.H.; Abdu, H.A.E.; Kim, D.H.; Kim, T.W. Enhancement of the power conversion efficiency of organic photovoltaic cells due to Au@SiO₂ core shell nanoparticles embedded into a WO₃ hole transport layer. *Org. Electron.* **2019**, *68*, 182–186. [[CrossRef](#)]
137. Li, X.; Choy, W.C.H.; Ren, X.; Xin, J.; Lin, P.; Leung, D.C.W. Polarization-independent efficiency enhancement of organic solar cells by using 3-dimensional plasmonic electrode. *Appl. Phys. Lett.* **2013**, *102*, 153304. [[CrossRef](#)]
138. Li, X.; Choy, W.C.H.; Huo, L.; Xie, F.; Sha, W.E.I.; Ding, B.; Guo, X.; Li, Y.; Hou, J.; You, J.; et al. Dual Plasmonic Nanostructures for High Performance Inverted Organic Solar Cells. *Adv. Mater.* **2012**, *24*, 3046–3052. [[CrossRef](#)]
139. Li, X.H.; Sha, W.E.I.; Choy, W.C.H.; Fung, D.D.S.; Xie, F.X. Efficient Inverted Polymer Solar Cells with Directly Patterned Active Layer and Silver Back Grating. *J. Phys. Chem. C* **2012**, *116*, 7200–7206. [[CrossRef](#)]
140. Lee, Y.H.; Kim, D.H.; Kim, T.W. Enhanced power conversion efficiency of organic photovoltaic devices due to the surface plasmonic resonance effect generated utilizing Au-WO₃ nanocomposites. *Org. Electron.* **2017**, *45*, 256–262. [[CrossRef](#)]
141. Shen, W.; Tang, J.; Wang, D.; Yang, R.; Chen, W.; Bao, X.; Wang, Y.; Jiao, J.; Wang, Y.; Huang, Z.; et al. Enhanced efficiency of polymer solar cells by structure-differentiated silver nano-dopants in solution-processed tungsten oxide layer. *Mater. Sci. Eng. B* **2016**, *206*, 61–68. [[CrossRef](#)]
142. Wang, C.C.D.; Choy, W.C.H.; Duan, C.; Fung, D.D.S.; Sha, W.E.I.; Xie, F.-X.; Huang, F.; Cao, Y. Optical and electrical effects of gold nanoparticles in the active layer of polymer solar cells. *J. Mater. Chem.* **2012**, *22*, 1206–1211. [[CrossRef](#)]
143. Zhang, D.; Choy, W.C.H.; Xie, F.; Sha, W.E.I.; Li, X.; Ding, B.; Zhang, K.; Huang, F.; Cao, Y. Plasmonic Electrically Functionalized TiO₂ for High-Performance Organic Solar Cells. *Adv. Funct. Mater.* **2013**, *23*, 4255–4261. [[CrossRef](#)]
144. Li, X.; Choy, W.C.H.; Xie, F.; Zhang, S.; Hou, J. Room-temperature solution-processed molybdenum oxide as a hole transport layer with Ag nanoparticles for highly efficient inverted organic solar cells. *J. Mater. Chem. A* **2013**, *1*, 6614. [[CrossRef](#)]
145. Xie, F.; Choy, W.C.H.; Sha, W.E.I.; Zhang, D.; Zhang, S.; Li, X.; Leung, C.; Hou, J. Enhanced charge extraction in organic solar cells through electron accumulation effects induced by metal nanoparticles. *Energy Environ. Sci.* **2013**, *6*, 3372. [[CrossRef](#)]
146. Ren, X.; Cheng, J.; Zhang, S.; Li, X.; Rao, T.; Huo, L.; Hou, J.; Choy, W.C.H. High Efficiency Organic Solar Cells Achieved by the Simultaneous Plasmon-Optical and Plasmon-Electrical Effects from Plasmonic Asymmetric Modes of Gold Nanostars. *Small* **2016**, *12*, 5200–5207. [[CrossRef](#)] [[PubMed](#)]
147. Sha, W.E.I.; Zhu, H.L.; Chen, L.; Chew, W.C.; Choy, W.C.H. A General Design Rule to Manipulate Photocarrier Transport Path in Solar Cells and Its Realization by the Plasmonic-Electrical Effect. *Sci. Rep.* **2015**, *5*, 8525. [[CrossRef](#)] [[PubMed](#)]
148. Sha, W.E.I.; Li, X.; Choy, W.C.H. Breaking the Space Charge Limit in Organic Solar Cells by a Novel Plasmonic-Electrical Concept. *Sci. Rep.* **2015**, *4*, 6236. [[CrossRef](#)]
149. Li, X.; Choy, W.C.H.; Lu, H.; Sha, W.E.I.; Ho, A.H.P. Efficiency Enhancement of Organic Solar Cells by Using Shape-Dependent Broadband Plasmonic Absorption in Metallic Nanoparticles. *Adv. Funct. Mater.* **2013**, *23*, 2728–2735. [[CrossRef](#)]
150. Remya, R.; Gayathri, P.T.G.; Deb, B. Studies on solution-processed tungsten oxide nanostructures for efficient hole transport in the inverted polymer solar cells. *Mater. Chem. Phys.* **2020**, *255*, 123584. [[CrossRef](#)]
151. Liao, H.-H.; Chen, L.-M.; Xu, Z.; Li, G.; Yang, Y. Highly efficient inverted polymer solar cell by low temperature annealing of Cs₂CO₃ interlayer. *Appl. Phys. Lett.* **2008**, *92*, 173303. [[CrossRef](#)]

152. Huang, J.-S.; Chou, C.-Y.; Liu, M.-Y.; Tsai, K.-H.; Lin, W.-H.; Lin, C.-F. Solution-processed vanadium oxide as an anode interlayer for inverted polymer solar cells hybridized with ZnO nanorods. *Org. Electron.* **2009**, *10*, 1060–1065. [[CrossRef](#)]
153. Meyer, J.; Zilberberg, K.; Riedl, T.; Kahn, A. Electronic structure of Vanadium pentoxide: An efficient hole injector for organic electronic materials. *J. Appl. Phys.* **2011**, *110*, 033710. [[CrossRef](#)]
154. Xu, M.-F.; Xu, T.; Wang, C.-N.; Zhai, Z.-C.; Jin, Y.-L.; Yang, X.-H. Low-temperature, aqueous solution-processed V₂O₅ as the hole-transport layer for high performance organic solar cells. *J. Mater. Sci. Mater. Electron.* **2018**, *29*, 14783–14787. [[CrossRef](#)]
155. Jiang, Y.; Xiao, S.; Xu, B.; Zhan, C.; Mai, L.; Lu, X.; You, W. Enhancement of Photovoltaic Performance by Utilizing Readily Accessible Hole Transporting Layer of Vanadium(V) Oxide Hydrate in a Polymer-Fullerene Blend Solar Cell. *ACS Appl. Mater. Interfaces* **2016**, *8*, 11658–11666. [[CrossRef](#)] [[PubMed](#)]
156. Cong, H.; Han, D.; Sun, B.; Zhou, D.; Wang, C.; Liu, P.; Feng, L. Facile Approach to Preparing a Vanadium Oxide Hydrate Layer as a Hole-Transport Layer for High-Performance Polymer Solar Cells. *ACS Appl. Mater. Interfaces* **2017**, *9*, 18087–18094. [[CrossRef](#)]
157. Xie, F.; Choy, W.C.H.; Wang, C.; Li, X.; Zhang, S.; Hou, J. Low-Temperature Solution-Processed Hydrogen Molybdenum and Vanadium Bronzes for an Efficient Hole-Transport Layer in Organic Electronics. *Adv. Mater.* **2013**, *25*, 2051–2055. [[CrossRef](#)]
158. Vishnumurthy, K.A.; Kesavan, A.V.; Swathi, S.K.; Ramamurthy, P.C. Low band gap thienothiophene-diketopyrrolopyrrole copolymers with V₂O₅ as hole transport layer for photovoltaic application. *Opt. Mater.* **2020**, *109*, 110303. [[CrossRef](#)]
159. Ravi, R.; Deb, B. Studies on One-Step-Synthesized Hydrated Vanadium Pentoxide for Efficient Hole Transport in Organic Photovoltaics. *Energy Technol.* **2020**, *8*, 1901323. [[CrossRef](#)]
160. Xu, W.; Liu, Y.; Huang, X.; Jiang, L.; Li, Q.; Hu, X.; Huang, F.; Gong, X.; Cao, Y. Solution-processed VO_x prepared using a novel synthetic method as the hole extraction layer for polymer solar cells. *J. Mater. Chem. C* **2016**, *4*, 1953–1958. [[CrossRef](#)]
161. Shafeeq, K.M.; Athira, V.P.; Kishor, C.H.R.; Aneesh, P.M. Structural and optical properties of V₂O₅ nanostructures grown by thermal decomposition technique. *Appl. Phys. A* **2020**, *126*, 586. [[CrossRef](#)]
162. Alsulami, A.; Griffin, J.; Alqurashi, R.; Yi, H.; Iraqi, A.; Lidzey, D.; Buckley, A. Thermally Stable Solution Processed Vanadium Oxide as a Hole Extraction Layer in Organic Solar Cells. *Materials* **2016**, *9*, 235. [[CrossRef](#)] [[PubMed](#)]
163. Zafar, M.; Yun, J.-Y.; Kim, D.-H. Highly stable inverted organic photovoltaic cells with a V₂O₅ hole transport layer. *Korean J. Chem. Eng.* **2017**, *34*, 1504–1508. [[CrossRef](#)]
164. Teng, N.-W.; Li, C.-H.; Lo, W.-C.; Tsai, Y.-S.; Liao, C.-Y.; You, Y.-W.; Ho, H.-L.; Li, W.-L.; Lee, C.-C.; Lin, W.-C.; et al. Highly Efficient Nonfullerene Organic Photovoltaic Devices with 10% Power Conversion Efficiency Enabled by a Fine-Tuned and Solution-Processed Hole-Transporting Layer. *Sol. RRL* **2020**, *4*, 2000223. [[CrossRef](#)]
165. Xia, C.; Hong, W.T.; Kim, Y.E.; Choe, W.-S.; Kim, D.-H.; Kim, J.K. Metal-Organic Decomposition-Mediated Nanoparticulate Vanadium Oxide Hole Transporting Buffer Layer for Polymer Bulk-Heterojunction Solar Cells. *Polymers* **2020**, *12*, 1791. [[CrossRef](#)] [[PubMed](#)]
166. Beliatas, M.J.; Helgesen, M.; García-Valverde, R.; Corazza, M.; Roth, B.; Carlé, J.E.; Jørgensen, M.; Krebs, F.C.; Gevorgyan, S.A. Slot-Die-Coated V₂O₅ as Hole Transport Layer for Flexible Organic Solar Cells and Optoelectronic Devices. *Adv. Eng. Mater.* **2016**, *18*, 1494–1503. [[CrossRef](#)]
167. Arbab, E.A.A.; Mola, G.T. V₂O₅ thin film deposition for application in organic solar cells. *Appl. Phys. A Mater. Sci. Process.* **2016**, *122*, 405. [[CrossRef](#)]
168. Kavuri, H.A.; Fukuda, T.; Takahira, K.; Takahashi, A.; Kihara, S.; McGillivray, D.J.; Willmott, G. Electro spray-deposited vanadium oxide anode interlayers for high-efficiency organic solar cells. *Org. Electron.* **2018**, *57*, 239–246. [[CrossRef](#)]
169. Lee, D.-Y.; Cho, S.-P.; Na, S.-I.; Kim, S.-S. ITO-free polymer solar cells with vanadium oxide hole transport layer. *J. Ind. Eng. Chem.* **2017**, *45*, 1–4. [[CrossRef](#)]
170. Ko, E.-H.; Kim, H.-K. Highly transparent vanadium oxide-graded indium zinc oxide electrodes for flexible organic solar cells. *Thin Solid Films* **2016**, *601*, 2–6. [[CrossRef](#)]
171. Ai, L.; Fang, G.; Yuan, L.; Liu, N.; Wang, M.; Li, C.; Zhang, Q.; Li, J.; Zhao, X. Influence of substrate temperature on electrical and optical properties of p-type semitransparent conductive nickel oxide thin films deposited by radio frequency sputtering. *Appl. Surf. Sci.* **2008**, *254*, 2401–2405. [[CrossRef](#)]
172. Zhang, H.; Cheng, J.; Lin, F.; He, H.; Mao, J.; Wong, K.S.; Jen, A.K.Y.; Choy, W.C.H. Pinhole-Free and Surface-Nanostructured NiO_x Film by Room-Temperature Solution Process for High-Performance Flexible Perovskite Solar Cells with Good Stability and Reproducibility. *ACS Nano* **2016**, *10*, 1503–1511. [[CrossRef](#)]
173. Manders, J.R.; Tsang, S.-W.; Hartel, M.J.; Lai, T.-H.; Chen, S.; Amb, C.M.; Reynolds, J.R.; So, F. Solution-Processed Nickel Oxide Hole Transport Layers in High Efficiency Polymer Photovoltaic Cells. *Adv. Funct. Mater.* **2013**, *23*, 2993–3001. [[CrossRef](#)]
174. Parthiban, S.; Kim, S.; Tamilavan, V.; Lee, J.; Shin, I.; Yuvaraj, D.; Jung, Y.K.; Hyun, M.H.; Jeong, J.H.; Park, S.H. Enhanced efficiency and stability of polymer solar cells using solution-processed nickel oxide as hole transport material. *Curr. Appl. Phys.* **2017**, *17*, 1232–1237. [[CrossRef](#)]
175. Chavhan, S.D.; Hansson, R.; Ericsson, L.K.E.; Beyer, P.; Hofmann, A.; Brütting, W.; Opitz, A.; Moons, E. Low temperature processed NiO_x hole transport layers for efficient polymer solar cells. *Org. Electron.* **2017**, *44*, 59–66. [[CrossRef](#)]
176. Jiang, F.; Choy, W.C.H.; Li, X.; Zhang, D.; Cheng, J. Post-treatment-Free Solution-Processed Non-stoichiometric NiO_x Nanoparticles for Efficient Hole-Transport Layers of Organic Optoelectronic Devices. *Adv. Mater.* **2015**, *27*, 2930–2937. [[CrossRef](#)] [[PubMed](#)]

177. Huang, Z.; Ouyang, D.; Ma, R.; Wu, W.; Roy, V.A.L.; Choy, W.C.H. A General Method: Designing a Hypocrystalline Hydroxide Intermediate to Achieve Ultrasmall and Well-Dispersed Ternary Metal Oxide for Efficient Photovoltaic Devices. *Adv. Funct. Mater.* **2019**, *29*, 1904684. [[CrossRef](#)]
178. Kim, J.K. PEG-assisted Sol-gel Synthesis of Compact Nickel Oxide Hole-Selective Layer with Modified Interfacial Properties for Organic Solar Cells. *Polymers* **2019**, *11*, 120. [[CrossRef](#)]
179. Rho, Y.; Kang, K.-T.; Lee, D. Highly crystalline Ni/NiO hybrid electrodes processed by inkjet printing and laser-induced reductive sintering under ambient conditions. *Nanoscale* **2016**, *8*, 8976–8985. [[CrossRef](#)]
180. Singh, A.; Gupta, S.K.; Garg, A. Inkjet printing of NiO films and integration as hole transporting layers in polymer solar cells. *Sci. Rep.* **2017**, *7*. [[CrossRef](#)]
181. Huang, S.; Wang, Y.; Shen, S.; Tang, Y.; Yu, A.; Kang, B.; Silva, S.R.P.; Lu, G. Enhancing the performance of polymer solar cells using solution-processed copper doped nickel oxide nanoparticles as hole transport layer. *J. Colloid Interface Sci.* **2019**, *535*, 308–317. [[CrossRef](#)]
182. Ouyang, D.; Zheng, J.; Huang, Z.; Zhu, L.; Choy, W.C.H. An efficacious multifunction codoping strategy on a room-temperature solution-processed hole transport layer for realizing high-performance perovskite solar cells. *J. Mater. Chem. A* **2021**, *9*, 371–379. [[CrossRef](#)]
183. Al-Jawhari, H.A.; Caraveo-Frescas, J.A.; Hedhili, M.N.; Alshareef, H.N. P-Type Cu₂O/SnO Bilayer Thin Film Transistors Processed at Low Temperatures. *ACS Appl. Mater. Interfaces* **2013**, *5*, 9615–9619. [[CrossRef](#)] [[PubMed](#)]
184. Murali, D.S.; Kumar, S.; Choudhary, R.J.; Wadikar, A.D.; Jain, M.K.; Subrahmanyam, A. Synthesis of Cu₂O from CuO thin films: Optical and electrical properties. *AIP Adv.* **2015**, *5*, 047143. [[CrossRef](#)]
185. Fortunato, E.; Figueiredo, V.; Barquinha, P.; Elamurugu, E.; Barros, R.; Gonçalves, G.; Park, S.-H.K.; Hwang, C.-S.; Martins, R. Thin-film transistors based on p-type Cu₂O thin films produced at room temperature. *Appl. Phys. Lett.* **2010**, *96*, 192102. [[CrossRef](#)]
186. Zuo, C.; Ding, L. Solution-Processed Cu₂O and CuO as Hole Transport Materials for Efficient Perovskite Solar Cells. *Small* **2015**, *11*, 5528–5532. [[CrossRef](#)]
187. Yu, Z.; Liu, W.; Fu, W.; Zhang, Z.; Yang, W.; Wang, S.; Li, H.; Xu, M.; Chen, H. An aqueous solution-processed CuO X film as an anode buffer layer for efficient and stable organic solar cells. *J. Mater. Chem. A* **2016**, *4*, 5130–5136. [[CrossRef](#)]
188. Yu, R.-S.; Tasi, C.-P. Structure, composition and properties of p-type CuCrO₂ thin films. *Ceram. Int.* **2014**, *40*, 8211–8217. [[CrossRef](#)]
189. Han, M.; Jiang, K.; Zhang, J.; Yu, W.; Li, Y.; Hu, Z.; Chu, J. Structural, electronic band transition and optoelectronic properties of delafossite CuGa_{1-x}Cr_xO₂ (0 ≤ x ≤ 1) solid solution films grown by the sol-gel method. *J. Mater. Chem.* **2012**, *22*, 18463. [[CrossRef](#)]
190. Xiong, D.; Xu, Z.; Zeng, X.; Zhang, W.; Chen, W.; Xu, X.; Wang, M.; Cheng, Y.-B. Hydrothermal synthesis of ultrasmall CuCrO₂ nanocrystal alternatives to NiO nanoparticles in efficient p-type dye-sensitized solar cells. *J. Mater. Chem.* **2012**, *22*, 24760. [[CrossRef](#)]
191. Marquardt, M.A.; Ashmore, N.A.; Cann, D.P. Crystal chemistry and electrical properties of the delafossite structure. *Thin Solid Films* **2006**, *496*, 146–156. [[CrossRef](#)]
192. Yang, B.; Ouyang, D.; Huang, Z.; Ren, X.; Zhang, H.; Choy, W.C.H. Multifunctional Synthesis Approach of In:CuCrO₂ Nanoparticles for Hole Transport Layer in High-Performance Perovskite Solar Cells. *Adv. Funct. Mater.* **2019**, *29*, 1902600. [[CrossRef](#)]
193. Wang, J.; Lee, Y.-J.; Hsu, J.W.P. Sub-10 nm copper chromium oxide nanocrystals as a solution processed p-type hole transport layer for organic photovoltaics. *J. Mater. Chem. C* **2016**, *4*, 3607–3613. [[CrossRef](#)]
194. Wang, J.; Daunis, T.B.; Cheng, L.; Zhang, B.; Kim, J.; Hsu, J.W.P. Combustion Synthesis of p-Type Transparent Conducting CuCrO_{2+x} and Cu:CrO_x Thin Films at 180 °C. *ACS Appl. Mater. Interfaces* **2018**, *10*, 3732–3738. [[CrossRef](#)] [[PubMed](#)]
195. Wahl, T.; Zellmer, S.; Hanisch, J.; Garnweitner, G.; Ahlswede, E. Thin indium tin oxide nanoparticle films as hole transport layer in inverted organic solar cells. *Thin Solid Films* **2016**, *616*, 419–424. [[CrossRef](#)]
196. Bhargav, R.; Gairola, S.P.; Patra, A.; Naqvi, S.; Dhawan, S.K. Improved performance of organic solar cells with solution processed hole transport layer. *Opt. Mater.* **2018**, *80*, 138–142. [[CrossRef](#)]
197. Kan, M.; Wang, J.Y.; Li, X.W.; Zhang, S.H.; Li, Y.W.; Kawazoe, Y.; Sun, Q.; Jena, P. Structures and Phase Transition of a MoS₂ Monolayer. *J. Phys. Chem. C* **2014**, *118*, 1515–1522. [[CrossRef](#)]
198. Barrera, D.; Jawaid, A.; Daunis, T.B.; Cheng, L.; Wang, Q.; Lee, Y.-J.; Kim, M.J.; Kim, J.; Vaia, R.A.; Hsu, J.W.P. Inverted OPVs with MoS₂ hole transport layer deposited by spray coating. *Mater. Today Energy* **2017**, *5*, 107–111. [[CrossRef](#)]
199. Martinez-Rojas, F.; Hsein, M.; El Jouad, Z.; Armijo, F.; Cattin, L.; Louarn, G.; Stephant, N.; del Valle, M.A.; Addou, M.; Soto, J.P.; et al. Mo(S_xO_y) thin films deposited by electrochemistry for application in organic photovoltaic cells. *Mater. Chem. Phys.* **2017**, *201*, 331–338. [[CrossRef](#)]
200. Xing, W.; Chen, Y.; Wang, X.; Lv, L.; Ouyang, X.; Ge, Z.; Huang, H. MoS₂ Quantum Dots with a Tunable Work Function for High-Performance Organic Solar Cells. *ACS Appl. Mater. Interfaces* **2016**, *8*, 26916–26923. [[CrossRef](#)]
201. Wei, J.; Yin, Z.; Chen, S.-C.; Cai, D.; Zheng, Q. Solution-processed MoS_x thin-films as hole-transport layers for efficient polymer solar cells. *RSC Adv.* **2016**, *6*, 39137–39143. [[CrossRef](#)]
202. Adilbekova, B.; Lin, Y.; Yengel, E.; Faber, H.; Harrison, G.; Firdaus, Y.; El-Labban, A.; Anjum, D.H.; Tung, V.; Anthopoulos, T.D. Liquid phase exfoliation of MoS₂ and WS₂ in aqueous ammonia and their application in highly efficient organic solar cells. *J. Mater. Chem. C* **2020**, *8*, 5259–5264. [[CrossRef](#)]

203. Lin, Y.; Adilbekova, B.; Firdaus, Y.; Yengel, E.; Faber, H.; Sajjad, M.; Zheng, X.; Yarali, E.; Seitkhan, A.; Bakr, O.M.; et al. 17% Efficient Organic Solar Cells Based on Liquid Exfoliated WS₂ as a Replacement for PEDOT:PSS. *Adv. Mater.* **2019**, *31*, 1902965. [[CrossRef](#)] [[PubMed](#)]
204. Ram, K.S.; Singh, J. Over 20% Efficient and Stable Non-Fullerene-Based Ternary Bulk-Heterojunction Organic Solar Cell with WS₂ Hole-Transport Layer and Graded Refractive Index Antireflection Coating. *Adv. Theory Simul.* **2020**, *3*, 2000047. [[CrossRef](#)]
205. Hilal, M.; Han, J.I. Preparation of hierarchical flower-like nickel sulfide as hole transporting material for organic solar cells via a one-step solvothermal method. *Sol. Energy* **2019**, *188*, 403–413. [[CrossRef](#)]
206. Bhargav, R.; Patra, A.; Dhawan, S.K.; Gairola, S.P. Solution processed hole transport layer towards efficient and cost effective organic solar cells. *Sol. Energy* **2018**, *165*, 131–135. [[CrossRef](#)]
207. Jose, E.; Mohan, M.; Namboothiry, M.A.G.; Kumar, M.C.S. Room temperature deposition of high figure of merit p-type transparent conducting Cu–Zn–S thin films and their application in organic solar cells as an efficient hole transport layer. *J. Alloys Compd.* **2020**, *829*, 154507. [[CrossRef](#)]
208. Wang, Z.; Gao, L.; Wei, X.; Zhao, M.; Miao, Y.; Zhang, X.; Zhang, H.; Wang, H.; Hao, Y.; Xu, B.; et al. Energy level engineering of PEDOT:PSS by antimonene quantum sheet doping for highly efficient OLEDs. *J. Mater. Chem. C* **2020**, *8*, 1796–1802. [[CrossRef](#)]
209. Wang, Z.; Wang, Z.; Wang, Z.; Zhao, M.; Zhou, Y.; Zhao, B.; Miao, Y.; Liu, P.; Hao, Y.; Wang, H.; et al. Novel 2D material from AMQS-based defect engineering for efficient and stable organic solar cells. *2D Mater.* **2019**, *6*, 045017. [[CrossRef](#)]
210. Gao, Z.; Wang, Y.; Ouyang, D.; Liu, H.; Huang, Z.; Kim, J.; Choy, W.C.H. Triple Interface Passivation Strategy-Enabled Efficient and Stable Inverted Perovskite Solar Cells. *Small Methods* **2020**, *4*, 2000478. [[CrossRef](#)]
211. Ma, R.; Ren, Z.; Li, C.; Wang, Y.; Huang, Z.; Zhao, Y.; Yang, T.; Liang, Y.; Sun, X.W.; Choy, W.C.H. Establishing Multifunctional Interface Layer of Perovskite Ligand Modified Lead Sulfide Quantum Dots for Improving the Performance and Stability of Perovskite Solar Cells. *Small* **2020**, *16*, 2002628. [[CrossRef](#)]
212. Ma, R.; Zheng, J.; Tian, Y.; Li, C.; Lyu, B.; Lu, L.; Su, Z.; Chen, L.; Gao, X.; Tang, J.; et al. Self-Polymerization of Monomer and Induced Interactions with Perovskite for Highly Performed and Stable Perovskite Solar Cells. *Adv. Funct. Mater.* **2022**, *32*, 2105290. [[CrossRef](#)]
213. Wijeyasinghe, N.; Eisner, F.; Tsetseris, L.; Lin, Y.-H.; Seitkhan, A.; Li, J.; Yan, F.; Solomeshch, O.; Tessler, N.; Patsalas, P.; et al. p-Doping of Copper(I) Thiocyanate (CuSCN) Hole-Transport Layers for High-Performance Transistors and Organic Solar Cells. *Adv. Funct. Mater.* **2018**, *28*, 1802055. [[CrossRef](#)]
214. Wang, Z.; Dong, J.; Guo, J.; Wang, Z.; Yan, L.; Hao, Y.; Wang, H.; Xu, B.; Yin, S. Hybrid Hole Extraction Layer Enabled High Efficiency in Polymer Solar Cells. *ACS Appl. Mater. Interfaces* **2020**, *12*, 55342–55348. [[CrossRef](#)]
215. Worakajit, P.; Hamada, F.; Sahu, D.; Kidkhunthod, P.; Sudyoadsuk, T.; Promarak, V.; Harding, D.J.; Packwood, D.M.; Saeki, A.; Pattanasattayavong, P. Elucidating the Coordination of Diethyl Sulfide Molecules in Copper(I) Thiocyanate (CuSCN) Thin Films and Improving Hole Transport by Antisolvent Treatment. *Adv. Funct. Mater.* **2020**, *30*, 2002355. [[CrossRef](#)]
216. Suresh Kumar, M.; Mohanta, K.; Batabyal, S.K. Solution processed Cu₂CdSnS₄ as a low-cost inorganic hole transport material for polymer solar cells. *Sol. Energy Mater. Sol. Cells* **2017**, *161*, 157–161. [[CrossRef](#)]
217. Xu, Z. Fundamental Properties of Graphene. In *Graphene*; Elsevier: Amsterdam, The Netherlands, 2018; pp. 73–102.
218. Konkena, B.; Vasudevan, S. Understanding Aqueous Dispersibility of Graphene Oxide and Reduced Graphene Oxide through pK_a Measurements. *J. Phys. Chem. Lett.* **2012**, *3*, 867–872. [[CrossRef](#)] [[PubMed](#)]
219. Mattevi, C.; Eda, G.; Agnoli, S.; Miller, S.; Mkhoyan, K.A.; Celik, O.; Mastrogiovanni, D.; Granozzi, G.; Garfunkel, E.; Chhowalla, M. Evolution of Electrical, Chemical, and Structural Properties of Transparent and Conducting Chemically Derived Graphene Thin Films. *Adv. Funct. Mater.* **2009**, *19*, 2577–2583. [[CrossRef](#)]
220. Sun, L. Structure and synthesis of graphene oxide. *Chin. J. Chem. Eng.* **2019**, *27*, 2251–2260. [[CrossRef](#)]
221. Rafique, S.; Abdullah, S.M.; Alhummiyany, H.; Abdel-wahab, M.S.; Iqbal, J.; Sulaiman, K. Bulk Heterojunction Organic Solar Cells with Graphene Oxide Hole Transport Layer: Effect of Varied Concentration on Photovoltaic Performance. *J. Phys. Chem. C* **2017**, *121*, 140–146. [[CrossRef](#)]
222. Allen, M.J.; Tung, V.C.; Kaner, R.B. Honeycomb Carbon: A Review of Graphene. *Chem. Rev.* **2010**, *110*, 132–145. [[CrossRef](#)]
223. Huang, X.; Yu, H.; Wu, Z.; Li, Y. Improving the performance of polymer solar cells by efficient optimizing the hole transport layer-graphene oxide. *J. Solid-State Electrochem.* **2018**, *22*, 317–329. [[CrossRef](#)]
224. Lee, S.; Yeo, J.-S.; Yun, J.-M.; Kim, D.-Y. Water dispersion of reduced graphene oxide stabilized via fullereneol semiconductor for organic solar cells. *Opt. Mater. Express* **2017**, *7*, 2487. [[CrossRef](#)]
225. Kwon, S.-N.; Jung, C.-H.; Na, S.-I. Electron-beam-induced reduced graphene oxide as an alternative hole-transporting interfacial layer for high-performance and reliable polymer solar cells. *Org. Electron.* **2016**, *34*, 67–74. [[CrossRef](#)]
226. Fakharan, Z.; Naji, L.; Madanipour, K. Nd:YAG pulsed laser production of reduced-graphene oxide as hole transporting layer in polymer solar cells and the influences of solvent type. *Org. Electron.* **2020**, *76*, 105459. [[CrossRef](#)]
227. Dericiler, K.; Alishah, H.M.; Bozar, S.; Güneş, S.; Kaya, F. A novel method for graphene synthesis via electrochemical process and its utilization in organic photovoltaic devices. *Appl. Phys. A* **2020**, *126*, 904. [[CrossRef](#)]
228. Xia, Y.; Pan, Y.; Zhang, H.; Qiu, J.; Zheng, Y.; Chen, Y.; Huang, W. Graphene Oxide by UV-Ozone Treatment as an Efficient Hole Extraction Layer for Highly Efficient and Stable Polymer Solar Cells. *ACS Appl. Mater. Interfaces* **2017**, *9*, 26252–26256. [[CrossRef](#)]
229. Rafique, S.; Abdullah, S.M.; Iqbal, J.; Jilani, A.; Vattamkandathil, S.; Iwamoto, M. Moderately reduced graphene oxide via UV-ozone treatment as hole transport layer for high efficiency organic solar cells. *Org. Electron.* **2018**, *59*, 140–148. [[CrossRef](#)]

230. Zhao, F.-G.; Hu, C.-M.; Kong, Y.-T.; Pan, B.; Yao, X.; Chu, J.; Xu, Z.-W.; Zuo, B.; Li, W.-S. Sulfanilic Acid Pending on a Graphene Scaffold: Novel, Efficient Synthesis and Much Enhanced Polymer Solar Cell Efficiency and Stability Using It as a Hole Extraction Layer. *ACS Appl. Mater. Interfaces* **2018**, *10*, 24679–24688. [[CrossRef](#)]
231. Ali, A.; Khan, Z.S.; Jamil, M.; Khan, Y.; Ahmad, N.; Ahmed, S. Simultaneous reduction and sulfonation of graphene oxide for efficient hole selectivity in polymer solar cells. *Curr. Appl. Phys.* **2018**, *18*, 599–610. [[CrossRef](#)]
232. Chen, X.; Liu, Q.; Zhang, M.; Ju, H.; Zhu, J.; Qiao, Q.; Wang, M.; Yang, S. Noncovalent phosphorylation of graphene oxide with improved hole transport in high-efficiency polymer solar cells. *Nanoscale* **2018**, *10*, 14840–14846. [[CrossRef](#)]
233. Cheng, X.; Long, J.; Wu, R.; Huang, L.; Tan, L.; Chen, L.; Chen, Y. Fluorinated Reduced Graphene Oxide as an Efficient Hole-Transport Layer for Efficient and Stable Polymer Solar Cells. *ACS Omega* **2017**, *2*, 2010–2016. [[CrossRef](#)] [[PubMed](#)]
234. Nicasio-Collazo, J.; Maldonado, J.-L.; Salinas-Cruz, J.; Barreiro-Argüelles, D.; Caballero-Quintana, I.; Vázquez-Espinosa, C.; Romero-Borja, D. Functionalized and reduced graphene oxide as hole transport layer and for use in ternary organic solar cell. *Opt. Mater.* **2019**, *98*, 109434. [[CrossRef](#)]
235. Park, J.-J.; Heo, Y.-J.; Yun, J.-M.; Kim, Y.; Yoon, S.C.; Lee, S.-H.; Kim, D.-Y. Orthogonal Printable Reduced Graphene Oxide 2D Materials as Hole Transport Layers for High-Performance Inverted Polymer Solar Cells: Sheet Size Effect on Photovoltaic Properties. *ACS Appl. Mater. Interfaces* **2020**, *12*, 42811–42820. [[CrossRef](#)] [[PubMed](#)]
236. Zheng, X.; Zhang, H.; Yang, Q.; Xiong, C.; Li, W.; Yan, Y.; Gurney, R.S.; Wang, T. Solution-processed Graphene-MoS₂ heterostructure for efficient hole extraction in organic solar cells. *Carbon* **2019**, *142*, 156–163. [[CrossRef](#)]
237. Shoyiga, H.O.; Martincigh, B.S.; Nyamori, V.O. Hydrothermal synthesis of reduced graphene oxide-anatase titania nanocomposites for dual application in organic solar cells. *Int. J. Energy Res.* **2020**, *45*, 7293–7314. [[CrossRef](#)]
238. Lee, J.H.; Yoon, S.; Ko, M.S.; Lee, N.; Hwang, I.; Lee, M.J. Improved performance of organic photovoltaic devices by doping F₄TCNQ onto solution-processed graphene as a hole transport layer. *Org. Electron.* **2016**, *30*, 302–311. [[CrossRef](#)]
239. Lee, C.K.; Seo, J.G.; Kim, H.J.; Hong, S.J.; Song, G.; Ahn, C.; Lee, D.J.; Song, S.H. Versatile and Tunable Electrical Properties of Doped Nonoxidized Graphene Using Alkali Metal Chlorides. *ACS Appl. Mater. Interfaces* **2019**, *11*, 42520–42527. [[CrossRef](#)]
240. Sun, B.; Zhou, D.; Wang, C.; Liu, P.; Hao, Y.; Han, D.; Feng, L.; Zhou, Y. Copper(II) chloride doped graphene oxides as efficient hole transport layer for high-performance polymer solar cells. *Org. Electron.* **2017**, *44*, 176–182. [[CrossRef](#)]
241. Capasso, A.; Salamandra, L.; Faggio, G.; Dikonimos, T.; Buonocore, F.; Morandi, V.; Ortolani, L.; Lisi, N. Chemical Vapor Deposited Graphene-Based Derivative As High-Performance Hole Transport Material for Organic Photovoltaics. *ACS Appl. Mater. Interfaces* **2016**, *8*, 23844–23853. [[CrossRef](#)]
242. Sarkar, A.S.; Rao, A.D.; Jagdish, A.K.; Gupta, A.; Nandi, C.K.; Ramamurthy, P.C.; Pal, S.K. Facile embedding of gold nanostructures in the hole transporting layer for efficient polymer solar cells. *Org. Electron.* **2018**, *54*, 148–153. [[CrossRef](#)]
243. Iakobson, O.D.; Gribkova, O.L.; Tameev, A.R.; Nekrasov, A.A.; Saranin, D.S.; Di Carlo, A. Graphene nanosheet/polyaniline composite for transparent hole transporting layer. *J. Ind. Eng. Chem.* **2018**, *65*, 309–317. [[CrossRef](#)]
244. Aatif, M.; Patel, J.; Sharma, A.; Chauhan, M.; Kumar, G.; Pal, P.; Chand, S.; Tripathi, B.; Pandey, M.K.; Tiwari, J.P. Graphene oxide-molybdenum oxide composite with improved hole transport in bulk heterojunction solar cells. *AIP Adv.* **2019**, *9*, 075215. [[CrossRef](#)]
245. Cheng, J.; Zhang, H.; Zhao, Y.; Mao, J.; Li, C.; Zhang, S.; Wong, K.S.; Hou, J.; Choy, W.C.H. Self-Assembled Quasi-3D Nanocomposite: A Novel p-Type Hole Transport Layer for High Performance Inverted Organic Solar Cells. *Adv. Funct. Mater.* **2018**, *28*, 1706403. [[CrossRef](#)]
246. Dang, Y.; Wang, Y.; Shen, S.; Huang, S.; Qu, X.; Pang, Y.; Silva, S.R.P.; Kang, B.; Lu, G. Solution processed hybrid Graphene-MoO₃ hole transport layers for improved performance of organic solar cells. *Org. Electron.* **2019**, *67*, 95–100. [[CrossRef](#)]
247. Christopholi, L.P.; da Cunha, M.R.P.; Spada, E.R.; Gavim, A.E.X.; Hadano, F.S.; da Silva, W.J.; Rodrigues, P.C.; Macedo, A.G.; Faria, R.M.; de Deus, J.F. Reduced graphene oxide and perylene derivative nanohybrid as multifunctional interlayer for organic solar cells. *Synth. Met.* **2020**, *269*, 116552. [[CrossRef](#)]
248. Lu, J.; Yeo, P.S.E.; Gan, C.K.; Wu, P.; Loh, K.P. Transforming C60 molecules into graphene quantum dots. *Nat. Nanotechnol.* **2011**, *6*, 247–252. [[CrossRef](#)]
249. Peng, J.; Gao, W.; Gupta, B.K.; Liu, Z.; Romero-Aburto, R.; Ge, L.; Song, L.; Alemany, L.B.; Zhan, X.; Gao, G.; et al. Graphene Quantum Dots Derived from Carbon Fibers. *Nano Lett.* **2012**, *12*, 844–849. [[CrossRef](#)]
250. Ho, N.T.; Van Tam, T.; Tien, H.N.; Jang, S.-J.; Nguyen, T.K.; Choi, W.M.; Cho, S.; Kim, Y.S. Solution-Processed Transparent Intermediate Layer for Organic Tandem Solar Cell Using Nitrogen-Doped Graphene Quantum Dots. *J. Nanosci. Nanotechnol.* **2017**, *17*, 5686–5692. [[CrossRef](#)]
251. Hoang, T.T.; Pham, H.P.; Tran, Q.T. A Facile Microwave-Assisted Hydrothermal Synthesis of Graphene Quantum Dots for Organic Solar Cell Efficiency Improvement. *J. Nanomater.* **2020**, *2020*, 3207909. [[CrossRef](#)]
252. Zhang, X.; Sun, S.; Liu, X. Amino functionalized carbon nanotubes as hole transport layer for high performance polymer solar cells. *Inorg. Chem. Commun.* **2019**, *103*, 142–148. [[CrossRef](#)]
253. Rajanna, P.M.; Meddeb, H.; Sergeev, O.; Tsapenko, A.P.; Bereznev, S.; Vehse, M.; Volobujeva, O.; Danilson, M.; Lund, P.D.; Nasibulin, A.G. Rational design of highly efficient flexible and transparent p-type composite electrode based on single-walled carbon nanotubes. *Nano Energy* **2020**, *67*, 104183. [[CrossRef](#)]

254. Zhang, W.; Bu, F.; Shen, W.; Qi, X.; Yang, N.; Chen, M.; Yang, D.; Wang, Y.; Zhang, M.; Jiang, H.; et al. Strongly enhanced efficiency of polymer solar cells through unzipped SWNT hybridization in the hole transport layer. *RSC Adv.* **2020**, *10*, 24847–24854. [[CrossRef](#)]
255. Ibanez, J.G.; Rincón, M.E.; Gutierrez-Granados, S.; Chahma, M.; Jaramillo-Quintero, O.A.; Frontana-Urbe, B.A. Conducting Polymers in the Fields of Energy, Environmental Remediation, and Chemical-Chiral Sensors. *Chem. Rev.* **2018**, *118*, 4731–4816. [[CrossRef](#)] [[PubMed](#)]
256. Emah, J.B.; George, N.J.; Akpan, U.B. Interfacial Surface Modification via Nanoimprinting to Increase Open-Circuit Voltage of Organic Solar Cells. *J. Electron. Mater.* **2017**, *46*, 4989–4998. [[CrossRef](#)]
257. Fernández Castro, M.; Mazzolini, E.; Sondergaard, R.R.; Espindola-Rodriguez, M.; Andreasen, J.W. Flexible ITO-Free Roll-Processed Large-Area Nonfullerene Organic Solar Cells Based on P3HT:O-IDTBR. *Phys. Rev. Appl.* **2020**, *14*, 034067. [[CrossRef](#)]
258. Vohra, V.; Shimizu, S.; Takeoka, Y. Water-Processed Organic Solar Cells with Open-Circuit Voltages Exceeding 1.3V. *Coatings* **2020**, *10*, 421. [[CrossRef](#)]
259. Hong, N.; Xiao, J.; Li, Y.; Li, Y.; Wu, Y.; Yu, W.; Qiu, X.; Chen, R.; Yip, H.-L.; Huang, W.; et al. Unexpected fluorescent emission of graft sulfonated-acetone-formaldehyde lignin and its application as a dopant of PEDOT for high performance photovoltaic and light-emitting devices. *J. Mater. Chem. C* **2016**, *4*, 5297–5306. [[CrossRef](#)]
260. Abdel-Fattah, T.M.; Younes, E.M.; Namkoong, G.; El-Maghraby, E.M.; Elsayed, A.H.; Abo Elazm, A.H. Solvents effects on the hole transport layer in organic solar cells performance. *Sol. Energy* **2016**, *137*, 337–343. [[CrossRef](#)]
261. Kurukavak, Ç.K.; Polat, S. Influence of the volume of EGME-DMSO mixed co-solvent doping on the characteristics of PEDOT:PSS and their application in polymer solar cells. *Polym. Polym. Compos.* **2020**, *29*, 1222–1228. [[CrossRef](#)]
262. Yi, M.; Hong, S.; Kim, J.-R.; Kang, H.; Lee, J.; Yu, K.; Kee, S.; Lee, W.; Lee, K. Modification of a PEDOT:PSS hole transport layer for printed polymer solar cells. *Sol. Energy Mater. Sol. Cells* **2016**, *153*, 117–123. [[CrossRef](#)]
263. Howells, C.T.; Marbou, K.; Kim, H.; Lee, K.J.; Heinrich, B.; Kim, S.J.; Nakao, A.; Aoyama, T.; Furukawa, S.; Kim, J.-H.; et al. Enhanced organic solar cells efficiency through electronic and electro-optic effects resulting from charge transfers in polymer hole transport blends. *J. Mater. Chem. A* **2016**, *4*, 4252–4263. [[CrossRef](#)]
264. Bhargav, R.; Bhardwaj, D.; Shahjad, A.P.; Chand, S. Poly(Styrene Sulfonate) Free Poly(3,4-Ethylenedioxythiophene) as a Robust and Solution-Processable Hole Transport Layer for Organic Solar Cells. *ChemistrySelect* **2016**, *1*, 1347–1352. [[CrossRef](#)]
265. Cai, W.; Musumeci, C.; Ajjan, F.N.; Bao, Q.; Ma, Z.; Tang, Z.; Inganäs, O. Self-doped conjugated polyelectrolyte with tuneable work function for effective hole transport in polymer solar cells. *J. Mater. Chem. A* **2016**, *4*, 15670–15675. [[CrossRef](#)]
266. Gribkova, O.L.; Iakobson, O.D.; Nekrasov, A.A.; Cabanova, V.A.; Tverskoy, V.A.; Tameev, A.R.; Vannikov, A.V. Ultraviolet-Visible-Near Infrared and Raman spectroelectrochemistry of poly(3,4-ethylenedioxythiophene) complexes with sulfonated polyelectrolytes. The role of inter- and intra-molecular interactions in polyelectrolyte. *Electrochim. Acta* **2016**, *222*, 409–420. [[CrossRef](#)]
267. Kim, D.H.; Lee, D.J.; Kim, B.; Yun, C.; Kang, M.H. Tailoring PEDOT:PSS polymer electrode for solution-processed inverted organic solar cells. *Solid-State Electron.* **2020**, *169*, 107808. [[CrossRef](#)]
268. Liu, L.; Li, F.; Zhao, C.; Bi, F.; Jiu, T.; Zhao, M.; Li, J.; Zhang, G.; Wang, L.; Fang, J.; et al. Performance Enhancement of Conventional Polymer Solar Cells with TTF-py-Modified PEDOT:PSS Film as the Hole Transport Layer. *ACS Appl. Energy Mater.* **2019**, *2*, 6577–6583. [[CrossRef](#)]
269. Wang, J.; Zheng, Z.; Zhang, D.; Zhang, J.; Zhou, J.; Liu, J.; Xie, S.; Zhao, Y.; Zhang, Y.; Wei, Z.; et al. Regulating Bulk-Heterojunction Molecular Orientations through Surface Free Energy Control of Hole-Transporting Layers for High-Performance Organic Solar Cells. *Adv. Mater.* **2019**, *31*, 1806921. [[CrossRef](#)]
270. Tang, H.; Liu, Z.; Hu, Z.; Liang, Y.; Huang, F.; Cao, Y. Oxoammonium enabled secondary doping of hole transporting material PEDOT:PSS for high-performance organic solar cells. *Sci. China Chem.* **2020**, *63*, 802–809. [[CrossRef](#)]
271. Khan, M.A.; Farva, U. Elucidation of hierarchical metallophthalocyanine buffer layers in bulk heterojunction solar cells. *RSC Adv.* **2017**, *7*, 11304–11311. [[CrossRef](#)]
272. Wang, J.; Yu, H.; Hou, C.; Zhang, J. Solution-Processable PEDOT:PSS:α-In₂Se₃ with Enhanced Conductivity as a Hole Transport Layer for High-Performance Polymer Solar Cells. *ACS Appl. Mater. Interfaces* **2020**, *12*, 26543–26554. [[CrossRef](#)]
273. Zeng, M.; Wang, X.; Ma, R.; Zhu, W.; Li, Y.; Chen, Z.; Zhou, J.; Li, W.; Liu, T.; He, Z.; et al. Dopamine Semiquinone Radical Doped PEDOT:PSS: Enhanced Conductivity, Work Function and Performance in Organic Solar Cells. *Adv. Energy Mater.* **2020**, *10*, 2000743. [[CrossRef](#)]
274. Roh, S.H.; Kim, J.K. Hexagonal Array Patterned PMMA Buffer Layer for Efficient Hole Transport and Tailored Interfacial Properties of FTO-Based Organic Solar Cells. *Macromol. Res.* **2018**, *26*, 1173–1178. [[CrossRef](#)]
275. Kwak, C.K.; Pérez, G.E.; Freestone, B.G.; Al-Isaee, S.A.; Iraqi, A.; Lidzey, D.G.; Dunbar, A.D.F. Improved efficiency in organic solar cells via conjugated polyelectrolyte additive in the hole transporting layer. *J. Mater. Chem. C* **2016**, *4*, 10722–10730. [[CrossRef](#)]
276. Palma-Cando, A.; Scherf, U. Electrochemically Generated Thin Films of Microporous Polymer Networks: Synthesis, Properties, and Applications. *Macromol. Chem. Phys.* **2016**, *217*, 827–841. [[CrossRef](#)]
277. Palma-Cando, A.; Scherf, U. Electrogenerated Thin Films of Microporous Polymer Networks with Remarkably Increased Electrochemical Response to Nitroaromatic Analytes. *ACS Appl. Mater. Interfaces* **2015**, *7*, 11127–11133. [[CrossRef](#)] [[PubMed](#)]
278. Räupe, A.; Palma-Cando, A.; Shkura, E.; Teckhausen, P.; Polywka, A.; Görrn, P.; Scherf, U.; Riedl, T. Highly sensitive gas-phase explosive detection by luminescent microporous polymer networks. *Sci. Rep.* **2016**, *6*, 29118. [[CrossRef](#)]

279. Palma-Cando, A.; Woitassek, D.; Brunklaus, G.; Scherf, U. Luminescent tetraphenylethene-cored, carbazole- and thiophene-based microporous polymer films for the chemosensing of nitroaromatic analytes. *Mater. Chem. Front.* **2017**, *1*, 1118–1124. [[CrossRef](#)]
280. Palma-Cando, A.; Preis, E.; Scherf, U. Silicon-or Carbon-Cored Multifunctional Carbazolyl Monomers for the Electrochemical Generation of Microporous Polymer Films. *Macromolecules* **2016**, *49*, 8041–8047. [[CrossRef](#)]
281. Palma-Cando, A.; Rendón-Enríquez, I.; Tausch, M.; Scherf, U. Thin Functional Polymer Films by Electropolymerization. *Nanomaterials* **2019**, *9*, 1125. [[CrossRef](#)]
282. Palma-Cando, A.; Brunklaus, G.; Scherf, U. Thiophene-Based Microporous Polymer Networks via Chemical or Electrochemical Oxidative Coupling. *Macromolecules* **2015**, *48*, 6816–6824. [[CrossRef](#)]
283. Gu, C.; Huang, N.; Chen, Y.; Qin, L.; Xu, H.; Zhang, S.; Li, F.; Ma, Y.; Jiang, D. π -Conjugated Microporous Polymer Films: Designed Synthesis, Conducting Properties, and Photoenergy Conversions. *Angew. Chem.* **2015**, *127*, 13798–13802. [[CrossRef](#)]
284. Liu, C.; Luo, H.; Shi, G.; Nian, L.; Chi, Z.; Ma, Y. Electrochemical route to fabricate porous organic polymers film and its application for polymer solar cells. *Dyes Pigments* **2017**, *142*, 132–138. [[CrossRef](#)]
285. Li, Y.; Sun, X.; Zhang, X.; Zhang, D.; Xia, H.; Zhou, J.; Ahmad, N.; Leng, X.; Yang, S.; Zhang, Y.; et al. Built-in voltage enhanced by in situ electrochemical polymerized undoped conjugated hole-transporting modifiers in organic solar cells. *J. Mater. Chem. C* **2020**, *8*, 2676–2681. [[CrossRef](#)]
286. Lee, E.J.; Han, J.P.; Jung, S.E.; Choi, M.H.; Moon, D.K. Improvement in Half-Life of Organic Solar Cells by Using a Blended Hole Extraction Layer Consisting of PEDOT:PSS and Conjugated Polymer Electrolyte. *ACS Appl. Mater. Interfaces* **2016**, *8*, 31791–31798. [[CrossRef](#)] [[PubMed](#)]
287. Pérez, G.E.; Erothu, H.; Topham, P.D.; Bastianini, F.; Alanazi, T.I.; Bernardo, G.; Parnell, A.J.; King, S.M.; Dunbar, A.D.F. Improved Performance and Stability of Organic Solar Cells by the Incorporation of a Block Copolymer Interfacial Layer. *Adv. Mater. Interfaces* **2020**, *7*, 2000918. [[CrossRef](#)]
288. Hamed, M.S.G.; Oseni, S.O.; Kumar, A.; Sharma, G.; Mola, G.T. Nickel sulphide nano-composite assisted hole transport in thin film polymer solar cells. *Sol. Energy* **2020**, *195*, 310–317. [[CrossRef](#)]
289. Wei, Y.; Zhang, Q.; Wan, H.; Zhang, Y.; Zheng, S.; Zhang, Y. A facile synthesis of segmented silver nanowires and enhancement of the performance of polymer solar cells. *Phys. Chem. Chem. Phys.* **2018**, *20*, 18837–18843. [[CrossRef](#)]
290. Hao, J.; Xu, Y.; Chen, S.; Zhang, Y.; Mai, J.; Lau, T.-K.; Zhang, R.; Mei, Y.; Wang, L.; Lu, X.; et al. Broadband plasmon-enhanced polymer solar cells with power conversion efficiency of 9.26% using mixed Au nanoparticles. *Opt. Commun.* **2016**, *362*, 50–58. [[CrossRef](#)]
291. Oh, Y.; Lim, J.W.; Kim, J.G.; Wang, H.; Kang, B.-H.; Park, Y.W.; Kim, H.; Jang, Y.J.; Kim, J.; Kim, D.H.; et al. Plasmonic Periodic Nanodot Arrays via Laser Interference Lithography for Organic Photovoltaic Cells with >10% Efficiency. *ACS Nano* **2016**, *10*, 10143–10151. [[CrossRef](#)]
292. Singh, A.; Dey, A.; Das, D.; Iyer, P.K. Combined influence of plasmonic metal nanoparticles and dual cathode buffer layers for highly efficient rrP3HT:PCBM-based bulk heterojunction solar cells. *J. Mater. Chem. C* **2017**, *5*, 6578–6587. [[CrossRef](#)]
293. Sah, P.-T.; Chang, W.-C.; Chen, J.-H.; Wang, H.-H.; Chan, L.-H. Bimetallic Ag-Au-Ag nanorods used to enhance efficiency of polymer solar cells. *Electrochim. Acta* **2018**, *259*, 293–302. [[CrossRef](#)]
294. Tang, M.; Sun, B.; Zhou, D.; Gu, Z.; Chen, K.; Guo, J.; Feng, L.; Zhou, Y. Broad-band plasmonic Cu-Au bimetallic nanoparticles for organic bulk heterojunction solar cells. *Org. Electron.* **2016**, *38*, 213–221. [[CrossRef](#)]
295. Adedeji, M.A.; Hamed, M.S.G.; Mola, G.T. Light trapping using copper decorated nano-composite in the hole transport layer of organic solar cell. *Sol. Energy* **2020**, *203*, 83–90. [[CrossRef](#)]
296. Najeeb, M.A.; Abdullah, S.M.; Aziz, F.; Ahmad, Z.; Shakoor, R.A.; Mohamed, A.M.A.; Khalil, U.; Swelm, W.; Al-Ghamdi, A.A.; Sulaiman, K. A comparative Study on the performance of hybrid solar cells containing ZnS/Te QDs in hole transporting layer and photoactive layer. *J. Nanopart. Res.* **2016**, *18*, 384. [[CrossRef](#)]
297. Zhang, X.; Jiang, Q.; Wang, J.; Tang, J. Black phosphorous quantum dots as an effective interlayer modifier in polymer solar cells. *Sol. Energy* **2020**, *206*, 670–676. [[CrossRef](#)]
298. Ismail, Y.A.M.; Kishi, N.; Soga, T. Improvement of organic solar cells using aluminium microstructures prepared in PEDOT:PSS buffer layer by using ultrasonic ablation technique. *Thin Solid Films* **2016**, *616*, 73–79. [[CrossRef](#)]
299. Kesavan, A.V.; Jagdish, A.K.; Ramamurthy, P.C. Organic Inorganic Hybrid Hole Transport Layer for Light Management in Inverted Organic Photovoltaic. *IEEE J. Photovolt.* **2017**, *7*, 787–791. [[CrossRef](#)]
300. Liu, Z.; Park, J.; Li, B.; Chan, H.P.; Yi, D.K.; Lee, E.-C. Performance improvement of organic bulk-heterojunction solar cells using complementary plasmonic gold nanorods. *Org. Electron.* **2020**, *84*, 105802. [[CrossRef](#)]
301. Phetsang, S.; Nootchanat, S.; Lertvachirapaiboon, C.; Ishikawa, R.; Shinbo, K.; Kato, K.; Mungkornasawakul, P.; Ounnunkad, K.; Baba, A. Enhancement of organic solar cell performance by incorporating gold quantum dots (AuQDs) on a plasmonic grating. *Nanoscale Adv.* **2020**, *2*, 2950–2957. [[CrossRef](#)]
302. Haase, M.; Schäfer, H. Upconverting Nanoparticles. *Angew. Chemie Int. Ed.* **2011**, *50*, 5808–5829. [[CrossRef](#)]
303. Mei, Y.; Ma, X.; Fan, Y.; Bai, Z.; Cheng, F.; Hu, Y.; Fan, Q.; Chen, S.; Huang, W. Application of β -NaYF₄:Er³⁺ (2%), Yb³⁺ (18%) Up-Conversion Nanoparticles in Polymer Solar Cells and its Working Mechanism. *J. Nanosci. Nanotechnol.* **2016**, *16*, 7380–7387. [[CrossRef](#)]
304. Mola, G.T.; Arbab, E.A.A. Bimetallic nanocomposite as hole transport co-buffer layer in organic solar cell. *Appl. Phys. A* **2017**, *123*, 772. [[CrossRef](#)]

305. Michalska, M.; Iwan, A.; Andrzejczuk, M.; Roguska, A.; Sikora, A.; Boharewicz, B.; Tazbir, I.; Hreniak, A.; Popłoński, S.; Korona, K.P. Analysis of the surface decoration of TiO₂ grains using silver nanoparticles obtained by ultrasonochemical synthesis towards organic photovoltaics. *New J. Chem.* **2018**, *42*, 7340–7354. [[CrossRef](#)]
306. Truong, N.T.N.; Kim, C.D.; Minnam Reddy, V.R.; Thai, V.H.; Jeon, H.J.; Park, C. Shape control of plasmonic gold nanoparticles and its application to vacuum-free bulk hetero-junction solar cells. *J. Mater. Sci. Mater. Electron.* **2020**, *31*, 22957–22965. [[CrossRef](#)]
307. Mohammad, T.; Dwivedi, C.; Kumar, V.; Dutta, V. Role of Continuous Spray Pyrolyzed synthesized MoO₃ nanorods in PEDOT:PSS matrix by electric field assisted spray deposition for organic photovoltaics. *Org. Electron.* **2020**, *77*, 105525. [[CrossRef](#)]
308. Pan, J.; Li, P.; Cai, L.; Hu, Y.; Zhang, Y. All-solution processed double-decked PEDOT:PSS/V₂O₅ nanowires as buffer layer of high performance polymer photovoltaic cells. *Sol. Energy Mater. Sol. Cells* **2016**, *144*, 616–622. [[CrossRef](#)]
309. Li, J.; Qin, J.; Liu, X.; Ren, M.; Tong, J.; Zheng, N.; Chen, W.; Xia, Y. Enhanced organic photovoltaic performance through promoting crystallinity of photoactive layer and conductivity of hole-transporting layer by V₂O₅ doped PEDOT:PSS hole-transporting layers. *Sol. Energy* **2020**, *211*, 1102–1109. [[CrossRef](#)]
310. Du, X.; Lytken, O.; Killian, M.S.; Cao, J.; Stubhan, T.; Turbiez, M.; Schmuki, P.; Steinrück, H.-P.; Ding, L.; Fink, R.H.; et al. Overcoming Interfacial Losses in Solution-Processed Organic Multi-Junction Solar Cells. *Adv. Energy Mater.* **2017**, *7*, 1601959. [[CrossRef](#)]
311. Wang, Y.; Han, J.; Cai, L.; Li, N.; Li, Z.; Zhu, F. Efficient and stable operation of nonfullerene organic solar cells: Retaining a high built-in potential. *J. Mater. Chem. A* **2020**, *8*, 21255–21264. [[CrossRef](#)]
312. Mbuyise, X.G.; Arbab, E.A.A.; Kaviyarasu, K.; Pellicane, G.; Maaza, M.; Mola, G.T. Zinc oxide doped single wall carbon nanotubes in hole transport buffer layer. *J. Alloys Compd.* **2017**, *706*, 344–350. [[CrossRef](#)]
313. Zheng, Z.; Hu, Q.; Zhang, S.; Zhang, D.; Wang, J.; Xie, S.; Wang, R.; Qin, Y.; Li, W.; Hong, L.; et al. A Highly Efficient Non-Fullerene Organic Solar Cell with a Fill Factor over 0.80 Enabled by a Fine-Tuned Hole-Transporting Layer. *Adv. Mater.* **2018**, *30*, 1801801. [[CrossRef](#)] [[PubMed](#)]
314. Han, Y.W.; Jeon, S.J.; Lee, H.S.; Park, H.; Kim, K.S.; Lee, H.; Moon, D.K. Evaporation-Free Nonfullerene Flexible Organic Solar Cell Modules Manufactured by An All-Solution Process. *Adv. Energy Mater.* **2019**, *9*, 1902065. [[CrossRef](#)]
315. Sun, L.; Zeng, W.; Xie, C.; Hu, L.; Dong, X.; Qin, F.; Wang, W.; Liu, T.; Jiang, X.; Jiang, Y.; et al. Flexible All-Solution-Processed Organic Solar Cells with High-Performance Nonfullerene Active Layers. *Adv. Mater.* **2020**, *32*, 1907840. [[CrossRef](#)] [[PubMed](#)]
316. Ji, G.; Wang, Y.; Luo, Q.; Han, K.; Xie, M.; Zhang, L.; Wu, N.; Lin, J.; Xiao, S.; Li, Y.-Q.; et al. Fully Coated Semitransparent Organic Solar Cells with a Doctor-Blade-Coated Composite Anode Buffer Layer of Phosphomolybdic Acid and PEDOT:PSS and a Spray-Coated Silver Nanowire Top Electrode. *ACS Appl. Mater. Interfaces* **2018**, *10*, 943–954. [[CrossRef](#)]
317. Liu, Z.; Niu, S.; Wang, N. Oleylamine-functionalized graphene oxide as an electron block layer towards high-performance and photostable fullerene-free polymer solar cells. *Nanoscale* **2017**, *9*, 16293–16304. [[CrossRef](#)]
318. Maity, S.; Thomas, T. Hole-Collecting Treated Graphene Layer and PTB7:PC 71 BM-Based Bulk-Heterojunction OPV With Improved Carrier Collection and Photovoltaic Efficiency. *IEEE Trans. Electron Devices* **2018**, *65*, 4548–4554. [[CrossRef](#)]
319. Hilal, M.; Han, J.I. Enhancing the photovoltaic characteristics of organic solar cells by introducing highly conductive graphene as a conductive platform for a PEDOT:PSS anode interfacial layer. *J. Mater. Sci. Mater. Electron.* **2019**, *30*, 6187–6200. [[CrossRef](#)]
320. Amollo, T.A.; Mola, G.T.; Nyamori, V.O. High-performance organic solar cells utilizing graphene oxide in the active and hole transport layers. *Sol. Energy* **2018**, *171*, 83–91. [[CrossRef](#)]
321. Goumri, M.; Lucas, B.; Ratier, B.; Baitoul, M. Inverted Polymer Solar Cells with a Reduced Graphene Oxide/Poly (3,4-Ethylene Dioxathiophene):Poly(4-Styrene Sulfonate) (PEDOT:PSS) Hole Transport Layer. *J. Electron. Mater.* **2019**, *48*, 1097–1105. [[CrossRef](#)]
322. Ozcan, S.; Erer, M.C.; Vempati, S.; Uyar, T.; Toppare, L.; Çirpan, A. Graphene oxide-doped PEDOT:PSS as hole transport layer in inverted bulk heterojunction solar cell. *J. Mater. Sci. Mater. Electron.* **2020**, *31*, 3576–3584. [[CrossRef](#)]
323. Amollo, T.A.; Mola, G.T.; Nyamori, V.O. Polymer solar cells with reduced graphene oxide–germanium quantum dots nanocomposite in the hole transport layer. *J. Mater. Sci. Mater. Electron.* **2018**, *29*, 7820–7831. [[CrossRef](#)]
324. Raj, P.G.; Rani, V.S.; Kanwat, A.; Jang, J. Enhanced organic photovoltaic properties via structural modifications in PEDOT:PSS due to graphene oxide doping. *Mater. Res. Bull.* **2016**, *74*, 346–352. [[CrossRef](#)]
325. Srivastava, S.K.; Pionteck, J. Recent Advances in Preparation, Structure, Properties and Applications of Graphite Oxide. *J. Nanosci. Nanotechnol.* **2015**, *15*, 1984–2000. [[CrossRef](#)] [[PubMed](#)]
326. Toh, S.Y.; Loh, K.S.; Kamarudin, S.K.; Daud, W.R.W. Graphene production via electrochemical reduction of graphene oxide: Synthesis and characterisation. *Chem. Eng. J.* **2014**, *251*, 422–434. [[CrossRef](#)]
327. Iwan, A.; Caballero-Briones, F.; Filapek, M.; Boharewicz, B.; Tazbir, I.; Hreniak, A.; Guerrero-Contreras, J. Electrochemical and photocurrent characterization of polymer solar cells with improved performance after GO addition to the PEDOT:PSS hole transporting layer. *Sol. Energy* **2017**, *146*, 230–242. [[CrossRef](#)]
328. Rafique, S.; Abdullah, S.M.; Shahid, M.M.; Ansari, M.O.; Sulaiman, K. Significantly improved photovoltaic performance in polymer bulk heterojunction solar cells with graphene oxide /PEDOT:PSS double decked hole transport layer. *Sci. Rep.* **2017**, *7*, 39555. [[CrossRef](#)]
329. Hilal, M.; Han, J.I. Significant improvement in the photovoltaic stability of bulk heterojunction organic solar cells by the molecular level interaction of graphene oxide with a PEDOT: PSS composite hole transport layer. *Sol. Energy* **2018**, *167*, 24–34. [[CrossRef](#)]
330. Moon, B.J.; Jang, D.; Yi, Y.; Lee, H.; Kim, S.J.; Oh, Y.; Lee, S.H.; Park, M.; Lee, S.; Bae, S. Multi-functional nitrogen self-doped graphene quantum dots for boosting the photovoltaic performance of BHJ solar cells. *Nano Energy* **2017**, *34*, 36–46. [[CrossRef](#)]

331. Rafique, S.; Roslan, N.A.; Abdullah, S.M.; Li, L.; Supangat, A.; Jilani, A.; Iwamoto, M. UV-ozone treated graphene oxide/PEDOT:PSS bilayer as a novel hole transport layer in highly efficient and stable organic solar cells. *Org. Electron.* **2019**, *66*, 32–42. [[CrossRef](#)]
332. Xing, W.; Chen, Y.; Wu, X.; Xu, X.; Ye, P.; Zhu, T.; Guo, Q.; Yang, L.; Li, W.; Huang, H. PEDOT:PSS-Assisted Exfoliation and Functionalization of 2D Nanosheets for High-Performance Organic Solar Cells. *Adv. Funct. Mater.* **2017**, *27*, 1701622. [[CrossRef](#)]
333. Koo, D.; Jung, S.; Oh, N.K.; Choi, Y.; Seo, J.; Lee, J.; Kim, U.; Park, H. Improved charge transport via WSe₂-mediated hole transporting layer toward efficient organic solar cells. *Semicond. Sci. Technol.* **2018**, *33*, 125020. [[CrossRef](#)]
334. Ramasamy, M.S.; Ryu, K.Y.; Lim, J.W.; Bibi, A.; Kwon, H.; Lee, J.-E.; Kim, D.H.; Kim, K. Solution-Processed PEDOT:PSS/MoS₂ Nanocomposites as Efficient Hole-Transporting Layers for Organic Solar Cells. *Nanomaterials* **2019**, *9*, 1328. [[CrossRef](#)] [[PubMed](#)]
335. Dang, Y.; Shen, S.; Wang, Y.; Qu, X.; Huang, S.; Dong, Q.; Silva, S.R.P.; Kang, B. Hole Extraction Enhancement for Efficient Polymer Solar Cells with Boronic Acid Functionalized Carbon Nanotubes doped Hole Transport Layers. *ACS Sustain. Chem. Eng.* **2018**, *6*, 5122–5131. [[CrossRef](#)]
336. Yang, Q.; Yu, S.; Fu, P.; Yu, W.; Liu, Y.; Liu, X.; Feng, Z.; Guo, X.; Li, C. Boosting Performance of Non-Fullerene Organic Solar Cells by 2D g-C₃N₄ Doped PEDOT:PSS. *Adv. Funct. Mater.* **2020**, *30*, 1910205. [[CrossRef](#)]
337. Hou, C.; Yu, H. Modifying the nanostructures of PEDOT:PSS/Ti₃C₂TX composite hole transport layers for highly efficient polymer solar cells. *J. Mater. Chem. C* **2020**, *8*, 4169–4180. [[CrossRef](#)]
338. Chiou, G.-C.; Lin, M.-W.; Lai, Y.-L.; Chang, C.-K.; Jiang, J.-M.; Su, Y.-W.; Wei, K.-H.; Hsu, Y.-J. Fluorene Conjugated Polymer/Nickel Oxide Nanocomposite Hole Transport Layer Enhances the Efficiency of Organic Photovoltaic Devices. *ACS Appl. Mater. Interfaces* **2017**, *9*, 2232–2239. [[CrossRef](#)] [[PubMed](#)]
339. Guo, Y.; Lei, H.; Xiong, L.; Li, B.; Fang, G. Organic solar cells based on a Cu₂O/FBT-TH4 anode buffer layer with enhanced power conversion efficiency and ambient stability. *J. Mater. Chem. C* **2017**, *5*, 8033–8040. [[CrossRef](#)]
340. Jo, W.J.; Nelson, J.T.; Chang, S.; Bulović, V.; Gradečak, S.; Strano, M.S.; Gleason, K.K. Oxidative Chemical Vapor Deposition of Neutral Hole Transporting Polymer for Enhanced Solar Cell Efficiency and Lifetime. *Adv. Mater.* **2016**, *28*, 6399–6404. [[CrossRef](#)]
341. Awada, H.; Mattana, G.; Tournebize, A.; Rodriguez, L.; Flahaut, D.; Vellutini, L.; Lartigau-Dagron, C.; Billon, L.; Bousquet, A.; Chambon, S. Surface engineering of ITO electrode with a functional polymer for PEDOT:PSS-free organic solar cells. *Org. Electron.* **2018**, *57*, 186–193. [[CrossRef](#)]
342. Kadem, B.Y.; Kadhim, R.G.; Banimuslem, H. Efficient P₃HT:SWCNTs hybrids as hole transport layer in P₃HT:PCBM organic solar cells. *J. Mater. Sci. Mater. Electron.* **2018**, *29*, 9418–9426. [[CrossRef](#)]
343. Babaei, Z.; Rezaei, B.; Pisheh, M.K.; Afshar-Taromi, F. In situ synthesis of gold/silver nanoparticles and polyaniline as buffer layer in polymer solar cells. *Mater. Chem. Phys.* **2020**, *248*, 122879. [[CrossRef](#)]
344. Deng, L.; Li, D.; Agbolaghi, S. Networked Conductive Polythiophene/Polyaniline Bottlebrushes with Modified Carbon Nanotubes As Hole Transport Layer in Organic Photovoltaics. *J. Electron. Mater.* **2020**, *49*, 937–948. [[CrossRef](#)]
345. Sorkhishams, N.; Massoumi, B.; Saraei, M.; Agbolaghi, S. Electrode buffer layers via networks of polythiophene/polyaniline bottlebrushes and carbon nanotubes in organic solar cells. *J. Mater. Sci. Mater. Electron.* **2019**, *30*, 21117–21125. [[CrossRef](#)]
346. Biswas, S.; You, Y.-J.; Kim, J.; Ha, S.R.; Choi, H.; Kwon, S.-H.; Kim, K.-K.; Shim, J.W.; Kim, H. Decent efficiency improvement of organic photovoltaic cell with low acidic hole transport material by controlling doping concentration. *Appl. Surf. Sci.* **2020**, *512*, 145700. [[CrossRef](#)]
347. Biswas, S.; You, Y.-J.; Lee, Y.; Shim, J.W.; Kim, H. Efficiency improvement of indoor organic solar cell by optimization of the doping level of the hole extraction layer. *Dyes Pigments* **2020**, *183*, 108719. [[CrossRef](#)]
348. Biswas, S.; You, Y.-J.; Shim, J.W.; Kim, H. Utilization of poly (4-styrenesulfonic acid) doped polyaniline as a hole transport layer of organic solar cell for indoor applications. *Thin Solid Films* **2020**, *700*, 137921. [[CrossRef](#)]
349. Abdulrazzaq, O.A.; Bourdo, S.E.; Saini, V.; Biris, A.S. Acid-free polyaniline:graphene-oxide hole transport layer in organic solar cells. *J. Mater. Sci. Mater. Electron.* **2020**, *31*, 21640–21650. [[CrossRef](#)]
350. Dong, J.; Guo, J.; Wang, X.; Dong, P.; Wang, Z.; Zhou, Y.; Miao, Y.; Zhao, B.; Hao, Y.; Wang, H.; et al. A Low-Temperature Solution-Processed CuSCN/Polymer Hole Transporting Layer Enables High Efficiency for Organic Solar Cells. *ACS Appl. Mater. Interfaces* **2020**, *12*, 46373–46380. [[CrossRef](#)]
351. Houston, J.E.; Kraft, M.; Scherf, U.; Evans, R.C. Sequential detection of multiple phase transitions in model biological membranes using a red-emitting conjugated polyelectrolyte. *Phys. Chem. Chem. Phys.* **2016**, *18*, 12423–12427. [[CrossRef](#)]
352. Meazzini, I.; Blayo, C.; Arlt, J.; Marques, A.-T.; Scherf, U.; Burrows, H.D.; Evans, R.C. Ureasil organic–inorganic hybrids as photoactive waveguides for conjugated polyelectrolyte luminescent solar concentrators. *Mater. Chem. Front.* **2017**, *1*, 2271–2282. [[CrossRef](#)]
353. Willis-Fox, N.; Gutacker, A.; Browne, M.P.; Khan, A.R.; Lyons, M.E.G.; Scherf, U.; Evans, R.C. Selective recognition of biologically important anions using a diblock polyfluorene–polythiophene conjugated polyelectrolyte. *Polym. Chem.* **2017**, *8*, 7151–7159. [[CrossRef](#)]
354. Balcı Leinen, M.; Berger, F.J.; Klein, P.; Mühlhous, M.; Zorn, N.F.; Settele, S.; Allard, S.; Scherf, U.; Zaumseil, J. Doping-Dependent Energy Transfer from Conjugated Polyelectrolytes to (6,5) Single-Walled Carbon Nanotubes. *J. Phys. Chem. C* **2019**, *123*, 22680–22689. [[CrossRef](#)]

355. Pipertzis, A.; Papamokos, G.; Sachnik, O.; Allard, S.; Scherf, U.; Floudas, G. Ionic Conductivity in Polyfluorene-Based Diblock Copolymers Comprising Nanodomains of a Polymerized Ionic Liquid and a Solid Polymer Electrolyte Doped with LiTFSI. *Macromolecules* **2021**, *54*, 4257–4268. [[CrossRef](#)]
356. Martelo, L.; Fonseca, S.; Marques, A.; Burrows, H.; Valente, A.; Justino, L.; Scherf, U.; Pradhan, S.; Song, Q. Effects of Charge Density on Photophysics and Aggregation Behavior of Anionic Fluorene-Arylene Conjugated Polyelectrolytes. *Polymers* **2018**, *10*, 258. [[CrossRef](#)]
357. Jo, J.W.; Jung, J.W.; Bae, S.; Ko, M.J.; Kim, H.; Jo, W.H.; Jen, A.K.-Y.; Son, H.J. Development of Self-Doped Conjugated Polyelectrolytes with Controlled Work Functions and Application to Hole Transport Layer Materials for High-Performance Organic Solar Cells. *Adv. Mater. Interfaces* **2016**, *3*, 1500703. [[CrossRef](#)]
358. Jo, J.W.; Yun, J.H.; Bae, S.; Ko, M.J.; Son, H.J. Development of a conjugated donor-acceptor polyelectrolyte with high work function and conductivity for organic solar cells. *Org. Electron.* **2017**, *50*, 1–6. [[CrossRef](#)]
359. Cui, Y.; Xu, B.; Yang, B.; Yao, H.; Li, S.; Hou, J. A Novel pH Neutral Self-Doped Polymer for Anode Interfacial Layer in Efficient Polymer Solar Cells. *Macromolecules* **2016**, *49*, 8126–8133. [[CrossRef](#)]
360. Choi, M.-H.; Lee, E.J.; Han, J.P.; Moon, D.K. Solution-processed pH-neutral conjugated polyelectrolytes with one-atom variation (O, S, Se) as a novel hole-collecting layer in organic photovoltaics. *Sol. Energy Mater. Sol. Cells* **2016**, *155*, 243–252. [[CrossRef](#)]
361. Xu, H.; Fu, X.; Cheng, X.; Huang, L.; Zhou, D.; Chen, L.; Chen, Y. Highly and homogeneously conductive conjugated polyelectrolyte hole transport layers for efficient organic solar cells. *J. Mater. Chem. A* **2017**, *5*, 14689–14696. [[CrossRef](#)]
362. Moon, S.; Khadtare, S.; Wong, M.; Han, S.-H.; Bazan, G.C.; Choi, H. Hole transport layer based on conjugated polyelectrolytes for polymer solar cells. *J. Colloid Interface Sci.* **2018**, *518*, 21–26. [[CrossRef](#)]
363. Xie, Q.; Zhang, J.; Xu, H.; Liao, X.; Chen, Y.; Li, Y.; Chen, L. Self-doped polymer with fluorinated phenylene as hole transport layer for efficient polymer solar cells. *Org. Electron.* **2018**, *61*, 207–214. [[CrossRef](#)]
364. Lee, E.J.; Choi, M.H.; Han, Y.W.; Moon, D.K. Effect on Electrode Work Function by Changing Molecular Geometry of Conjugated Polymer Electrolytes and Application for Hole-Transporting Layer of Organic Optoelectronic Devices. *ACS Appl. Mater. Interfaces* **2017**, *9*, 44060–44069. [[CrossRef](#)] [[PubMed](#)]
365. Xu, H.; Zou, H.; Zhou, D.; Zeng, G.; Chen, L.; Liao, X.; Chen, Y. Printable Hole Transport Layer for 1.0 cm² Organic Solar Cells. *ACS Appl. Mater. Interfaces* **2020**, *12*, 52028–52037. [[CrossRef](#)] [[PubMed](#)]
366. Xu, X.-P.; Li, S.-Y.; Li, Y.; Peng, Q. Recent progress in organic hole-transporting materials with 4-anisylamino-based end caps for efficient perovskite solar cells. *Rare Met.* **2021**, *40*, 1669–1690. [[CrossRef](#)]
367. Rombach, F.M.; Haque, S.A.; Macdonald, T.J. Lessons learned from spiro-OMeTAD and PTAA in perovskite solar cells. *Energy Environ. Sci.* **2021**, *14*, 5161–5190. [[CrossRef](#)]
368. Li, H.; Fu, K.; Boix, P.P.; Wong, L.H.; Hagfeldt, A.; Grätzel, M.; Mhaisalkar, S.G.; Grimsdale, A.C. Hole-Transporting Small Molecules Based on Thiophene Cores for High Efficiency Perovskite Solar Cells. *ChemSusChem* **2014**, *7*, 3420–3425. [[CrossRef](#)]
369. Bormann, L.; Selzer, F.; Weiß, N.; Kneppel, D.; Leo, K.; Müller-Meskamp, L. Doped hole transport layers processed from solution: Planarization and bridging the voids in noncontinuous silver nanowire electrodes. *Org. Electron.* **2016**, *28*, 163–171. [[CrossRef](#)]
370. Cheng, J.; Ren, X.; Zhu, H.L.; Mao, J.; Liang, C.; Zhuang, J.; Roy, V.A.L.; Choy, W.C.H. Pre- and post-treatments free nanocomposite based hole transport layer for high performance organic solar cells with considerably enhanced reproducibility. *Nano Energy* **2017**, *34*, 76–85. [[CrossRef](#)]
371. Courté, M.; Alaeddine, M.; Barth, V.; Tortech, L.; Fichou, D. Structural and electronic properties of 2,2',6,6'-tetraphenyl-dipyrylylidene and its use as a hole-collecting interfacial layer in organic solar cells. *Dye. Pigment.* **2017**, *141*, 487–492. [[CrossRef](#)]
372. Wang, L.; Li, X.; Tan, T.W.; Shi, Y.; Zhao, X.Y.; Mi, B.X.; Gao, Z.Q. An organic semiconductor as an anode-buffer for the improvement of small molecular photovoltaic cells. *RSC Adv.* **2017**, *7*, 38204–38209. [[CrossRef](#)]
373. Li, J.; Zheng, Y.; Zheng, D.; Yu, J. Effect of organic small-molecule hole injection materials on the performance of inverted organic solar cells. *J. Photonics Energy* **2016**, *6*, 035502. [[CrossRef](#)]
374. Li, P.; Wu, B.; Yang, Y.C.; Huang, H.S.; De Yang, X.; Zhou, G.D.; Song, Q.L. Improved charge transport ability of polymer solar cells by using NPB/MoO₃ as anode buffer layer. *Sol. Energy* **2018**, *170*, 212–216. [[CrossRef](#)]
375. Shi, Z.; Deng, H.; Zhao, W.; Cao, H.; Yang, Q.; Zhang, J.; Ban, D.; Qin, D. An alternative hole extraction layer for inverted organic solar cells. *Appl. Phys. A* **2018**, *124*, 676. [[CrossRef](#)]
376. Wang, S.; Yang, P.; Chang, K.; Lv, W.; Mi, B.; Song, J.; Zhao, X.; Gao, Z. A new dibenzo[g,p]chrysene derivative as an efficient anode buffer for inverted polymer solar cells. *Org. Electron.* **2019**, *74*, 269–275. [[CrossRef](#)]
377. Liu, L.; Zhou, S.; Zhao, C.; Jiu, T.; Bi, F.; Jian, H.; Zhao, M.; Zhang, G.; Wang, L.; Li, F.; et al. TTA as a potential hole transport layer for application in conventional polymer solar cells. *J. Energy Chem.* **2020**, *42*, 210–216. [[CrossRef](#)]